Tunable Filters and RF MEMS Variable Capacitors with Closed Loop Control

by

Nino Zahirovic

A thesis
presented to the University of Waterloo
in fulfillment of the
thesis requirement for the degree of
Doctor of Philosophy
in
Electrical and Computer Engineering

Waterloo, Ontario, Canada, 2011

I hereby declare that I am the sole author of this thesis. This is a true copy of the thesis, including any required final revisions, as accepted by my examiners.

I understand that my thesis may be made electronically available to the public.

Nino Zahirovic

Abstract

Multi-band and multi-mode radios are becoming prevalent and necessary in order to provide optimal data rates across a network with a diverse and spotty landscape of coverage areas (3G, HSPA, LTE, etc.). As the number of required bands and modes increases, the aggregate cost of discrete RF signal chains justifies the adoption of tunable solutions. Tunable filters are one of the pieces crucial to signal chain amalgamation.

The main requirements for a tunable filter are high unloaded quality factor, wide tuning range, high tuning speed, high linearity, and small size. MEMS technology is the most promising in terms of tuning range, quality factor, linearity and size. In addition, a filter that maintains a constant passband bandwidth as the center frequency is tuned is preferred since the analog baseband processing circuitry tends to be tailored for a particular signal bandwidth.

In this work, a novel design technique for tunable filters with controlled and predictable bandwidth variation is presented. The design technique is presented alongside an analysis and modeling method for predicting the final filter response during design optimization. The method is based on the well known coupling matrix model. In order to demonstrate the design and modeling technique, a novel coupling structure for stripline filters is presented that results in substantial improvements in coupling bandwidth variation over an octave tuning range when compared to combline and interdigitated coupled line filters.

In order for a coupled resonator filter to produce an equal ripple Chebyshev response, each resonator of the filter must be tuned to precisely the same resonant frequency. Production tuned filters are routinely tuned in the lab and production environments by skilled technicians in order to compensate for manufacturing tolerances. However, integrated tunable filters cannot be tuned by traditional means since they are integrated into systems on circuit boards or inside front end modules. A fixed tuning table for all manufactured modules is inadequate since the required tuning accuracy exceeds the tolerance of the tuning elements. In this work, we develop tuning techniques for the automatic in-circuit tuning of tunable filters using scalar transmission measurement. The scalar transmission based techniques obviate the use of directional couplers. Techniques based on both swept and single frequency scalar transmission measurement are developed. The swept frequency technique, based on the Hilbert transform derived relative group delay, tunes both couplings and resonant frequencies while the single frequency technique only tunes the center frequency.

High performance filters necessitate high resonator quality factors. Although filters are traditionally treated as passive devices, tunable filters need to be treated as active devices. Tuning elements invariably introduce non-linearities that limit the useful power handling of the tunable filter. RF MEMS devices have been a topic of intense research for many years for their promising characteristics of high quality factor and high power handling. Control and reliability issues have resulted in a shift from continuously tunable devices to discretely switched devices. However, filter tuning applications require fine resolution and therefore many bits for digital capacitor banks. An analog/digital hybrid tuning approach would enable the tuning range of a switched capacitor bank to be combined with the tuning resolution of an analog tunable capacitor. In this work, a device-level position control mechanism is proposed for piezoresistive feedback of device capacitance over the device's tuning range. It is shown that piezoresistve position control is effective at improving capacitance uncertainty in a CMOS integrated RF MEMS variable capacitor.

Acknowledgements

The completion of the work presented in this thesis would not have been possible without the help and support of many people along the way. First, I would like to thank my supervisor Professor Raafat R. Mansour for his mentorship, guidance and support throughout the research work. His positive impact cannot be overstated. I would also like to thank my co-advisor, Dr. Ming Yu who was also very helpful and available whenever called upon.

I would like to thank the many members of the Centre for Integrated RF Engineering at the University of Waterloo who were my friends, co-workers and confidants for the last 5+ years. Thanks to Siamak Fouladi for always being available to listen, provide guidance and lend a hand; to Bill Jolley for providing his bountiful experience and expertise with RF measurement and assembly; to Neil Sarkar for his depth of knowledge about CMOS-MEMS; and Sara Attar for being a great office-mate and for always greeting me with a smile.

This thesis could not have been completed without the moral support of friends and family. Thanks to Susan Roy for enduring this long journey and providing her unwavering support; to my sister, Ines and my parents Sonja and Hamo for being there with a place to celebrate triumphs and vent frustrations. Finally, thanks to Neil Sarkar, Bill Jolley and Kyle Trainor for their company on breaks to recharge. Extra thanks to Bill Jolley and Kyle Trainor for their help with the proofreading of the first draft of the manuscript.

I would like to acknowledge the Canadian Microelectronics Corporation (CMC) for providing access to CMOS and UW MEMS fabrication services; and the Natural Sciences and Engineering Research Council (NSERC), the Ontario Graduate Scholarship and COM DEV for funding elements of this research.

Dedication

I dedicate this work to those that laid the foundation of opportunity that gave me a chance to pursue my dreams: from mountain peaks and stone walls to dams and generators; from a small town in the east to the city in the west—only the moon will do.

Contents

List of Tables

List of Figures

Chapter 1

Introduction

Multiband radios are a topic of significant recent interest due to increased demand for smartphones with global coverage and the sparse allocation of wireless spectrum for cellular applications. Current implementations of multiband radios result in duplicate hardware with a dedicated signal chain for each band. As the number of wireless standards and frequency bands grows, the costs associated with integrating a distinct front-end per band and standard become significant. The fixed radio frequency (RF) filters in the analog portion of the signal chain are significant stumbling blocks for the consolidation of multiple signal chains. Tunable filters are aimed at addressing the multiband problem by permitting a single component to handle multiple bands so as to combine multiple front-end signal chains into one. A single tunable analog signal chain with software defined baseband processing has the potential to reduce circuit area and result in more flexible and scalable multiband radios.

Tunable filters promise to enable frequency agile receivers and have been implemented using a variety of tuning elements including varactor diodes, radio frequency micro-electro-mechanical systems (RF MEMS), piezoelectric elements and paraelectric elements. Early work in the area of tunable filters focused primarily on tuning range. Recent research is directed at techniques to maintain the response of the filter as the center frequency is tuned. The initial technical challenge is in achieving low-loss and high quality factor (Q) from tunable filter structures. Considerable research is available in the area of miniature low-loss tunable filters [1] with substantial on-going research [2]. Once miniature tunable filters are made available, there remains the challenge of tuning such filters.

An enabling technology in modern electronics is the complementary metal-oxide-semiconductor (CMOS) integrated circuit. CMOS has become the de-facto standard technology for integrated electronics due to its low cost, low power consumption and long legacy in complexity scaling now famously known as "Moore's Law." The burden of controlling filter tuning elements will invariably fall on some flavor of CMOS circuit. The integration of high quality factor tuning elements and CMOS is of significant benefit. Combining the higher quality factors possible with RF MEMS, the integration and scaling of CMOS and tunability suggests significant potential for integrated RF MEMS tunable devices [3,4]. These tunable elements can enable reconfigurable single chip wireless front-ends resulting in smaller, more power efficient and less costly multi-standard radios.

1.1 Motivation

Global roaming is a challenging feature to implement due to the many different frequency bands defined for each region as shown in Table 1.1. Global roaming and multi-standard support has been achieved, for the most part, by integrating separate signal chains for each particular service and region supported by a particular device as shown in Fig. 1.1. An implementation approach using dedicated signal chains for each standard comes at the expense of circuit size, power consumption and reduced flexibility resulting in higher cost.

The concept of software radio attempts to address circuit flexibility by doing for wireless communications what software did for computing and information technology: create a universal system that is capable of addressing the needs of multiple services. Digital signal processing of microwave signals is prohibitively expensive and power inefficient in the GHz range. Therefore, analog signal processing of microwave signals using frequency translation and filtering would be required to reduce the digital signal processing burden to only the bandwidth of the signal of interest. The band selection flexibility calls for the use of tunable bandpass filters to ensure frequency band flexibility in software radio implementations.

Traditional filter theory has been rigorously developed for the design and synthesis of fixed frequency filter networks. The analysis and synthesis procedures for fixed frequency filters need to be extended to tunable networks to enable the systematic control of bandwidth and center frequency. Furthermore, methods to model tunable filters will

Table 1.1: Frequency bands as defined by the 3GPP [5].

Duplexing	Uplink (MHz)	Downlink (MHz)	Region
FDD	1920-1980	2110-2170	Europe, Asia
	1850-1910	1930-1990	Americas (Asia)
	1710-1785	1805-1880	Europe, Asia (Americas)
	1710-1755	2110-2155	Americas
	824-849	869-894	Americas
	830-840	875-885	Japan
	2500-2570	2620-2690	Europe
	880-915	925-960	Europe, Asia
	1749.9-1784.9	1844.9-1879.9	Japan
	1710-1770	2110-2170	Americas
	Frequency Range		
TDD	1900-1920		Europe, Asia
	2010-2025		
	1850-1910		(Americas)
	1930-1990		
	1910-1930		(Americas)
	2570-2620		Europe

also be needed in order to effectively determine whether a particular tunable network can cover the required states.

Once tunable filter networks become available there remains the problem of how to ensure precise performance from the device. Manufacturing process variations, long term drift and operating temperature can make precise tuning difficult. In traditional analog and RF circuits such issues addressed by operating devices in closed-loop with circuit performance tightly coupled to a precise reference such as a resistor or crystal oscillator. Such techniques have proven difficult to apply to RF MEMS due to the difficulty of integrating sensors into such small devices. One of the goals of this research is to develop methods to precisely control integrated microwave tuning elements in a MEMS context.

1.2 Objective

The objective of this research is to develop effective filter tuning techniques, tunable filter design methods and micro-scale integration techniques for closed-loop control of

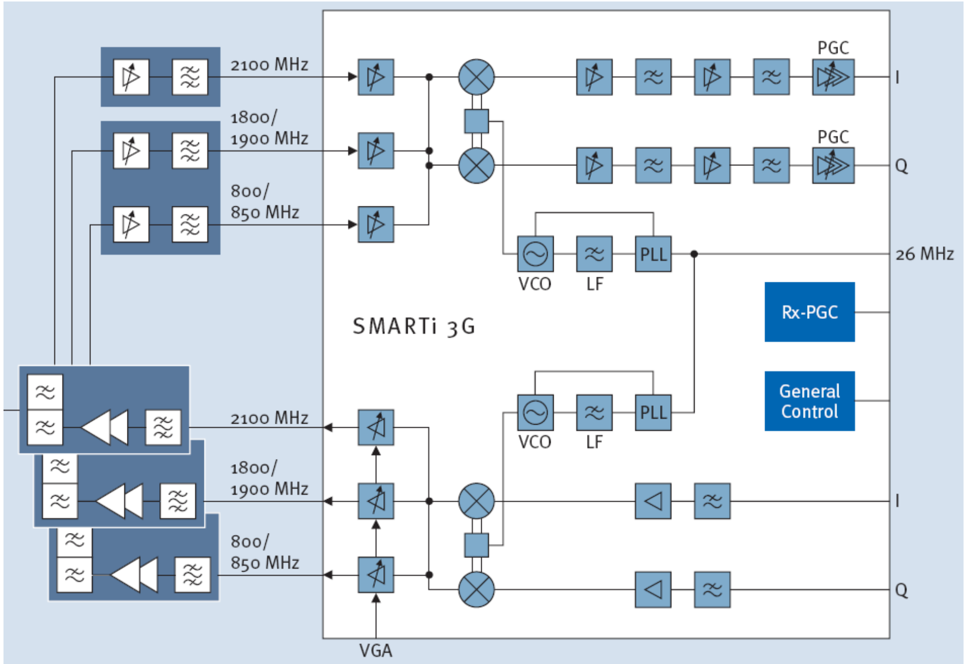

Figure 1.1: Block diagram of the PMB 5701 commercial transceiver from Intel (formerly Infineon): "the world's first single-chip multi-band UMTS transceiver IC" [6]

microwave filters and tuning elements. The ultimate goal is the monolithic integration of frequency agile RF MEMS components with characterization and tuning circuitry in order to guarantee predictable performance at the system level.

The primary focus of the research is on the design, modeling and control of tunable microwave elements and tunable filter networks. Tunable in the context of this work refers to in-circuit tunability as opposed to production tuning. In order to achieve these objectives in-circuit tunable and controllable filters and RF MEMS components are developed.

The research is divided into three key areas:

- **Tunable filter design and modeling techniques for controlled bandwidth**

  Conventional tunable filter design begins with the design of a filter at a nominal pass-band. The tuning element is added for control of center frequency with little analysis or design of the coupling variation across the filter's tuning range. The traditional approach results in substantial variation in return loss and bandwidth. In this work, a novel design technique is presented for tunable RF MEMS filters with controlled and predictable bandwidth variation. The design technique is presented alongside an analysis and modeling method for predicting the final filter response during design optimization.

- **Closed loop characterization methods and tuning techniques for automated in-circuit filter tuning**

  Production tuned filters are routinely tuned in the lab and production environments by skilled technicians in order to compensate for manufacturing tolerances. However, integrated tunable filters cannot be tuned by traditional means since they are integrated into systems on circuit boards or inside front-end modules. Look up tables of tuning voltages may also be inadequate since the required tuning accuracy exceeds the tolerance of the tuning elements. In this work, we develop tuning techniques for the automatic in circuit closed loop tuning of tunable filters using scalar transmission measurement.

- **Novel tunable RF MEMS components and stabilization**

  RF MEMS devices have been a topic of intense research for many years. Control and reliability issues have resulted in a shift from continuously tunable devices to switched devices. However, filter tuning applications require very fine resolution and therefore many bits for digital capacitor banks. An analog/digital hybrid tuning approach would enable the tuning range of a switched capacitor bank to be combined with the tuning resolution of an analog tunable capacitor. In this work, a device-level position control mechanism is proposed for piezoresistive feedback of device capacitance over the tuning range. It is shown that piezoresistive position control is effective at improving capacitance uncertainty in a CMOS integrated RF MEMS variable capacitor.

1.3 Organization

The study of the design, modeling, tuning device and tuning algorithm needed to occur in parallel in order for timely completion of the work. The position control of the MEMS varactor is presented in CMOS-MEMS technology. Due to the long cycle time of each fabrication run, the CMOS-MEMS device was studied first and required multiple fabrication runs. During periods of device fabrication the tuning algorithms of Chapter 3 were developed on screw tuned coaxial cavity filters with servo motor actuators. Finally, the filter design and modeling approaches for constant bandwidth were developed to complete the work by considering the tuning device and the control circuit in the design of the filter structure.

The frequency range from 3 GHz to 6 GHz was chosen due to the immediate availability of commercial wideband components in this band. A VCO, PLL and detector were all readily available for the prototyping of filter characterization hardware, and the dimensions of a planar filter implementation were reasonable for an integrated MEMS die. The work is presented in essentially the reverse order of that in which it was performed for a logical flow.

Chapter 1 introduced the concept of tunable filter control and outlines the motivation and objectives of this work. Chapter 2 contains a literature survey of the state of the art in tunable filters, tuning algorithms and tunable RF MEMS components. Section 2.3 of Chapter 2 briefly summarizes filter design theory based on the coupling matrix. Coupling matrix theory subsequently serves as the foundation for the research presented in Chapters 3 and 4.

Chapter 3 presents tunable filter design from the basis of coupling matrix theory. A novel constant coupling bandwidth structure in suspended substrate stripline technology is presented. Second and third order suspended substrate filters are presented and the design technique is validated by using a back annotated modeling approach to compare the coupling matrix model predicted response to the full-wave EM-simulated response. Design considerations for synchronously-tuned filters are presented in order to improve the performance of filters tuned by switched capacitor banks. Tuning performance is improved by ensuring that each resonator has the same center frequency versus capacitance characteristic.

Chapter 4 presents research on scalar transmission based tuning algorithms for the in-circuit tuning of microwave filters. Two approaches are presented. The first is based on the relative group delay of the transmitted signal that is derived from the Hilbert transform of the scalar transmission response. The relative group delay approach tunes both inter-resonator couplings and the center frequency. The second approach uses the magnitude of transmission at a single frequency. The second approach lends itself to high speed automated filter tuning but is not capable of tuning inter-resonator couplings.

Chapter 5 is dedicated to the control of MEMS tuning elements in CMOS using piezoresistive position sensing. The polysilicon gate material used for the fabrication of resistors and transistor gates in the standard CMOS process is used as a strain gauge for the position sensing of one plate of a CMOS-MEMS variable capacitor. It is shown that the mechanical position of the MEMS plate is a better indicator of RF capacitance than the control voltage in the presence of hysteresis and dielectric charging. The position sensing technique is proposed as a sensing scheme for the closed-loop control of RF MEMS variable capacitors.

Chapter 6 concludes the dissertation. It outlines the proposed future work, highlights the novel research contributions and lists the academic publications that were the product of the research.

Chapter 2

Literature Review

In this chapter a literature review of relevant material is presented. In Section 2.1, a literature review of tunable filters and filter tuning elements is outlined. Literature on tunable cavity filters, planar filters and tunable components is presented.

In the following section, Section 2.2, a literature review on filter characterization and tuning is presented. Literature on filter control at the tuning element level, resonator level and the filter level is discussed. The section on characterization and tuning is concluded with a review of filter tuning algorithms.

The final review section, Section 2.3, describes the coupling matrix model that is used extensively in the development of the material of Chapters 3 and 4. The material of Section 2.3 summarizes the necessary background for coupling matrix based filter synthesis and modeling.

2.1 Tunable Filters and Tuning Elements

In this section several different tunable planar and cavity filter designs will be highlighted. The section is split into two subsections—one on tunable cavity filters and the other on tunable planar filters.

Microwave filters can be constructed using a large array of technologies and are traditionally fabricated with tuning elements to compensate for manufacturing tolerances. The most popular tuning elements for cavity filters (waveguide, coaxial, dielectric resonator, etc.) are tuning screws [7]. In planar technologies trimming capacitors can be used though it is not uncommon to physically trim sections of microstrip line to achieve the desired tuning effect [8] or even to swap fixed capacitors. These tuning elements and techniques are applied during assembly and generally not adjusted after the filter leaves the factory.

This thesis is primarily concerned with filters of the post-production tunable type; i.e. filters that are intended for tunability after leaving the factory floor. Henceforth, the term *tunable filter* is reserved for use in this context and it will be made explicit where production tuning is being considered. However, many post-production tunable filter designs are based on traditional tuning screws or cavity deformations. Most tuning techniques that will be presented in the tuning techniques section were developed for production tuning and, in some cases, can be applied to in-circuit tuning as well.

2.1.1 Tunable Cavity Filters

Commercial post-production tunable cavity filters are adjusted by turning a Vernier knob such as the one shown in Fig. 2.1a. The knob is attached to a common shaft from which the tuning elements are coupled via a geared mechanism [9]. The bandwidth is usually fixed and is not adjustable [10]. The single tuning knob simplifies the use of the filter since it only requires adjusting one element. A picture of the BT series of tunable filters from K&L Microwave is shown in Fig. 2.1a. The off-the shelf version of the BT series has a 5-section Chebyshev response with a constant fractional bandwidth of 5% but can be customized for a fractional bandwidth from 1% to 10%.

Commercial filters with tuning knobs for each resonator are also available as shown in Fig. 2.1b [11]. However, these filters require the use of a vector network analyzer (VNA) to tune the filter and may require expertise to appropriately tune the N knobs for an Nth-order filter. Also, even the N-knob filters in [11] do not have direct control over the bandwidth since their N tuning knobs do not offer access to tune the $N - 1$ additional coupling values between the cavities.

Thus far all the tunable filters discussed have required manual tuning. Indeed, most of the commercially available tunable filters of this type do since they are intended for test and measurement, surveillance and niche wireless communications applications. The single Vernier knob tunable filters are also available in motorized versions with electronic general purpose interface bus (GPIB) interfaces [10] but they also do not offer tunable

(a) Tunable cavity filter from K&L Microwave with a single Vernier knob [10]

(b) Tunable cavity filter with individual tuning knobs [11]

Figure 2.1: Tunable cavity filters from K&L Microwave and Wainwright Instruments GmbH [11]

bandwidth. The bandwidth of these mechanically tunable filters is often fixed relative to the center frequency; i.e. their percentage bandwidth is fixed. The absolute bandwidth of this class of filters varies with the center frequency.

A fourth order dual-mode elliptic tunable cavity filter was presented in [12]. The filter was tuned using a micrometer to deform a bellows at one end of the filter cavity. The filter was designed for a fixed characteristic versus center frequency and resulted in a measured Q in excess of 8000. The inter-resonator couplings were designed such that the absolute bandwidth was maintained constant as the filter was tuned. The tuning range was less than 4.4% and the bandwidth variation was 3.5% using an offset iris design. The return loss was better than 15 dB over most of the tuning range. Electronic tuning would be conceivable in such design using a motor to drive the micrometer.

Electronic tuning of cavity filters is done by modifying the field within the cavity using an electronic actuator that disturbs the fields inside the cavity. These actuators can be constructed with simple stepper motors [13] or even piezoelectric actuators as shown in the dual mode dielectric resonator tunable filter shown in Fig. 2.2 [14].

A piezoelectric tuning mechanism was also used in a series of works on highly loaded evanescent coupled cavities. Much of the series was part of the DARPA Analog Spectral Processors project with the more recent work being sponsored by DARPA under the deservedly named Purdue Microwave Reconfigurable Evanescent-Mode Cavity Filters

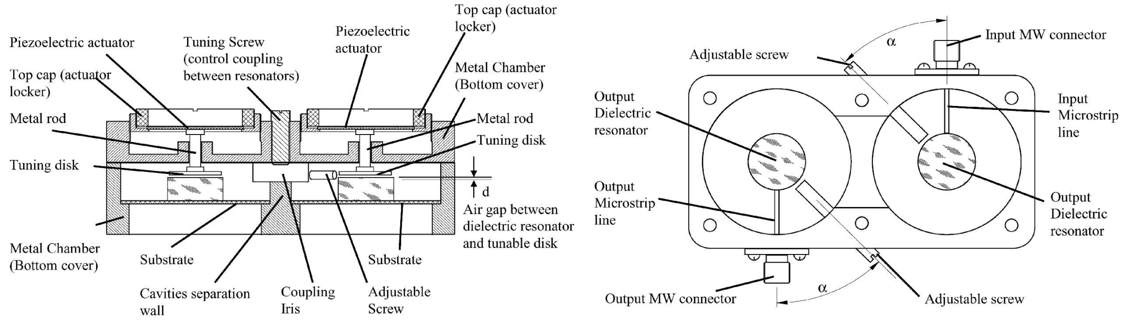

(a) Lateral view (b) Top view

Figure 2.2: Piezoelectric actuator tuned dual mode resonator 4-pole filter [14]

Study. The highly loaded structures resemble coaxial filters and are tuned by adjusting a capacitive gap at the open end of the coaxial post. Initial designs used piezoelectric actuators that deformed a copper-clad circuit board membrane that was soldered on top of a low temperature co-fired ceramic (LTCC) circuit [15]. Subsequent designs were based on a substrate integrated technique. A radial array of vias form the coaxial cavity wells and a metal patch on the top side is grounded by an array of vias to the bottom to form the loading post as shown in Fig. 2.3. The substrate integrated design is tuned by a round metalized piezoelectric actuator mounted directly onto the printed circuit board (PCB) carrier as shown in Fig. 2.4. Input coupling is achieved from the back side with a co-planar waveguide (CPW) feed. Inductive slots are use to normalize input coupling across the tuning range [16,17]. Unloaded quality factors (Q_u) between 250 and 650 have been demonstrated over an octave tuning range.

The resonators have been studied in multiple designs including tunable bandwidth filters [16], triplexer [18], reconfigurable order filters [19] and bandpass to bandstop switchable filters [20]. Tuning elements for the evanescent mode cavities based on micro-electro-mechanical system (MEMS) technology using both electrostatic [21] and magnetostatic actuation [22] have also been demonstrated. The primary advantage of the MEMS implementation is the elimination of hysteresis which can be detrimental to the repeatable tuning of the filter. Ultimately, the work has culminated in the field programmable filter array (FPFA). Analogous to a field programmable gate array (FPGA) in the digital domain, the field programmable filter array permits an arbitrary arrangement of coupled resonators to realize filters of varying order, transmission zeros, bandpass or bandstop response [23].

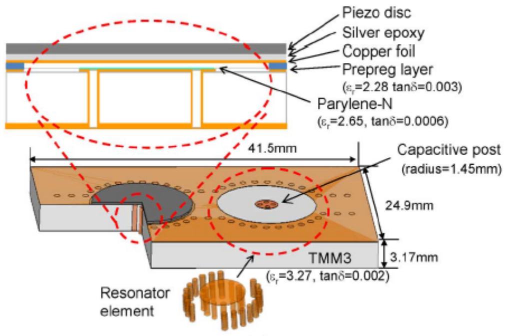

Figure 2.3: A cross-section of a two-coupled resonator circuit using an evanescent mode substrate integrated resonator structure tuned by piezoelectric actuators. [17]

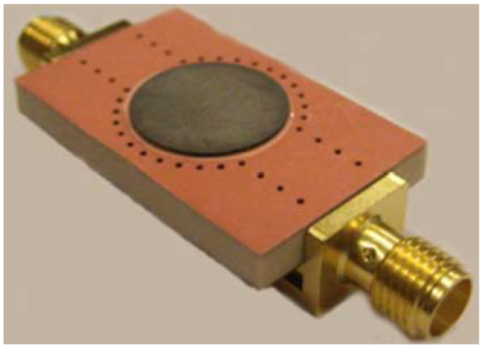

Figure 2.4: A photograph of a single resonator test circuit with SMA launches. [17]

2.1.2 Tunable Planar Filters

Tunable cavity filters are easily tuned by mechanical means due to their large size. Inserting an electrically or magnetically visible material into the cavity invariably results in frequency shift. The size of the tuning elements also make tunable cavity filters more expensive since they require mechanical actuators. Planar filters are more difficult to tune with tuning screws since the electric field tends to be trapped inside the dielectric. The use of tuning screws on planar filters is thus limited to fine tuning during production [24].

Planar filter technology is highly attractive for tunable filters due to its relatively small size and ease of integration with active components. Planar fabrication also results in lower cost and is amenable to mass production. Variable capacitors are the most common tuning element in printed and integrated circuit technology. Electronically tuned variable capacitors can be implemented using several different technologies. Semiconductor varactors are the most common [25–28] with significant research attention in MEMS [29–32] and barium strontium titanate (BST) tunable capacitors [33–35]. The trade-offs between the three are many including cost, linearity (intermodulation distortion [36]), Q-factor and tuning range. MEMS technology is the most promising overall but suffers from substantial manufacturing challenges that have thus far resulted in high costs. BST is particularly attractive since it has improved reliability and reduced packaging requirements. Commercial availability of BST materials is still fairly limited. Semiconductor

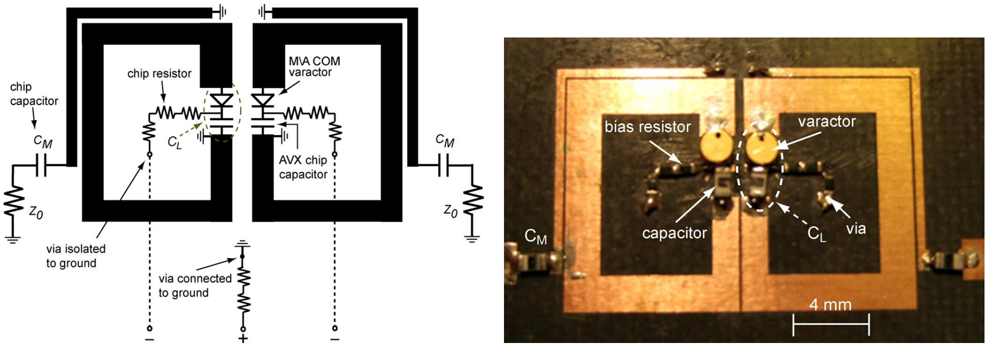

(a) Schematic (b) Photo

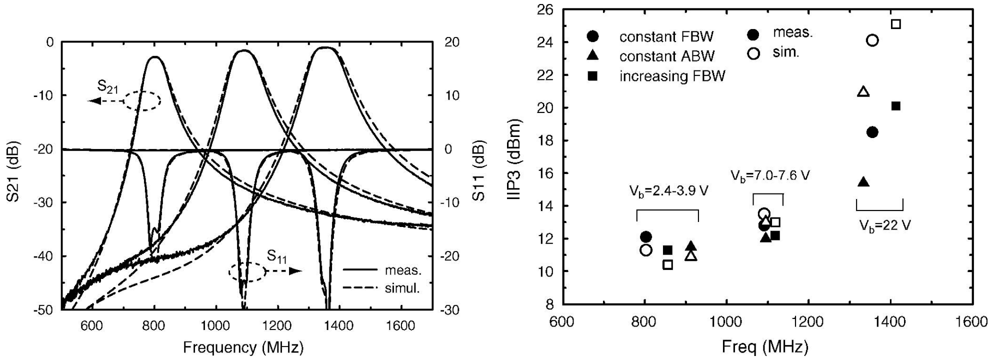

(c) Filter response (d) IIP3

Figure 2.5: Schematic, photograph, response and IIP3 of the diode tuned filter with constant absolute bandwidth from [28]

varactors are common but have relatively low Q-factors at higher frequencies and have lower linearity than MEMS and BST.

Three tunable filters were presented in [28] with increasing, decreasing and constant bandwidth vs. center frequency. All three tunable filters are Schottky diode tuned and use quarter-wave split ring resonators by grounding one end of the split. The presented coupling approach results in hybrid magnetic and electric coupling between the resonators that permits prescribed bandwidth tuning characteristics. The achieved quality factor varies from about 50 at the lower frequencies up to 150 at higher frequencies and bias voltages. Since the filters are tuned using varactor diodes, the power handling also varies with diode bias due to increased capacitance sensitivity and fractional bandwidth variation. A narrower bandwidth results in a higher external quality factor with increased voltage swing at the diodes resulting in higher non-linearity [28]. The tuning response of the constant fractional bandwidth type of filter and the input third order intercept point

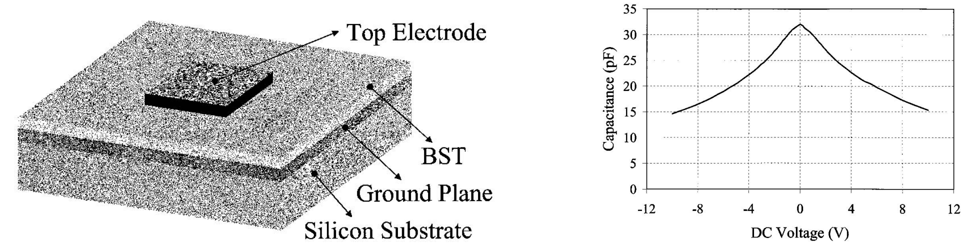

(a) Schematic cross-section of a BST MIM capacitor

(b) Measured capacitance vs. voltage characteristic for a BST capacitor

Figure 2.6: BST variable capacitor schematic and C-V curve [37]

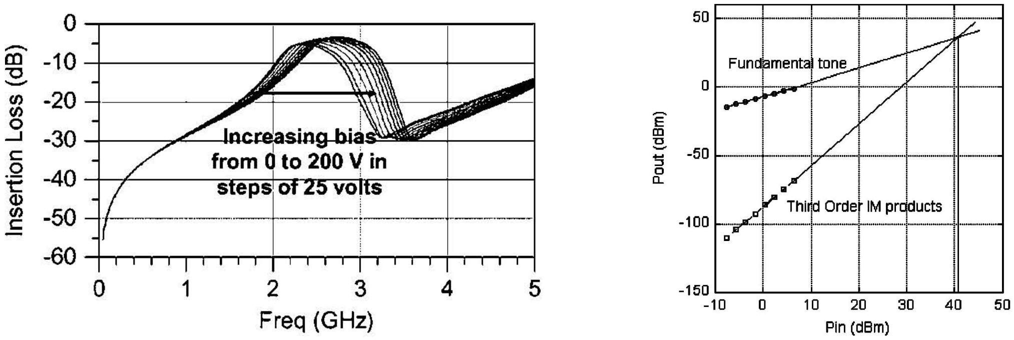

(a) BST tuned filter tuning range

(b) IIP3 response of a BST tuned filter

Figure 2.7: BST tunable filter response and IIP3 [38]

(IIP3) of all three is shown in Fig. 2.5. Note that the IIP3 of all three designs is below 26 dBm and therefore below the capability of the MEMS and BST examples shown below. The design presented in [28] proposes broadside coupling for filters of order greater than 2 making higher order filters difficult to implement.

A schematic illustration of a BST metal-insulator-metal (MIM) varactor and its C-V characteristic from [37] are shown in Fig. 2.6. A tunable combline bandpass filter tuning response and IIP3 is shown in Fig. 2.7 [38]. The response in Fig. 2.7 shows 5 dB insertion loss and an IIP3 of 40 dBm which exceeds the 21 dBm maximum IIP3 of the varactor tuned design shown in Fig. 2.5. The higher linearity is due, at least in part, to the high bias voltage of up to 200 V. High linearity with lower biasing voltages can be achieved by using a series stacking technique as shown in [39].

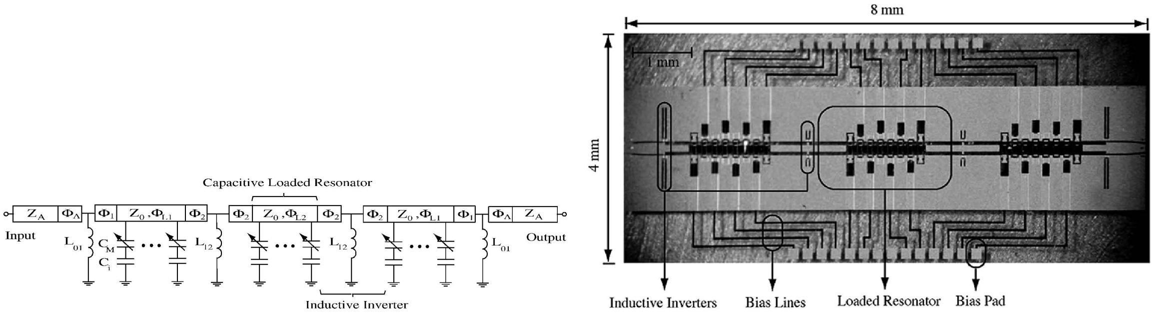

(a) Schematic (b) Photo

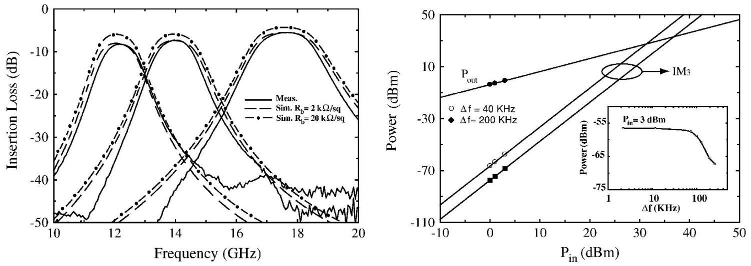

(c) Tuning range (d) IIP3

Figure 2.8: MEMS tunable filter schematic, photo, response and IIP3 [40]

In Fig. 2.8 a three-pole 4-bit tunable RF MEMS filter designed at 12-18 GHz is shown [40]. The unloaded Q varies between 30-45 but is expected to be higher with a more resistive bias configuration. The measured tuning results and intermodulation curves are shown in Fig. 2.8d illustrating that MEMS based technology has a power handling capability comparable to BST with a much higher applicable operating frequency. The tuning results in Fig. 2.8c are for three of the sixteen possible tuning states. The remaining states follow the same trend. Also, the tuning curve shows the potential performance improvement if biasing lines with higher resistivity are used. The IIP3 in this case is better than 30 dBm for a tone spacing of 40 kHz. The IIP3 is quoted as improving beyond 77 dBm at tone spacings above 2 MHz and exceeds the BST design shown in Fig. 2.7.

The majority of this proposal focuses on MEMS implementations of tunable filters due to availability of expertise, the wide applicable frequency range, power handling, Q-factor, scalability and CMOS integration. While BST shows promise up to 2 GHz its quality factor degrades with frequency while MEMS devices hold promise up to tens of GHz and millimeter-wave [41].

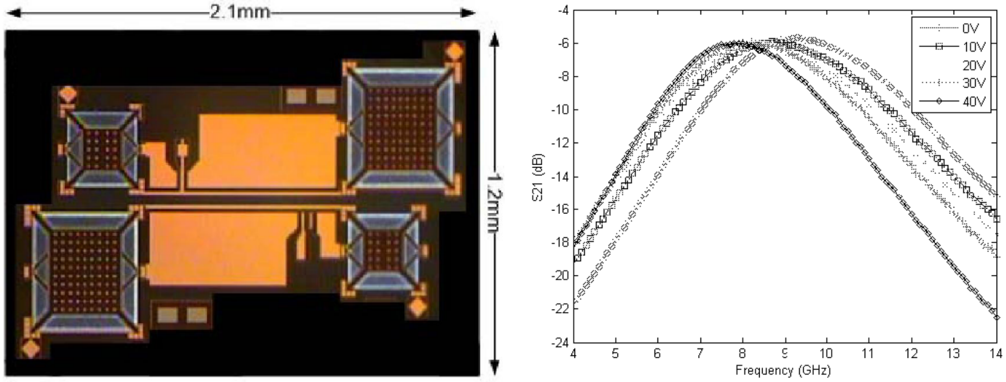

(a) Optical micrograph (b) Tuning response

Figure 2.9: Optical micrograph and tuning response of a CMOS MEMS tunable filter

A CMOS MEMS tunable filter is presented in [42] that has an insertion loss of 6 dB over the entire tuning range of 17% from 9.5 GHz. The optical micrograph and response are shown in Fig. 2.9. The tunable elements have enhanced Q through substrate etching, however, the transmission lines are not suspended and are still subject to substrate loss.

2.1.3 Tunable Filters with Controlled Bandwidth Variation

Tunable filters usually exhibit bandwidth and return loss variation as their center frequency is tuned. The bandwidth variation is usually nearly constant in a fractional sense with respect to center frequency. In other words, the fractional bandwidth remains relatively constant. Filters that exhibit a constant fractional bandwidth with respect to center frequency include [25, 32, 40, 43–45] and many more. A constant fractional bandwidth is relatively easy to implement as it is often a natural result of introducing tunability to coupled resonator filters.

Recently, further attention has been paid to the control of bandwidth variation across the filter's tuning range. Bandwidth control has been implemented using both direct methods, with tunable bandwidth, and indirect methods, where the bandwidth is determined by center frequency tuning. Filters with controlled bandwidth and center frequency are referred to as tune-all filters.

At this point it is important to consider the definition of bandwidth. Figure 2.10 illustrates two of the more common definitions of bandwidth for microwave filters. Equal-

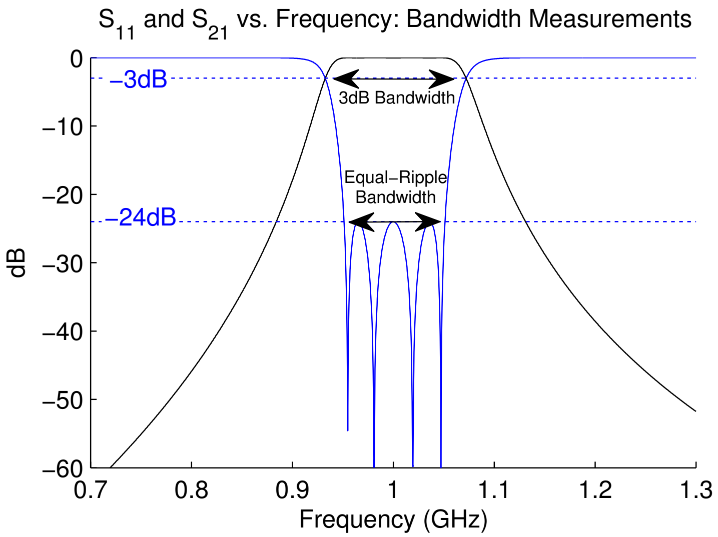

Figure 2.10: Illustration showing the 3dB and equal-ripple bandwidth criteria for bandwidth measurement.

ripple bandwidth is measured as the bandwidth of constant return minimum return loss. The loss-less filter specification shown in Fig. 2.10 has an equal-ripple bandwidth of 500 MHz and its filter function is directly synthesized from this specification. Equal-ripple bandwidth is commonly used in the context of design and for the design specification of high-performance filters. However, in tunable filters the return loss tends to vary substantially with center frequency and it therefore becomes an inconvenient measure. Instead, 3 dB or in some cases1 dB bandwidths are used since the selectivity or insertion loss of the filter is of primary concern. In the context of tunable filters we will use the 3 dB bandwidth as the definition.

The first proposed constant bandwidth tunable filter approach was published in [46]. The bandwidth control method relies on the use of stripline resonators with a prescribed phase length in a combline configuration. The resonators are capacitively loaded such that the phase length of the resonators is 53° in the middle of the tuning range. The inter-resonator coupling across the tuning range resembles an inverted parabola with a maximum bandwidth near the middle of the tuning range and minimum bandwidth at the extremes.

The use of a prescribed phase length for coupling was generalized in [47] by controlling the phase length of the coupled sections between adjacent microstrip resonators. The discrepancy between even and odd mode phase velocities was taken into account and both half-wave and quarter-wave structures were explored. The paper concludes with the demonstration of a three-pole microstrip tune-all filter with a center frequency tuning range from 600 MHz to 1.4 GHz and tunable bandwidth from 0 MHz to 120 MHz. The filter with tunable bandwidth and center frequency required the use of eight varactors for a third order filter due to the use of half-wave resonators and tunable input coupling. In contrast, a constant bandwidth design would only require three tuning elements for a third order filter. The controlled phase length coupling approach was also used in [48] showing excellent constant bandwidth performance. However, the approach presented in [48] relies on a coupling structure that may not be extensible beyond second order filters.

A constant bandwidth design using stepped impedance microstrip resonators was presented in [49]. The measured performance was reported over a small tuning range of 12% and the bandwidth variation was only quoted at two frequencies which is inadequate when the bandwidth variation is parabolic. However, the approach is very effective and was independently confirmed by our own simulations. The bandwidth variation at the two measured states was quoted as 3.2% for a tuning range of 12.5%.

A constant absolute bandwidth was also achieved in the microstrip filters presented in [28, 50]. The work in [28] demonstrated three different bandwidth characteristics including constant fractional bandwidth, constant absolute bandwidth and increasing fractional bandwidth. However, it requires coupling two quarter wave folded C-shaped resonators at their open ends making extension to higher order filters difficult. In [50] a corrugated resonator is used to manipulate the even and odd mode phase velocities in order to achieve constant coupling bandwidth. The combline structure with corrugations makes it easy to extend to higher order filters. However, the corrugations also reduce the overall coupling making the structure suitable for relatively narrowband filters.

2.1.4 RF MEMS Tunable Components for Filter Tuning Applications

The tunable capacitor is the most frequently used tuning element in planar technologies. Although several attempts have been made at fabricating miniature tunable inductors for RF applications [52], they tend to suffer from low Q-factors (less than 50) and high levels of complexity that make them generally ill-suited for filter applications.

Tunable RF MEMS capacitors come in three main flavors. These are digital [53], linear [53, 54] and a combination of the two called multi-step [55]. These classifications determine the shapes of their respective capacitance-voltage (C-V) curves. A digital capacitor is designed to operate in two stable states as shown in Fig. 2.11b while a linear capacitor is designed to approximate a capacitance that is proportional to the applied control voltage as shown in Fig. 2.11a. The multistep capacitor C-V curve is shown in Fig. 2.11c. It is designed for a multistable response with n discrete capacitance levels. When n is large, the multistep capacitor can be designed to approximate linear tuning [56]. Implementations are relatively straight forward and most reliable for the digital capacitor and hence this implementation has garnered the most commercial interest [3,4].

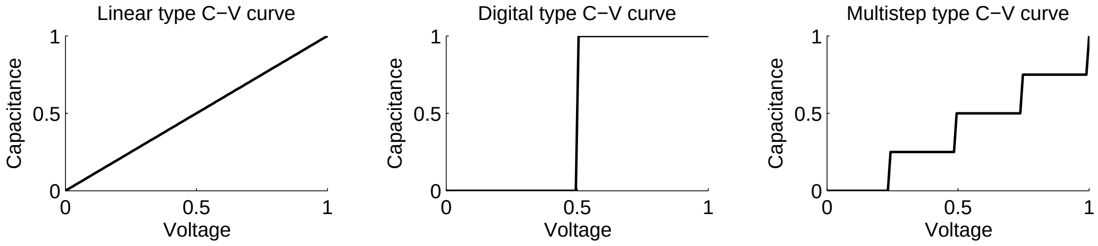

(a) Linear (b) Digital (c) Multistep

Figure 2.11: RF MEMS varactor normalized characteristic C-V curves

The principles of actuation of all three types vary but the most common are ther-

Table 2.1: Summary of Tunable Filters with Constant Bandwidth

Ref.	f_0	Tuning Range	BW	BW Var.	Poles-Zeros	Year
[46]	4 GHz	± 21.25%	200 MHz	± 12.3%	2	1982
[49]	2 GHz	± 6.25%	100 MHz	± 3.2%	4	2004
[28]	1.08 GHz	± 15.7%	43 MHz	± 7%	2	2008*
[50]	1.6 GHz	± 17.5%	112.5 MHz	± 4.9%	2	2010
[48]	0.8 GHz	± 19.3 %	80 MHz	± 4.4% (1dB)	2-2	2010*
[48]	0.78 GHz	± 19.2 %	60	± 5.0% (1dB)	2-2	2010*
[51]	1.7 GHz	± 15%	215 MHz	± 4.7%	2-2	2011*

* Difficult to extend beyond order 2.

Parameter	Thermal	Electrostatic
Linearity	Good	Poor
DC Power	High	None
Deflection	High	Low
Voltage	Low	High
Current	High	Low

Table 2.2: Thermal vs. electrostatic actuation of RF MEMS varactors

mal [57] and electrostatic. Piezoelectric [58] and magnetic actuation [59] have also been applied to RF MEMS to a lesser degree since they often suffer from high power consumption or integration challenges. In the case of digital capacitors electrostatic actuation is the most common. Electrostatic actuation has an inherent instability that results in a bistable response and the actuation method requires low energy. Linear capacitors, on the other hand, are often tuned using thermal actuators but suffer from high DC power consumption throughout their tuning range. As a result, significant work has been done on linearizing the behavior of electrostatic actuators and varactors [55, 56, 60, 61]. The relative performance between electrostatic and thermal actuation principles is shown in Table 2.2.

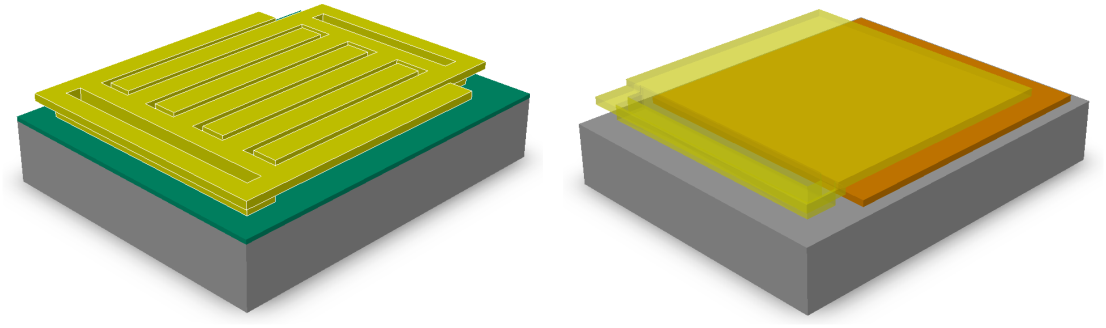

(a) Interdigitated

(b) Parallel Plate

Figure 2.12: The two most common capacitor configurations

The capacitor configuration is another key element that distinguishes RF MEMS varactor implementations. The configuration can be classified as either interdigitated [62] or parallel plate [55, 63] as shown in Fig. 2.12. The parallel plate configuration yields a higher self resonant frequency and Q-factor but is usually more difficult to fabricate than the interdigitated type as it requires the patterning of two metal layers. However,

Parameter	Parallel Plate	Interdigitated
Linearity	Poor	Good
Q Factor	Good	Poor
SRF	High	Low
Metalization	Two Layers	Single layer
Size	Small	Large

Table 2.3: Parallel plate vs. interdigitated capacitor configuration

when interdigitated structures are used for MEMS they tend to curl due to residual stresses in the structural layer. Therefore, they require high aspect ratios [62], low-stress processes [64] or special attention during design such as curl-matching [65]. Parallel plate configurations tuned by electrostatic actuation tend to show greater non-linearity in their C-V curves than the interdigitated thermally tuned type but are more compact for a given capacitance, have higher quality factors and self resonant frequencies. A comparison of parallel plate and interdigitated capacitor configurations is shown in Table 2.3. The parallel plate configuration is preferred in filter applications for its high Q factor, high self resonance frequency (SRF) and small size.

The CMOS MEMS parallel plate electrostatically actuated capacitor presented in [55] is shown in Fig. 2.13. This capacitor is fabricated by a mask-less post processing of a foundry fabricated CMOS chip. The process involves oxide, substrate and metal etching for device release resulting in two fully released structural layers in a four-metal CMOS technology. This allows for the fabrication of high-Q tunable capacitors as shown in Fig. 2.13b. This device was also used in the tunable filter described in [42] and shown in Fig. 2.9.

2.1.5 Substrate Etching

CMOS substrates are doped to have low resistivity to avoid issues with latch-up in digital circuits. The low resistivity substrate makes unmitigated substrate loss the dominant loss mechanism for microwave circuits on CMOS. In addition, the parasitic capacitance to the substrate drastically reduces the self resonance frequency of CMOS integrated microwave passive devices. Substrate removal techniques have successfully been employed in order to reduce the effect of substrate loss and enhance the Q of micromachined CMOS passive devices such as inductors [66, 67]. The substrate removal process can be accomplished

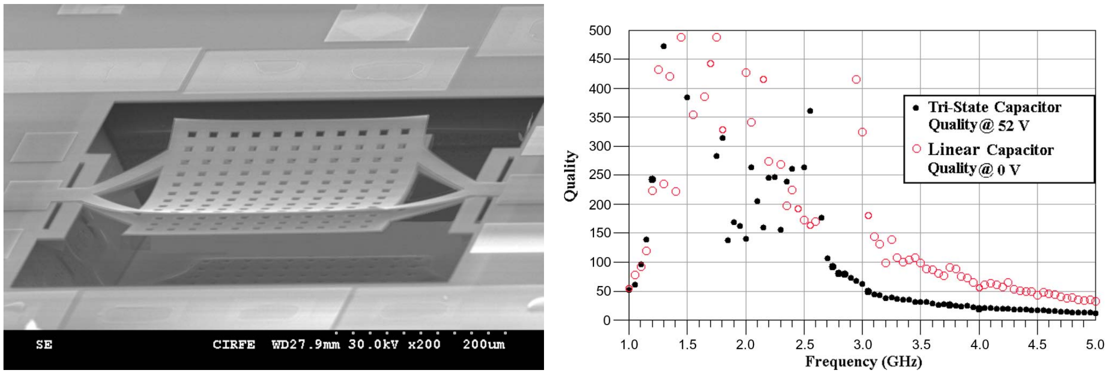

(a) Capacitor SEM picture (b) Quality factor at approximately 1 pF

Figure 2.13: SEM photograph and quality factor of the CMOS MEMS parallel plate electrostatically actuated capacitor presented in [55]

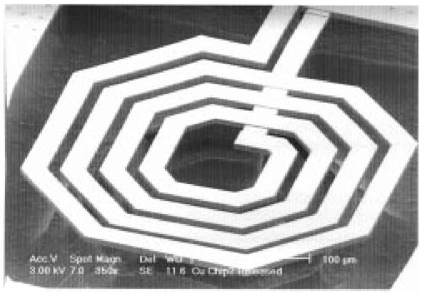

Figure 2.14: An example of an inductor with quality factor enhancement using substrate etching techniques

by wet etching using tetramethylammonium hydroxide (TMAH) [55] or dry RIE etching using SF_6 and/or CHF_3 [42]. Substrate removal techniques have been used to fabricate enhanced Q capacitors and inductors as shown in Fig. 2.13a and Fig. 2.14, respectively.

2.2 Filter Characterization and Tuning

In this section, the literature related to control of tunable filters will be discussed. The section is split into four subsections. The first three deal with three levels of control for a tunable filter. These are the tuning element level, resonator level and the filter level. The final section deals with the tuning algorithms for filter level tuning which warrants a section unto itself due to its complexity. In the rest of the introduction to this section auto-tuned filter networks are classified by their control topologies.

Filter tuning comes has several levels of complexity based on the measured parameter, measurement method and control approach. During the 2004 International Microwave Symposium a workshop titled "System Requirements and Review of Conventional Tuning Techniques" was presented [68]. The comprehensive presentation outlined the possible methods of implementing closed-loop filter tuning. Three classification categories of filter control and tuning methods were identified. The first is the measured parameter, the second is the measurement method and the third is the tuning algorithm. An extended summary of the measurable parameters, methods and algorithms are shown below.

Measurable parameters:

- **Direct filter measurement** — Involves switching between characterization and filtering modes. The measurement mode could involve the use of a frequency sweep or a single frequency tone to characterize the response of the filter.
- **Indirect filter measurement** — A secondary filter, for example, could be used in a Master-Slave arrangement to avoid the use of switching and enable continuous, uninterrupted filtering.
- **Resonator measurement** — Each resonator could be measured individually reducing the computational burden and simplifying algorithm design but increasing the number of switches required to isolate each resonator.
- **Tuner position** — This is an indirect measurement of filter performance and does not require any switching but does the least to guarantee overall filter performance.

Measurement methods:

- **Single-frequency reference signal** — A single reference tone is used to tune each resonator for maximum response at the center frequency.
- **Multi-frequency reference signal** — A multi-tone signal is used to reduce the number of necessary measurements.
- **Swept-frequency signal** — A series of measurements are performed similar to a network analyzer to determine the response of the filter over a frequency range.

- **Position sensing** — Position sensing of tuner position is used as an indirect measurement method.

Tuning algorithm:

- **Look-up table** — The filter is pre-characterized and the tuning states are pre-configured into the memory of the controller. Switching between states only requires the lookup of the requisite control signals from memory.
- **Optimization** — A goal function is established and an iterative algorithm employed to find optimal tuning voltages to minimize the value of the objective function.
- **Parameter extraction and space mapping** — Similar to optimization but the optimization is used to extract the model parameters and the correction is applied based on the extracted model [69, 70].
- **Fuzzy logic** — A fuzzy control algorithm is applied using a combination of tuning techniques defined using fuzzy methods [71].
- **Sequential techniques** — Sequential techniques include time domain tuning [72] and Ness's method [73, 74]. They attempt to reduce the multivariable optimization problem to a sequence of smaller one or two-variable optimization problems.

2.2.1 Device-Level Control

Device-level control is directed at controlling the tuning element itself and ensuring that its value is precisely set. In the case of variable capacitors the desire is to set the correct capacitance level at the frequency of interest. This can be done by measuring the capacitance directly or by indirect means such as measuring the position of the tuning element. The control may be required due to temperature drift or device non-linearity.

Since RF MEMS varactors are mechanical it seems reasonable that they can be controlled using servo-loops like other mechanical actuators requiring stabilization. Perhaps the most studied phenomenon in electrostatic MEMS actuation is the pull-in effect. Pull-in results in device collapse at $1/3$ of the initial gap and is a limiting factor in the displacement of electrostatic actuators. One of the more elegant solutions to pull-in was

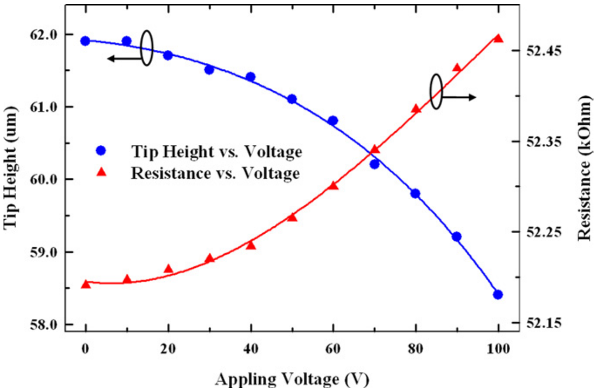

(a) Tip deflection and sensor resistance

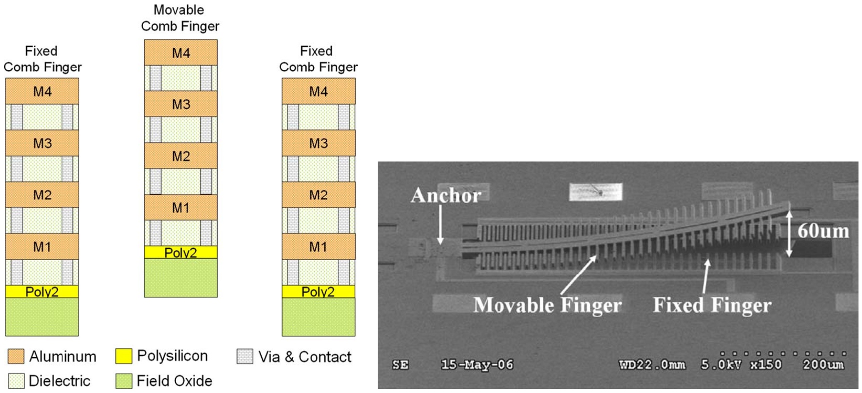

(b) Material stackup in the 0.35 μm CMOS process from TSMC

(c) SEM micrograph of the out-of-plane electrostatically actuated resonator

Figure 2.15: Piezoresistive position sensing in TSMC's 0.35 µm CMOS process [76]

proposed using capacitor feedback [75]. Its operation arises from a simple fixed capacitor placed in series with the electrostatic actuator. As the capacitance of the actuation capacitor increases with actuation voltage, its proportion of the overall voltage drops from a simple application of Kirchoff's law. This passive controllability comes at the cost of increased actuation voltage since the electric field across the actuator capacitor is reduced.

CMOS MEMS (CMOS MEMS) technology allows designers to integrate MEMS devices with active control electronics. Position sensing in CMOS MEMS is possible using traditional capacitive sensing which is prevalent in MEMS based accelerometers [65,77] or even integrated piezoresistive sensing as shown in [76]. The results from [76] are shown in Fig. 2.15. The resonator was fabricated using a 0.35 µm CMOS process from Taiwanese

Semiconductor Manufacturing Company (TSMC). The sensitivity of the piezoresistor is fair considering the very small deflection at the tip of the cantilever that would result in an even smaller strain in the actual resistor.

To our knowledge closed-loop control and feedback have not been directly applied to RF MEMS devices. However, the result from [76] is encouraging for the application of piezoresistive feedback to RF CMOS MEMS devices.

2.2.2 Resonator Based Tuning

A tuning approach proposed by Superconducting Technologies Inc. involves individually tuning each resonator to a precise resonant frequency [78]. This is an example of single-frequency resonator measurement and requires multiple reed-relay switches integrated into the filter housing to route the reference signal between each resonator and the detector. The number of switches is proportional to the number of resonators that need to be tuned and consequently the filter order. In both cases there are no dedicated tuners that tune the inter-resonator coupling. Instead, in the design shown in [78] the topology of the filter is optimized to result in a fairly constant filter bandwidth across the entire tuning range. Fig. 2.16 shows the two modes of operation for the filter described in [78]. In Fig. 2.16a the switches are set to disconnect the resonator from the input signal and apply a single tone reference. A signal is applied to one resonator at a time and the resonator is tuned until the maximum magnitude is received at the detector.

An elegant resonator-based tuning approach that permits continuous monitoring and control is the differential mode monitoring technique presented in [79]. The resonator is designed with a monitoring port that is coupled to an orthogonal resonant mode as shown in Fig. 2.17. The orthogonal mode is a higher order resonance and not to be confused with a degenerate mode of a dual-mode resonator. The field distributions of the fundamental (common) mode and higher order (differential) mode are shown in Fig. 2.18. The higher order mode is tuned by the same mechanism as the fundamental and therefore acts as an indirect indicator of the resonance frequency of the fundamental. The advantage of this technique is that the state measurement is performed at a frequency outside the intended operating band of the filter and should not interfere with the signal of interest. Continuous monitoring is thus possible. However, this monitoring method only yields a relative relationship between the fundamental and higher order mode and therefore does not guarantee absolute accuracy.

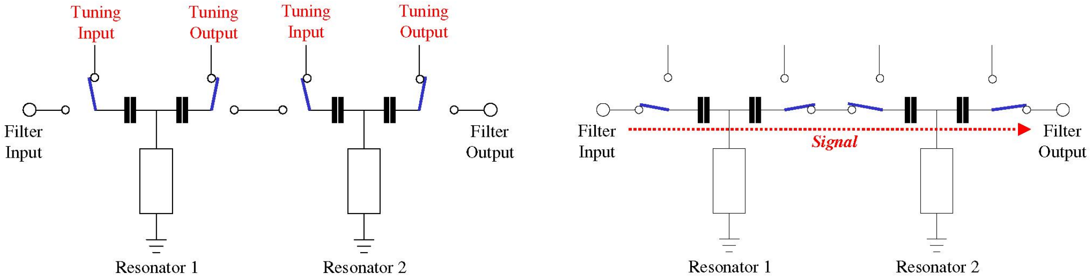

(a) Tuning mode (b) Filtering mode

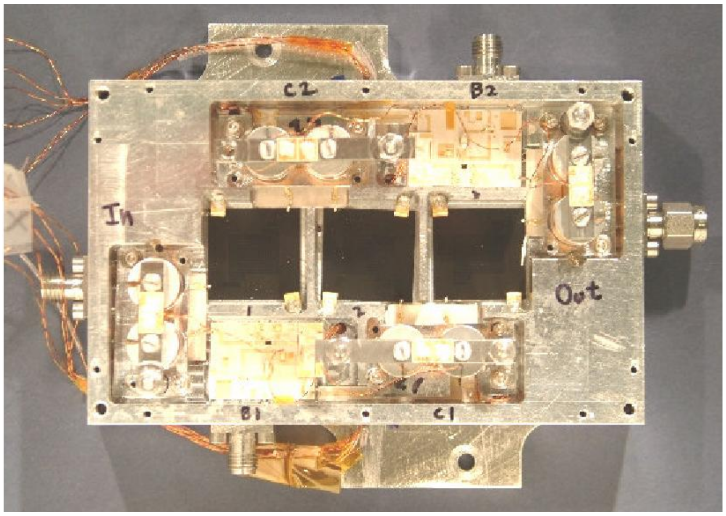

(c) Three-pole resonator tuned HTS filter with integrated switches and nano-position tuners

Figure 2.16: Automatically tuned filter with tuning of individual resonators

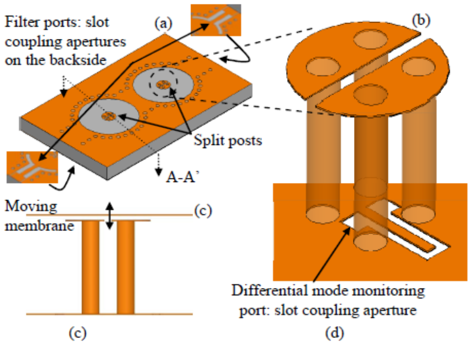

Figure 2.17: A CAD model of the resonator design. (a) Shows the two pole filter. (b) Shows the split resonator loading post. The tuning mechanism is shown in (c).

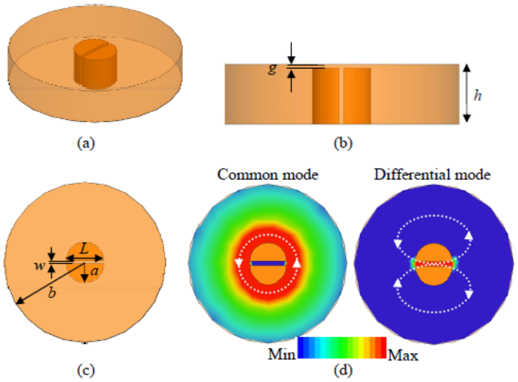

Figure 2.18: An EM model of the resonator (a-c) showing the field distributions of the common and differential modes of the cavity (d). [79]

An indirect position sensing scheme is integrated in the system demonstrated in [80] but is used primarily for servo feedback of the motor actuators. It is not clear if it used to indirectly determine the filter performance. It is conceivable that some coarse tuning could be applied when combined with a look up table. This design will be discussed in the following section.

2.2.3 Filter-Level Control and Automated Filter Tuning

One of the first examples of fully-automated production tuning of filters was presented in [81]. The tuning system was coined the RoboCAT or robotic computer aided tuning. The robot consists of a robotic arm suspended on a gantry that is capable of turning tuning screws mounted on a traditional screw-tuned filter. The tuning robot is substantial in size and is shown in Fig. 2.19. Such a system is limited to production tuning only. The tuning element is the classical tuning screw.

There are three key parameters for tuning coupled resonator filters. These are the frequencies of the resonators, the inter-resonator couplings and the input/output (i/o) couplings. By tuning the resonance frequency of the resonators the center frequency of the filter is adjusted while adjusting couplings affects the filter's bandwidth. The resonator frequency is usually very close to the center frequency of the filter while an

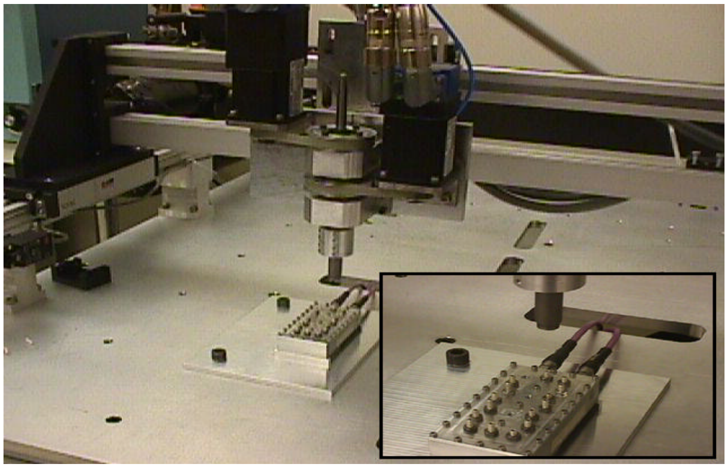

Figure 2.19: Robotic computer aided tuning (RoboCAT) used for tuning after assembly.

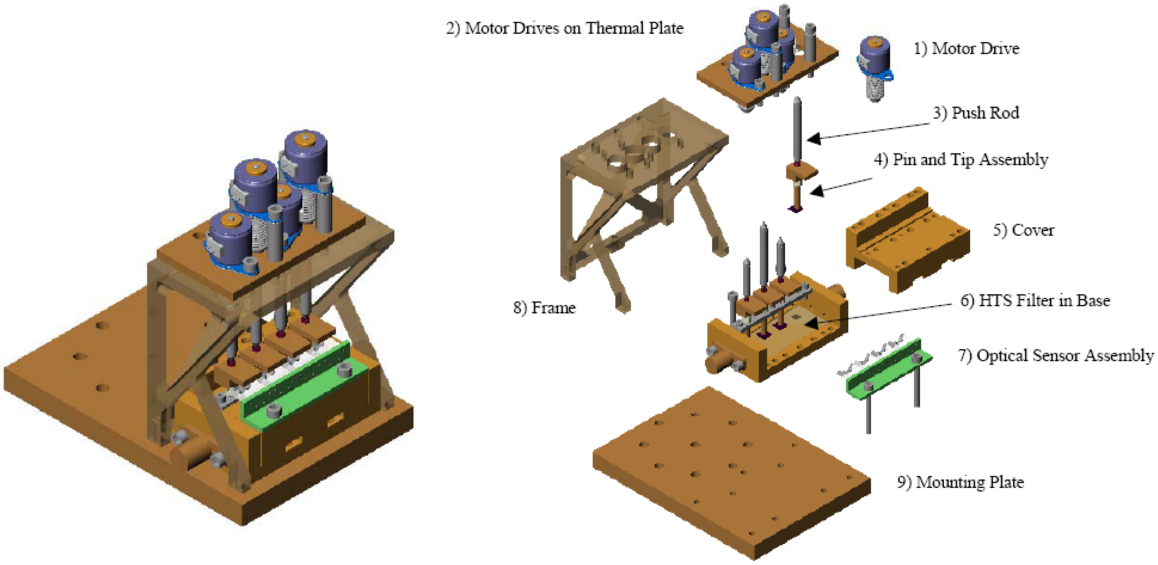

Figure 2.20: Tunable HTS filter with motor control [80]

increase in coupling yields a wider bandwidth and a lower coupling factor reduces the bandwidth.

A closed-loop filter tuning system is proposed in [80] using a swept frequency direct filter measurement system. The filter in [80] is a four pole microstrip HTS filter. The tuning is actuated using motor drives with HTS tuning elements that result in low loss. A picture of the configuration is shown in Fig. 2.20. The tuning time is exceptional requiring only 1 second, but the presentation does not indicate if this is a closed-loop response or a look up table response limited by actuator speed. The overall size of the filter alone is very large with the tuning actuators occupying much more volume than the filter itself.

Example implementations of the indirect filter measurement technique are demonstrated in [82] and [83]. In both cases a single-frequency reference is used to tune a master filter from which a tuning signal is derived and applied to a slave filter which can continuously filter a desired signal without switching. The filters under consideration in both [82] and [83] consist of only a single tunable element and result in a relatively simple implementation compared to the higher order filters considered in [78, 80]. Also, such solutions are not practical for filters that occupy a large area since the technique requires two identical implementations and thus double the volume.

2.2.4 Tuning Algorithms

In traditional tuning techniques a complete filter frequency response is measured using swept-frequency measurement such as that performed by a VNA. A tuning technician then applies a series of heuristics based on experience to adjust the tuning elements for a desired response. Experience derived heuristics or tuning methods and algorithms have long been sought after in the microwave filter design community to reduce the production tuning time and thus cost of high-performance filters. Such techniques are also applicable to automated electronic filter tuning as well. There are four main classes of tuning algorithms for microwave filters. These are: space mapping, parameter extraction, fuzzy logic, and sequential techniques.

Sequential techniques are methods that attempt to deterministically find tuning element positions one at a time [72, 73, 84–86]. These techniques are not completely sequential since it is difficult to fabricate filters with tuning elements that only affect a single filter parameter. A tuning screw that, by design, is only intended to affect the center frequency of a single resonator will invariably also cause some loading on an adjacent resonator. This results in the requirement for some iteration despite attempts at keeping the algorithm purely sequential. Two of the more recent and well-known sequential tuning techniques are the group delay tuning technique proposed in [73] and the time domain tuning technique proposed in [72, 85].

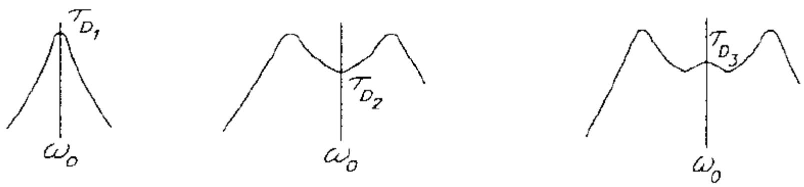

$$Q_E = \frac{\omega_0 \Gamma_{d1}}{4} \qquad k_{12} = \frac{4}{\omega_0 (\Gamma_{d1} \Gamma_{d2})^{1/2}} \qquad k_{23} = \frac{4}{\omega_0 \left[\Gamma_{d2} \; (\Gamma_{d3} - \Gamma_{d1})\right]^{1/2}}$$

$$\Gamma_{d1} = \frac{4 g_0 \; g_1}{\Delta\omega} \qquad \Gamma_{d2} = \frac{4 g_2}{g_0 \; \Delta\omega} \qquad \Gamma_{d3} = \frac{4 g_0 \; (g_1 + g_3)}{\Delta\omega}$$

Figure 2.21: The prototype group delay values for the group-delay based tuning of a 3-pole filter using the method proposed in [73]

The group delay technique follows a simple algorithm whereby each resonator is first shorted and then tuned one by one to achieve a symmetric response and a prescribed group delay of S_{11} at the center frequency. The prescribed group delay for each step can be determined from the lowpass prototype g-values and the prescribed bandwidth of the filter. The group delay values (Γ_d), external Q (Q_e), coupling coefficients ($k_{r(r+1)}$) and the expected group delay shape for a Chebyshev filter response at each step are shown in Fig. 2.21.

The time-domain tuning technique proposed in [72] also operates on the S_{11} response by performing an inverse Fourier transform on the vector S_{11} response and observing the obtained time-domain waveform. Intuitively, the time-domain response will initially display the effect of the first resonator then followed by the "downstream" resonators. In this way, the effects of each resonator and coupling element can be isolated in the time domain waveform. To tune each resonator, the nulls are first tuned in sequence to make them as deep as possible. Then, a golden filter or simulated model are used to set the inter-resonator couplings to establish the local maxima between the nulls. Fig. 2.22 shows the S_{11} and the time domain response for a filter with the second resonator detuned. Note that the second null, indicated by marker 2 in Fig. 2.22, is ill-defined and requires further tuning. Although nulls 3-5 are also shallow, the effect of a detuned second resonator will affect the rest of the "downstream" response. Therefore, the filter is tuned starting at the source terminal and proceeding towards the load. The time domain tuning technique

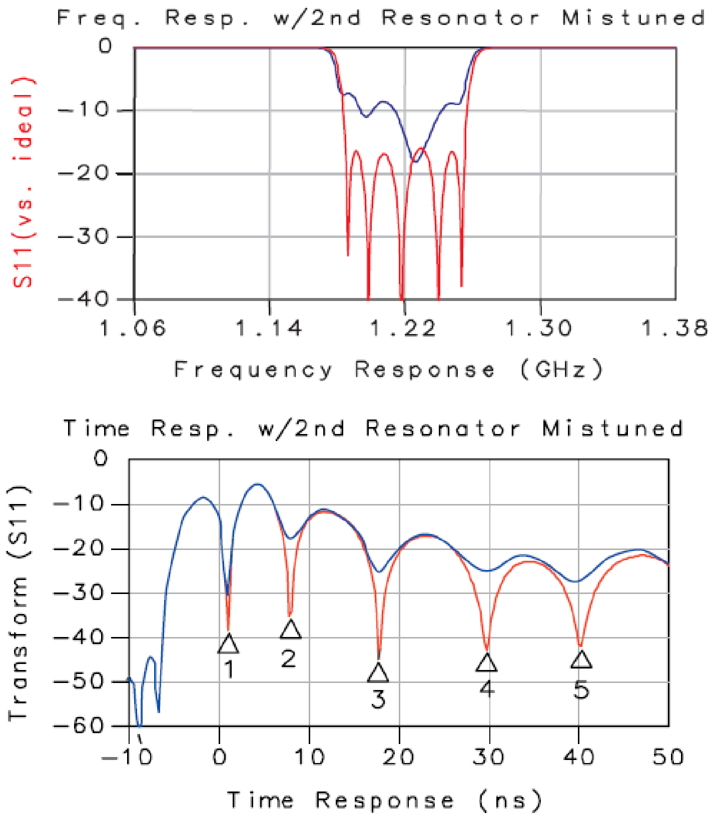

Figure 2.22: S_{11} magnitude and time domain response in the ideal (red) and second resonator detuned (blue) case [87]

works well for filters with a single path from input to output such as Chebyshev and Butterworth responses. Its applicability is doubtful, however, for filters with multiple paths from input to output such as elliptic, quasi-elliptic and self-equalized filters.

A heavily used model for coupled resonator filters is the coupling matrix since its elements have a physical correspondence to the elements of a coupled resonator filter. Knowing the exact coupling matrix for a measured response makes it possible to determine the elements that require tuning by comparing the extracted coupling matrix to a desired result. Deriving the coupling matrix directly from the scattering parameters is a challenging problem. There are several parameter extraction techniques to determine the coupling matrix from the measured S-parameters [88, 89]. Each technique does so to a varying degree of success. Once the coupling matrix is derived an error matrix can be calculated to determine which elements of the coupling matrix need to be adjusted for the measured response to match the desired response. Once again, a given tuning actuator will, to some extent, affect multiple elements of the coupling matrix and thus even with an accurate parameter extraction technique the tuning process is still iterative.

A highly promising implementation of tuning algorithms is fuzzy logic [71, 90]. Since there are a great number of interrelated variables in a filter tuning problem, deterministic models are difficult to define. However, it is easier to to say, for example, that a given tuning element will *mostly* affect the center frequency of a given resonator and only *somewhat* affect the adjacent resonators and inter-resonator coupling. Fuzzy logic techniques attempt to create a tuning algorithm from expressions such as *mostly* and *somewhat*. This makes fuzzy logic an excellent framework for formulating the tuning algorithm.

Space mapping is a design technique that relies on first having a physics-based coarse model of the tunable system [70]. When the measurement of a filter response is costly in terms of time such as electro magnetic (EM) simulation, space mapping serves to improve the efficiency of the calculation by optimizing at the circuit level on a physics-based coarse model. In this fashion the optimization loop occurs in a fast circuit simulator and the time-consuming EM simulation serves to adjust the discrepancy between the coarse surrogate model and the accurate fine model. Space mapping is therefore well suited for circuit design and its benefits are less clear for filter tuning since the measurement of a tuning step is less costly in a realized filter than in an EM simulation.

2.3 Coupling Matrix Background

The following chapters rely heavily on concepts derived from coupling matrix synthesis and design. Due to the heavy use of coupling matrix concepts it is pertinent to review some of the material here.

The coupling matrix was first introduced for the design and analysis of narrow-band multi-coupled resonator filters. It was particularly useful for relating elliptic filter functions to the physical design of coupled cavity circuits [91]. Techniques relating to filter design using the coupling matrix have since been presented in great detail in [92].

The coupling matrix form used in this work is based on the low-pass NxN coupling network shown in Fig. 2.23. The network shown in Fig. 2.23 has been illustrated as an

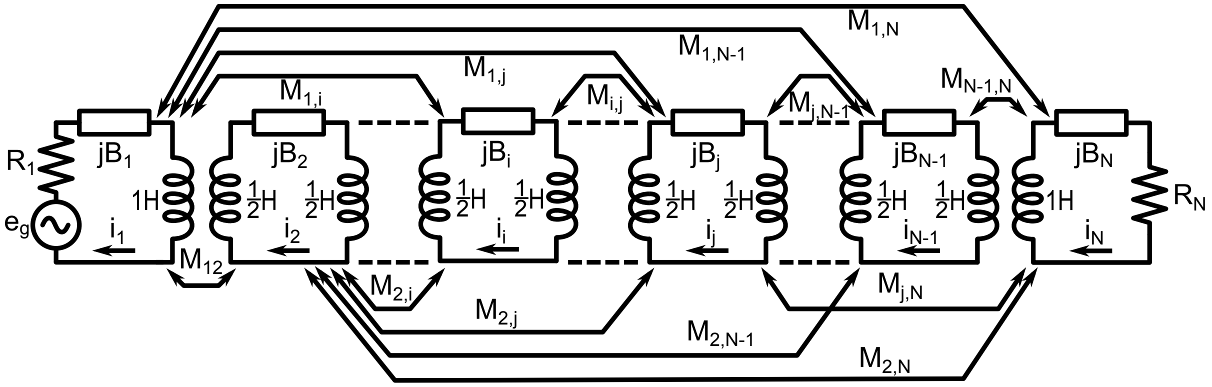

Figure 2.23: Low-pass circuit diagram of the coupling matrix. Generally, all cross-couplings exist. Only a subset are shown.

impedance network. A dual network with an admittance formulation also exists and is illustrated in [93]. The inductors are normalized to unity for a low-pass cut-off of 1 rad/s.

The generic circuit diagram of Fig. 2.23 describes an arbitrary low-pass circuit of Nth order interconnected with frequency invariant couplings M_{ij} and augmented with frequency invariant reactances B_i. The couplings in the low-pass domain are modeled as frequency invariant inverters while in the bandpass domain they are transformed into frequency invariant mutual capacitances or inductances, respectively. The elements labeled B_i permit the design of asymmetric frequency responses and appear as self-couplings along the main diagonal of the coupling coupling matrix; i.e., $M_{ii} = B_i$. The frequency invariant reactances B_i effectively offset the resonance frequency in the bandpass domain. The resonance frequency shift is used in Chapter 4 to model the effect of tuning each resonator.

In the narrowband case, the limitations of the frequency invariant couplings and frequency invariant reactances are negligible; the coupling is approximately constant across the band of interest and the frequency invariant reactances merely shift the nominal resonance frequency. In the wideband case, coupling variation across the band needs to be taken into account [94].

The NxN low-pass circuit of Fig. 2.23 can be solved for its terminal characteristics by writing the loop equations in matrix form as (2.1). S-Parameters may also be related directly by solving for the incident and reflected waves of the impedance matrix as given in (2.2) where the complex frequency variable $s = j\omega$ has been substituted by the low-pass angular frequency variable λ. The low-pass response can be transformed to the bandpass domain using the low-pass to bandpass transformation given in (2.3).

$$e_g[1,0,0,\cdots,0]^t = [j\boldsymbol{M} + s\boldsymbol{I} + \boldsymbol{R}]\cdot[i_1, i_2, i_3, \cdots i_N]^t \tag{2.1}$$

$$\begin{aligned} S_{11} &= 1 + 2jR(\lambda\boldsymbol{I} - j\boldsymbol{R} + \boldsymbol{M})^{-1}_{1,1} \\ S_{21} &= -2jR(\lambda\boldsymbol{I} - j\boldsymbol{R} + \boldsymbol{M})^{-1}_{N,1} \end{aligned} \tag{2.2}$$

$$\lambda = \frac{f_0}{\Delta f}\left(\frac{f}{f_0} - \frac{f_0}{f}\right) \tag{2.3}$$

A sample coupling matrix for a fourth order Chebyshev filter with 23 dB return loss is shown in (2.4). The low-pass angular frequency response is shown in Fig. 2.24a and the bandpass transformed response is shown in Fig. 2.24b at a center frequency of 1 GHz with a bandwidth of 10 MHz where the bandwidth is defined as the equal ripple bandwidth.

$$\boldsymbol{M} = \begin{bmatrix} 0 & 0.9860 & 0 & 0 \\ 0.9860 & 0 & 0.7411 & 0 \\ 0 & 0.7411 & 0 & 0.9860 \\ 0 & 0 & 0.9860 & 0 \end{bmatrix} \quad \boldsymbol{R} = \begin{bmatrix} 1.2222 & 0 & 0 & 0 \\ 0 & 0 & 0 & 0 \\ 0 & 0 & 0 & 0 \\ 0 & 0 & 0 & 1.2222 \end{bmatrix} \tag{2.4}$$

The coupling matrix can also be directly synthesized from polynomial synthesis using techniques detailed in [92]. The polynomial form of the fourth order filter with no transmission zeros (all transmission zeros at infinity) is given in (2.5). In this case, the polynomials are all functions of the complex frequency variable s and are related to the S-Parameters as given (2.6).

$$\begin{aligned} P(s) &= j \\ F(s) &= s^4 + s^2 + 0.125 & \epsilon &= 0.5678 \\ E(s) &= s^4 + 2.4444s^3 + 3.9875s^2 + 3.7190s + 1.7657 & \epsilon_r &= 1 \end{aligned} \tag{2.5}$$

$$S_{11}(s) = \frac{F(s)}{\epsilon_r E(s)} \quad S_{21}(s) = \frac{P(s)}{\epsilon E(s)} \tag{2.6}$$

The coupling matrix algorithms for the synthesis of filter polynomials and coupling

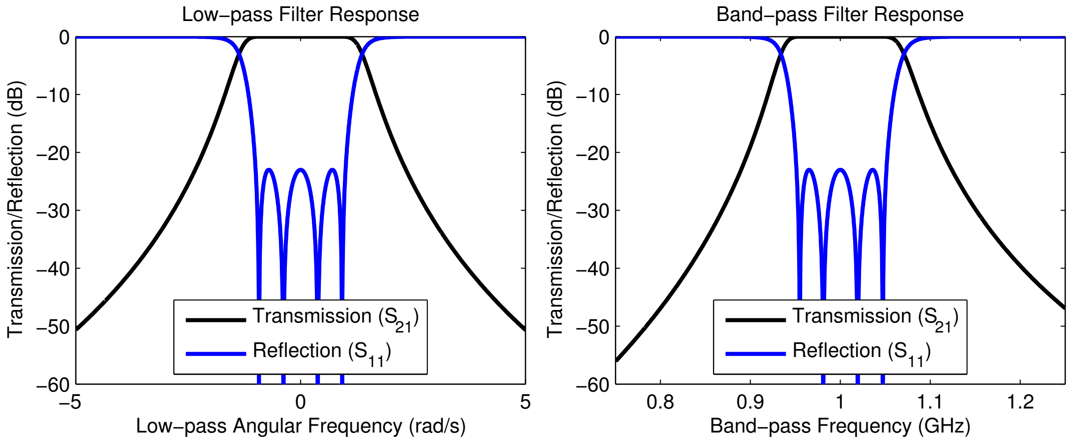

(a) Low-pass (b) Band-pass

Figure 2.24: Low-pass and bandpass responses of the fourth order coupling matrix given in (2.4)

matrix canonical forms from [92] have been combined into a MATLAB graphical user interface (GUI) tool called the Centre for Integrated RF Engineering (CIRFE) Filter Tool. The CIRFE Filter Tool was created to explore tuning algorithms by permitting the direct manipulation of coupling matrix elements using a simple graphical user interface.

The coupled resonator tunable filters presented in this work are all of the equal-ripple Chebyshev type. These filters have the characteristic of being implemented as an in-line chain of coupled synchronous resonators with no cross couplings. A synchronous response implies that the resonators are all tuned to the same unloaded resonance frequency. The presence of no cross-couplings implies that the only non-zero coupling matrix values are $M_{i,i+1} = M_{i+1,i}$ for $i = 1$ to N. In addition, operating in a constant reference impedance environment, such as $50\,\Omega$, results in the network being symmetric across the mid-plane between input and output. As a consequence, the coupling matrix for an in-line Chebyshev filter is also symmetric across the antidiagonal.

Elementary bandpass filter designs of equal-ripple Chebyshev or maximally-flat Butterworth response often begin with g-values. The g-values are low-pass element values that can be transformed to result in a bandpass, bandstop, low-pass or high-pass response as required [95]. The equivalence between the coupling matrix and g-values is given in (2.7) below. Indeed, the polynomial synthesis procedure for generalized Chebyshev functions with transmission zeros is not necessary if the g-values are known.

$$R_1 = \frac{1}{g_0\, g_1} \quad R_N = \frac{1}{g_N\, g_{N+1}} \quad M_{ij} = \frac{1}{\sqrt{g_i\, g_j}} \tag{2.7}$$

Chapter 3

Tunable Filter Design for Constant Bandwidth

Early work on tunable filters focused predominantly on maximizing the tuning range and quality factor. Recently, the focus has shifted to controlling the filter response as it is tuned. A widely used design approach for tunable filters begins with the design of a fixed filter at a nominal center frequency. The fixed filter design is then augmented with a tunable resonator and optimized to achieve the desired tuning range. A common result of the traditional design approach is a filter that maintains constant fractional bandwidth as it is tuned with substantial degradation in return loss as the filter is tuned away from the nominal center frequency. Constant fractional bandwidth filters have a variable absolute bandwidth that is proportional to the center frequency. Front-end filters that maintain a constant absolute bandwidth are of particular interest in software defined radios since baseband circuitry tends to be tailored for a fixed bandwidth.

This chapter presents both a novel constant bandwidth coupling approach for moderate to wideband filters and a coupling matrix based design technique for constant bandwidth tunable filters. The design approach takes a general, resonator technology agnostic approach. The approach is based around coupling matrix synthesis [92]. Although a suspended substrate stripline implementation is used here, the same analysis and synthesis procedure could be applied to designs using a variety of technologies. The design method is not limited to planar circuits since coupling matrix synthesis techniques apply equally well to 3D cavity filters and dielectric resonator filters as shown in [92]. The coupling matrix formulation is chosen to ease extension of the presented technique to higher order filters. Second and third order prototypes are presented in both MEMS and varactor-tuned incarnations.

A coupled resonator filter design that maintains a particular response as the center frequency of the resonators is tuned requires that the input and inter-resonator couplings are kept at a prescribed value across the center frequency tuning range. The constant bandwidth design techniques employed in [46, 50] each focus on a particular transmission line technology. The work presented in [50] makes use of the dispersive nature of corrugated microstrip transmission lines, while [46] employs quarter-wave stripline resonators with a prescribed phase length in the middle of the tuning range. The approach presented in [28] uses a coupling scheme that is difficult to extend to higher order filters due to the use of broadside coupled resonators. The constant bandwidth tunable filter design technique described in [49] makes use of lumped inductors for input coupling, stepped impedance resonators in microstrip technology and utilizes even and odd mode coupled line analysis. The coupling implementations demonstrated in [50] and [49] are well suited for narrowband filters while the coupling implementation presented here is better suited for use in higher frequency and wider bandwidth filters due to the use of tapped interresonator coupling and absence of lumped element components. A comprehensive comparison table of constant bandwidth planar tunable filter designs is shown in Table 2.1 in the literature review chapter.

In addition to the novel coupling structure and comprehensive coupling matrix-based design technique, the third order filter design presented here also implements a novel compensation of the capacitance versus center frequency tuning curve for the center resonator. The compensation is necessary in order for a given capacitance to equate to the same resonance frequency for all resonators despite differences in resonator loading due to the circuit layout. A filter whose resonators have the same resonance frequency for a given capacitance loading is referred to as a filter with synchronous capacitance tuning. Synchronous capacitance tuning is particularly important in switch-tuned filters where the same switched capacitance network is used to tune all of the resonators. The coarse stepping of a switched capacitor network makes fine trimming of the resonance frequency impractical. The work presented in [32] is tuned by a 5-bit MEMS capacitor bank but makes no correction for the modified tuning behavior of the center resonator and results in poor and non-equal-ripple return loss in most states. In this work we demonstrate a simple layout modification that can substantially improve the response of higher order filters under a synchronous capacitance tuning condition.

In order to confirm the validity of the proposed coupling matrix based design approach for tunable filters, a modeling technique is presented. In the presented coupling matrix model, the coupling matrix parameters obtained through sub-circuit optimization are used to synthesize a model that is shown to be capable of accurately predicting the final circuit response in the vicinity of the passband. The validity of the coupling matrix based design approach is verified by equating the model-predicted response with the simulated complete filter.

3.1 Theory

The coupling matrix has traditionally been used in the synthesis of fixed filters and is adopted here for tunable filter design. As discussed in Section 2.3 the coupling matrix does not depend on the center frequency or bandwidth since it is expressed in terms of the low-pass prototype. Therefore, for a filter to maintain the same shape as it is tuned, it should have an identical coupling matrix at all center frequencies, i.e. $\boldsymbol{R}$ and $\boldsymbol{M}$ should remain constant as a function of center frequency. The frequency invariant reactances, B_i, of the coupling matrix can be used to represent the effects of center frequency offset or tuning.

3.1.1 Parameter Specification

The coupling matrix is specified in the low-pass domain. In order for the filter design to maintain a constant bandwidth and return loss, the coupling matrix must remain constant as the center frequency of the filter is tuned. The design constraints for the input coupling and inter-resonator coupling are thus specified on the basis of maintaining a constant coupling matrix and bandpass transformation as the center frequency is tuned.

Input Coupling

The input coupling can be extracted from a single resonant circuit simulation by using the reflected group delay method. The reflected group delay at the resonant frequency of the resonator can be related to the R parameter of the coupling matrix by the expression

$$\tau(f_0) = \frac{4}{R \cdot 2\pi \Delta f} \tag{3.1}$$

where τ represents the reflected group delay or the group delay of S_{11} [92]. R is a parameter of the coupling matrix, Δf is the bandpass bandwidth and f_0 is the resonance frequency (frequency of the group delay peak). Therefore, for a constant bandwidth filter design, the reflected group delay of a single resonant circuit should remain constant over the tuning range of the input resonator.

Inter-resonator Coupling

The inter-resonator coupling can be extracted from a loosely coupled double resonant circuit [93]. A double resonant coupled circuit will show two resonant peaks in the transmission response, denoted f_1 and f_2. The coupling coefficient, k, can be expressed in terms of the two resonant peaks as

$$k = \frac{f_2^2 - f_1^2}{f_2^2 + f_1^2}. \tag{3.2}$$

In the narrowband case, where $f_1 \cdot f_2 \approx f_0^2$, k approximates to

$$k \approx \frac{f_2 - f_1}{f_0} = \frac{\Delta f_{12}}{f_0} \tag{3.3}$$

where $\Delta f_{12} = |f_2 - f_1|$.

The coupling coefficient relates to the low-pass normalized coupling matrix value M through

$$M = \frac{f_0}{\Delta f} k \tag{3.4}$$

and by substituting (3.3) into (3.4) it is determined that the coupling bandwidth ($\Delta f_{12} = M \cdot \Delta f$) should remain constant as the filter is tuned [47].

Therefore, from the target low-pass coupling matrix that prescribes the filter order and return loss level, and the frequency transformation that sets the bandwidth and center frequency, we can specify the target reflected peak group delay ($\tau(f_0)$) and interresonator coupling bandwidths (Δf) for adjacent resonators at each tuned center frequency (f_0).

Center Frequency Tuning

The diagonal elements of a coupling matrix for an in-line Chebyshev filter are all zero, i.e. $M_{ii} = B_i = 0$ for all i. Therefore, all the resonators should have no frequency offset from the bandpass center frequency or, in other words, the resonators should all have the same resonance frequency. Second order filters have this property due to symmetry. Varactor tuned filters with a continuous tuning range can be finely tuned to satisfy this property at the expense of a reduced tuning range where an equiripple response is attainable. However, filters that are tuned using switched elements, such as MEMS, require that the tuning curves for all resonators be matched in order to maintain an equiripple response in all states. It may simply be impractical to include a sufficient number of tuning bits to adjust for the difference in the capacitance versus frequency characteristics without explicit correction at design time. The concept is illustrated in the third order MEMS-tuned filter example that follows with the use of an inductive compensating element.

An accurate simulation of center frequency versus capacitance needs to include the loading effects of the adjacent structures [92]. The adjacent structures should not resonate. A good approximation of the loaded resonance frequency can be simulated by including the next-nearest resonators in the simulation but shorting their tuning elements to ensure that they do not resonate near the band of interest. The center frequency tuning simulation with adjacent resonator loading cannot be performed until the inter-resonator coupling structure is determined. Therefore, some degree of iteration at this stage may be necessary.

3.1.2 Model Extraction

In order to extract the coupling matrix from a completed filter, we may work backwards from the extracted group delay and coupling bandwidths to obtain the coupling matrix of the synthesized network. However, if we start with only the input group delay and each of the inter-resonator coupling coefficients we will be at a loss to set both the coupling matrix values and the bandpass transformation parameters. The equations defining the model are shown in (3.5) where, for a given capacitance C and measured values $\tau(C)$, $k(C)$ and $f(C)$ we seek to find $\Delta f(C)$, $R(C)$, $M_{ij}(C)$ and $B_{ii}(C)$.

$$R(C) = \frac{4}{\tau(C) \cdot 2\pi\Delta f(C)} \qquad M_{ij}(C) = \frac{f_0(C)}{\Delta f(C)} k(C) \tag{3.5}$$

There are more unknowns than equations. Therefore, we need to normalize the coupling matrix. As is customary, the input resistance is normalized to $1\,\Omega$ and the nominal center frequency is selected to be the resonance frequency of the first resonator. As a result, the extracted coupling matrix will have $R_1 = R_N = 1$ and $M_{11} = M_{NN} = B_1 = B_N = 0$. The input coupling simulation sets the bandpass transformation parameters Δf and f_0 based on the reflected group delay of the input reflection coefficient. The inter-resonator couplings $M_{ij}(C)$ directly follow from the expression given for the interresonator coupling where the bandpass transformation parameters Δf and f_0 are set in the preceding input group delay simulation.

Filters of second order are adequately modeled with just the input coupling and inter-resonator coupling simulations. A given load capacitance will, by symmetry alone, result in the same resonance frequency for both resonators. However, higher order filters, such as the third order design described below, may result in a finite offset in the resonance frequency of the asymmetric resonators. The offset can be modeled by setting the diagonal elements, B_i, where $i \neq 0, N$, according to the frequency offset relative to the input and output resonators. The low-pass normalized offset can be calculated from the bandpass transformation as given by

$$B_i = \frac{f_0}{\Delta f} \left(\frac{f_i}{f_0} - \frac{f_0}{f_i} \right). \tag{3.6}$$

In (3.6) Δf is the effective bandpass transformation bandwidth, f_i is the resonant frequency of the off-input resonator and f_0 is the resonance frequency of the input and output resonators. The parameters Δf and f_0 were calculated from the input coupling simulation.

The unity input resistance coupling matrix and bandpass transformation for a synchronously tuned Chebyshev filter is now complete. The S-parameters resulting from the extracted coupling matrix should match the final simulation of the complete filter as a validation of the proposed design method and tunable filter model.

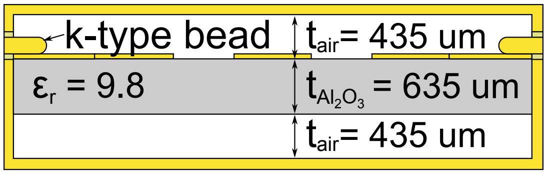

Figure 3.1: Suspended substrate stripline cross-section.

Table 3.1: Second order coupling matrix with 20 dB return loss

$$R_1 = R_N = 1.6583 \quad M_{1,2} = M_{2,1} = 1.5$$

3.2 Design and Simulation

The constant bandwidth tunable filter prototypes were fabricated in suspended substrate stripline technology. The suspended substrate stripline technology was chosen for its high quality factor and compatibility with the UW MEMS manufacturing process. The cross-section of the suspended substrate circuit is shown in Fig. 3.1. The cross-sectional dimensions were chosen such that a 50 Ω line width was 850 μm and the air gap above and below the substrate was equal. A standard UW MEMS multi-project die size of 1 cm by 1 cm was used for both the second and third order filter prototypes.

Quarter-wave resonators were chosen for their spurious-free range and miniature size. The resonators are tuned using a variable capacitive load at the open end of each of the resonators. Notable structures of the filter design are the meandered inter-resonator and input coupling, and the compensation for synchronous capacitance tuning. A novel coupling structure consisting of a meandered line tapped near the open end of the inter-resonator coupled resonators is introduced for constant coupling bandwidth. In the third order filter design synchronous capacitance tuning is achieved by means of an inductive inverted T structure at the top of the middle resonator.

All simulation results were obtained using Sonnet Software's planar circuit simulator *em* [96]. Coupling matrix values for second and third order filters with 20 dB return loss were used and are listed in Tables 3.1 and 3.2. Co-calibrated internal ports of feed-line width were used to simulate the tuning elements. The tuning reactances were cascaded in a circuit simulator to simulate the capacitive loading of the actual tuning elements.

Table 3.2: Third order coupling matrix with 20 dB return loss

$$R_1 = R_3 = 1.1717 \quad M_{1,2} = M_{2,1} = M_{2,3} = M_{3,2} = 1.0303$$

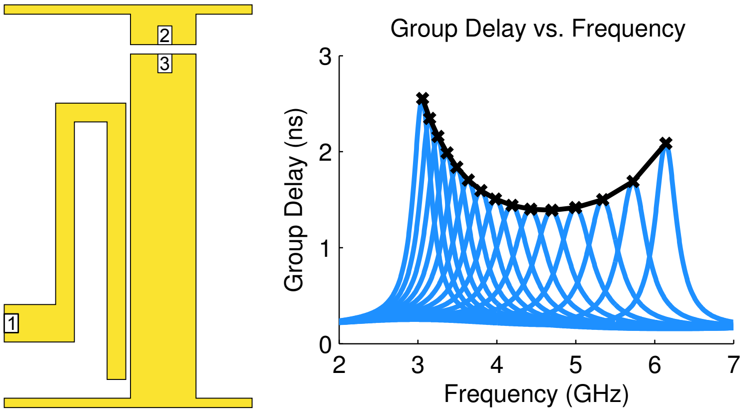

(a) Input coupling simulation (b) Reflected group delay versus frequency

Figure 3.2: Input coupling simulation setup and result.

3.2.1 Input Coupling

The input coupling for constant bandwidth is implemented using a meandered open-ended non-resonating length of transmission line. The open end of the meandered input coupling is near the ground of the first resonator. Lumped element components were avoided in order to implement the circuit as a monolithic MEMS die. In a future work, a tuning element at the open end of the meandered input coupling line may be introduced for input coupling tuning.

The setup of the input coupling simulation is shown in Fig. 3.2a. The extraction of the input coupling parameters proceeds as follows. A three-port simulation is run with the tuning element represented by internal ports two and three. Matlab is used to cascade the S-parameters of a range of capacitance values at the two tuning ports. The reflected group delay is then extracted and the magnitude and frequency of the peak is noted as shown in Fig. 3.2b. The meandered input coupling structure is compared to the traditional tapped and edge coupled structures in Fig. 3.3. As shown in Fig. 3.3, the meandered coupling structure outperforms the tapped and edge coupled designs with regard to peak group delay variation with center frequency. The meandered input coupling results in a parabolic shape of the peak reflected group delay with respect to

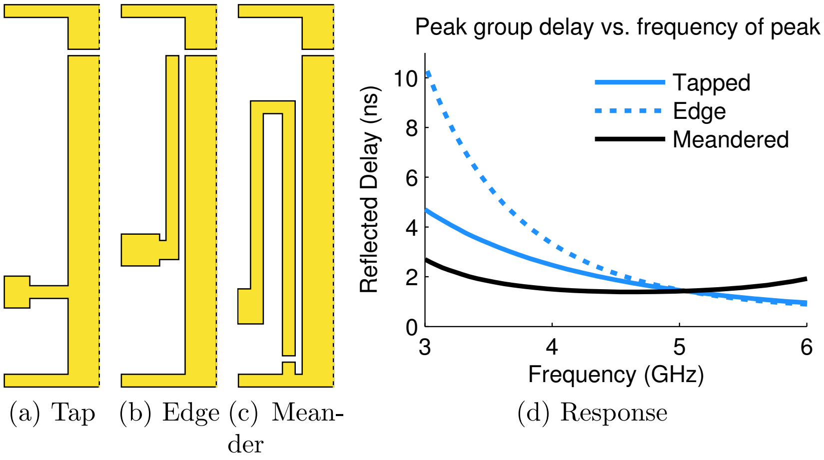

(a) Tap (b) Edge (c) Meander (d) Response

Figure 3.3: Three input coupling structures compared.

input resonator resonance frequency and is a better candidate for a constant bandwidth filter design than tapped and edge coupled approaches.

3.2.2 Inter-resonator Coupling

The inter-resonator coupling structure is shown in Fig. 3.4a. A hybrid inter-resonator coupling structure is realized using a combline topology that is enhanced with a narrow high impedance meandered line that acts as an additional inductive element in order to increase coupling at lower frequencies. The inter-resonator couplings are determined from the frequency spacings of the resonant peaks using (3.3) as shown in Fig. 3.4b at each load capacitance.

The inter-resonator coupling of the combline structure with meandered line is compared to the traditional combline and interdigitated structures in Fig. 3.5. The meandered coupling structure provides a substantially better coupling variation with center frequency than either the combline or interdigitated structures.

In Chebyshev filters of second and third order there are only two couplings to design: the input coupling and the inter-resonator coupling (symmetric in the case of the third order). The return loss variation over the tuning range is determined by the relationship between the input coupling and inter-resonator coupling as the center frequency is tuned. The input coupling variation with center frequency can be used to impose the

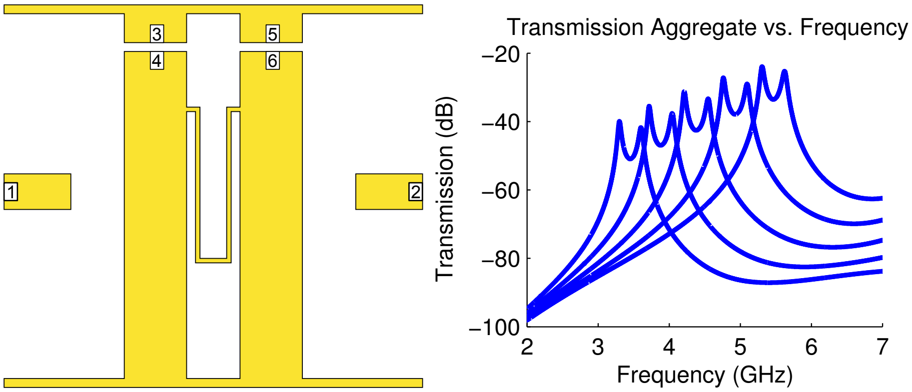

(a) Inter-resonator coupling simulation

(b) Transmission at multiple loadings

Figure 3.4: Simulated structure and transmission of coupling simulation for several capacitive loadings. The spacing between the resonant peaks at a given loading are indicative of the coupling between the resonators.

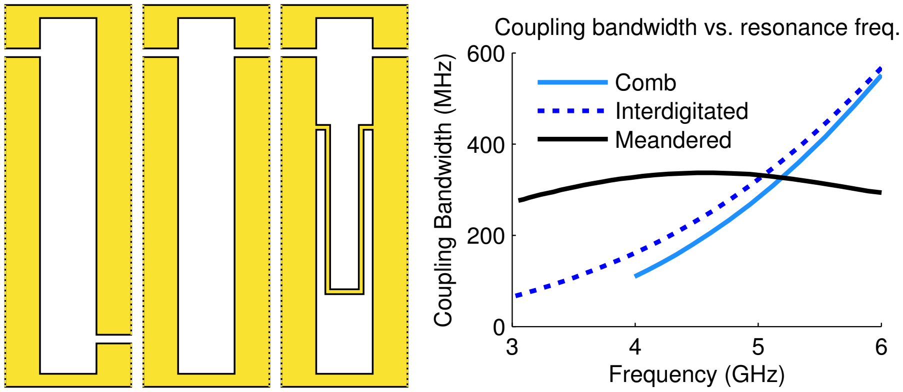

(a) Interdigitated

(b) Combline

(c) Meandered

(d) Coupling bandwidth comparison

Figure 3.5: Three interresonator coupling structures compared.

requirements on the inter-resonator coupling to meet the return loss specification.

All simulations are performed with the tuning load capacitance (C) as a parameter. The coupling matrix parameters are derived as a function of capacitance from the simulated $\tau_{f0}(C)$ and $k_(C)$. The input coupling bandwidth as a function of load capacitance ($\Delta f(C)$) for a particular return loss is calculated by rearranging (3.1) to solve for $\Delta f(C)$ using a normalized resistance R. The input coupling bandwidth is substituted into (3.4) to determine the required coupling coefficient for a minimum return loss as given in (3.7).

$$\Delta f(C) = \frac{4}{R \cdot \tau_{f_0}(C)} \qquad\qquad k_{20dB}(C) \leq \frac{M_{20dB} \cdot \Delta f(C)}{f_0(C)} \tag{3.7}$$

Fig. 3.6 shows the simulated inter-resonator coupling for the meandered coupling structure and the 20 dB return loss coupling curve calculated from the meandered input coupling simulation result shown in Fig. 3.3d. Maintaining an inter-resonator coupling below the 20 dB return loss coupling curve will result in a return loss higher than 20 dB. An additional benefit of lower inter-resonator coupling in the middle of the tuning range is the reduction of the filter bandwidth and overall bandwidth variation since the input coupling peaks in the middle of the tuning range.

The inter-resonator coupling result shown in Fig. 3.6 is generated using a peak-finding algorithm to find the frequency of the two resonant peaks of the transmission coefficient. The two resonant peaks are used to calculate $k_{1,2}$ using (3.4). The inter-resonator coupling is optimized such that the simulated coupling variation satisfies the 20 dB return loss coupling at the extremes of the tuning range as shown in Fig. 3.6.

3.2.3 Synchronous Capacitance Tuning

At this point, with the input coupling and inter-resonator coupling initially specified, a first-order prototype design is complete. A single pass design is sufficient for second order filters where the two resonators resonate at the same frequency due to symmetry. The resonant frequency versus load capacitance in higher order filters, however, is not the same on an asymmetric pair of resonators since their loadings are not identical. In the case of a third order filter, for example, resonators one and three experience the same loading due to symmetry; the load of one input coupling and the load of one inter-resonator coupling. The middle resonator, resonator two, only experiences two inter-resonator loadings and

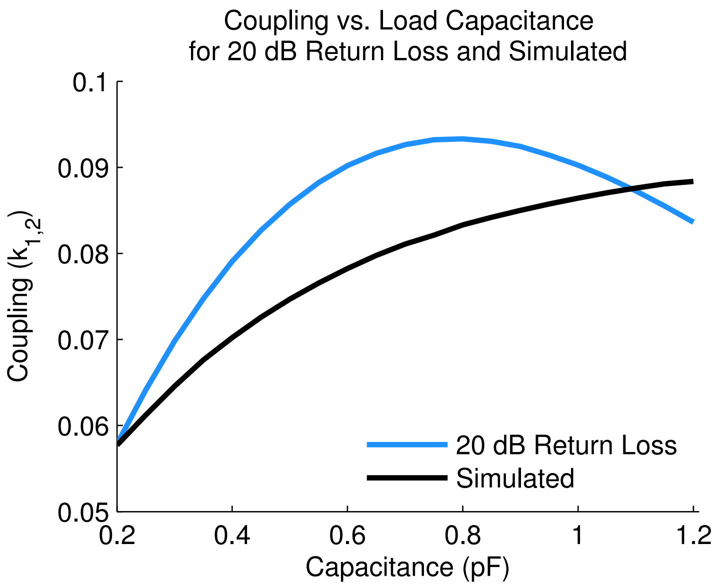

Figure 3.6: Plot of desired versus simulated inter resonator coupling for a three-pole filter with 20 dB return loss. The inter-resonator coupling is optimized such that the coupling coefficients match the desired curves at the extents of the tuning range.

is likely to have a very different tuning characteristic than resonators one and three. The net effect is that resonators one and three will tune to two different resonance frequencies than resonator two for a given load capacitance value.

Traditional tuning using varactor diodes is only moderately affected by asynchronous loading of the resonators since the continuous tuning nature of varactors permits each resonator to be trimmed to the same frequency as was done in [49]. As a consequence, each diode would necessitate a different tuning voltage and require a separate bias to be supplied. RF-MEMS tuning elements, however, are primarily implemented as switched capacitor banks. The coarse capacitance tuning of a switched capacitor implementation requires that all of the resonators tune to the same resonance frequency for a given capacitance value. A filter that is tuned with an identical capacitance on each resonator is referred to as a filter with synchronous capacitance tuning.

An initial design with optimized coupling for a flat coupling variation at midband for the third order filter is shown in Fig. 3.7a. The filter response of the initial design with synchronous capacitance tuning is shown in Fig. 3.7b and results in a poor return loss over most of the tuning range. Compensation of asymmetric resonator loading is required. In

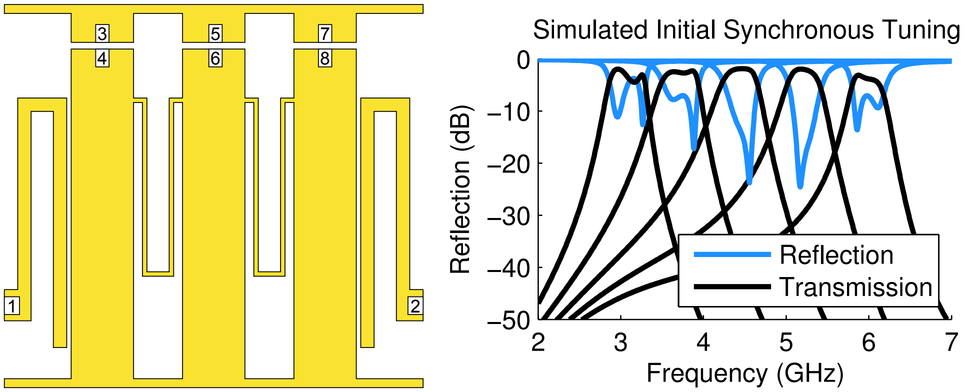

(a) Initial schematic of 3rd order filter (b) Initial synchronous capacitance tuning

Figure 3.7: Initial design and response of filter with synchronous capacitance tuning. Tuning states shown for load capacitances of 1.5 pF, 0.95 pF, 0.57 pF, 0.3 pF and 0.1 pF

this work we propose an approach to match the center frequency vs. capacitance tuning curve of each resonator by employing a semi-lumped inductance.

The loaded center frequency versus capacitance characteristic for a tunable resonator is simulated by shorting out the adjacent resonators and leaving the coupling structures intact. Schematic depictions of the simulated initial and optimized structures for the middle resonator of the third order filter are shown in Fig. 3.8a and Fig. 3.8b, respectively. The resonance frequency is extracted by finding the peak of the transmission coefficient and recording the frequency at which the peak occurs with respect to load capacitance.

The length of the resonator and the length and width of the semi lumped inductance provide three degrees of freedom to optimize the frequency versus capacitance tuning curve. The semi lumped inductance is implemented as an inverted T at the ground connection of the tuning element as shown in Fig. 3.8b. The semi-lumped inductance adjusts the tuning rate or slope of the resonance frequency versus capacitance curve while adjusting the length of the resonator shifts the nominal resonance frequency. The resonance frequency vs. tuning capacitance of the initial and optimized middle resonator designs relative to the input and output resonators are shown in Fig. 3.9a. Fig. 3.9b shows that the optimized design has a smaller frequency deviation from the i/o resonators. The worst case frequency deviation of the optimized design is less than 50 MHz while the initial design has an error of up to 300 MHz.

A schematic representation of the third order design using the proposed technique is

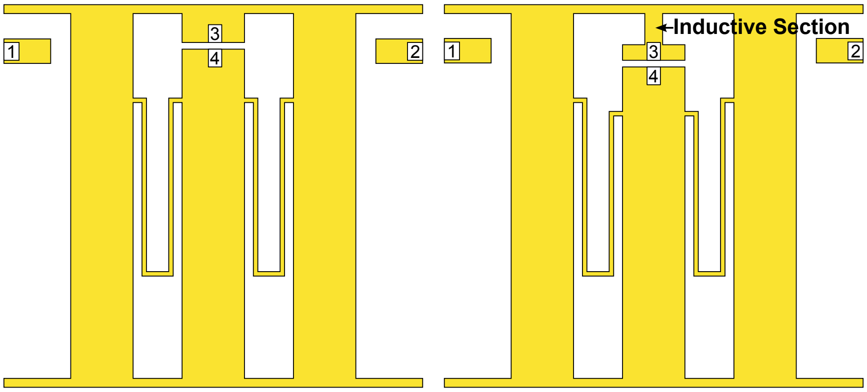

(a) Initial central resonator (b) Optimized central resonator

Figure 3.8: The initial and optimized designs for the central resonator with center frequency tuning compensation.

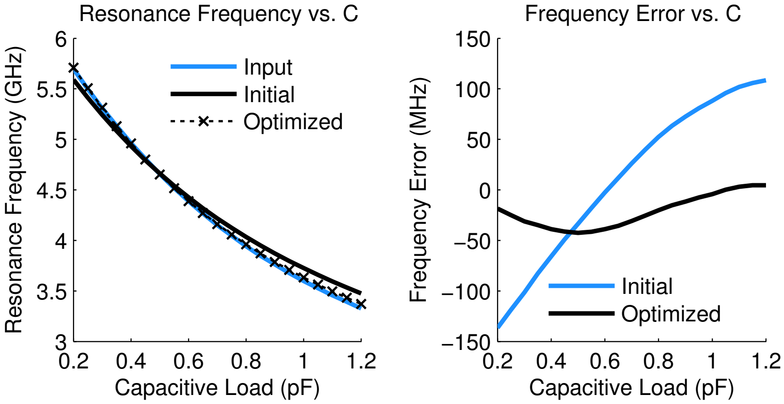

(a) Tuning comparison of initial and optimized designs (b) Tuning error wrt i/o resonators

Figure 3.9: Simulated loaded resonance frequency with respect to tuning capacitance for the input resonator and the initial and optimized central resonator designs.

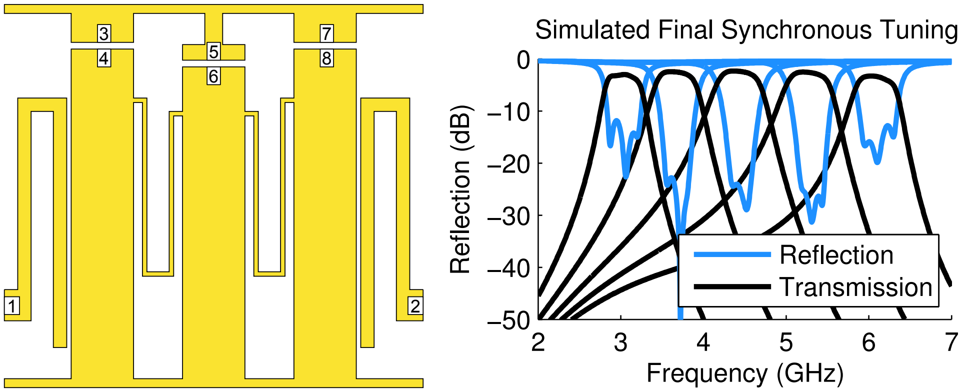

(a) Final schematic of filter (b) Optimized synchronous capacitance tuning

Figure 3.10: Layout of the 3rd order filter designed using the proposed coupling technique. Dimensions are constrained to fit inside the same housing as the second order filter.

shown in Fig. 3.10. The simulated results for the third order tunable filter implemented using the proposed coupling and design techniques is shown in Fig. 3.10b. The simulated tuning range is from 3.26 GHz to 5.41 GHz with better than 20 dB return loss or 4.34 GHz±25% with a 3 dB bandwidth of 517 MHz±8%.

The conductivity of the simulated metal was adjusted to fit measurement results. The Q was then extracted from the simulation results. The simulated Q with 1 μm thick metalization and conductivity of 2.09e7 S/m ranges from 70 to 43 at center frequencies from 6 GHz to 3 GHz, respectively. Increasing the metalization thickness to 8 μm would increase the Q to 100 over the entire tuning range.

3.2.4 Coupling Matrix Model Extraction and Design Verification

The design of filters with constant bandwidth using design constraints derived from the coupling matrix model has been described thus far. The same process can also be reversed, whereby the completed design is used as the starting point and the coupling matrix model is extracted from a simulation of the complete filter. The tunable coupling matrix model can then be used in tuning algorithms, for example, or in this case as validation of the design approach.

The coupling matrix model extraction proceeds using the same approach as the filter

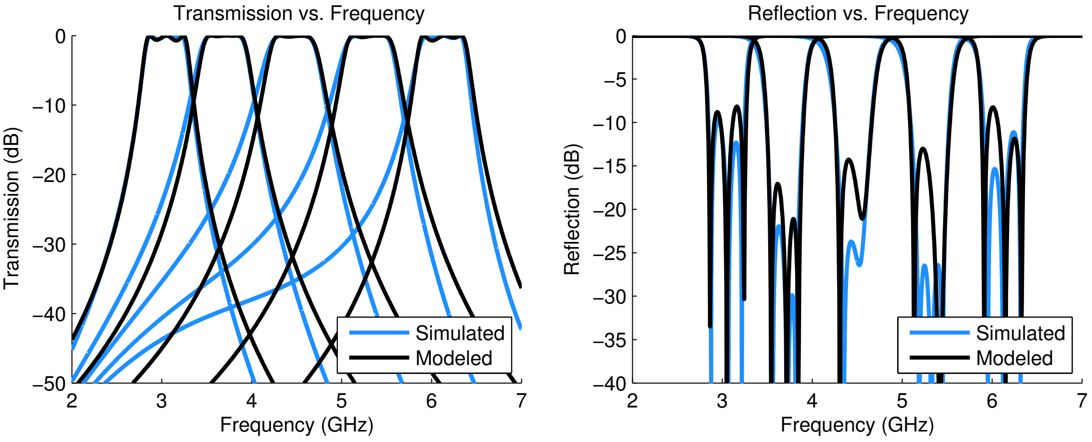

(a) Transmission comparison (b) Reflection comparison

Figure 3.11: Comparison of simulated and coupling matrix model derived responses. The close match validates the design approach.

design. The model extraction procedures was described in Section 3.1.2.

The semi-lumped meandered coupling structure results in a frequency variant coupling that violates the frequency invariant coupling model of the coupling matrix. Since the filter is of a relatively wide bandwidth the frequency variant coupling should also be included. A comparison of the transmission and reflection magnitude parameters of the complete filter and the coupling matrix model for the third order filter are shown in Fig. 3.11. The close match of the simulated and measured responses in the vicinity of the pass band validate the design approach. The low-frequency rejection is worse than predicted by the model due to the resonance of the meandered feed line at 3 GHz. The discontinuity is relatively small hence the relatively small effect on the rejection.

3.3 Measurement Results

Measured and simulated results for four filters are presented in this section. Varactor and MEMS tuned prototypes were fabricated for both the 2-pole and 3-pole designs. The 2-pole results are presented first, followed by the results for the 3-pole design.

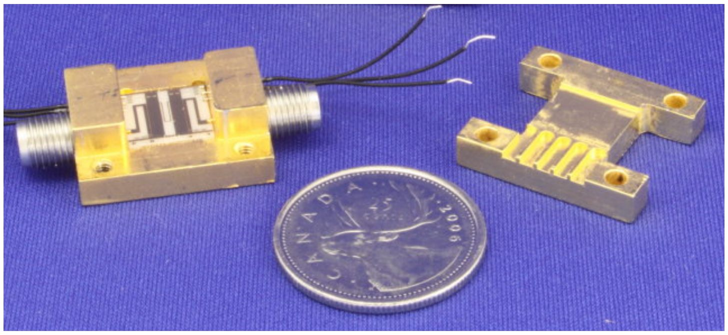

Figure 3.12: Packaged filter with lid removed showing the alumina die with integrated MEMS tuning elements and resistive biasing lines. The biasing leads are also shown.

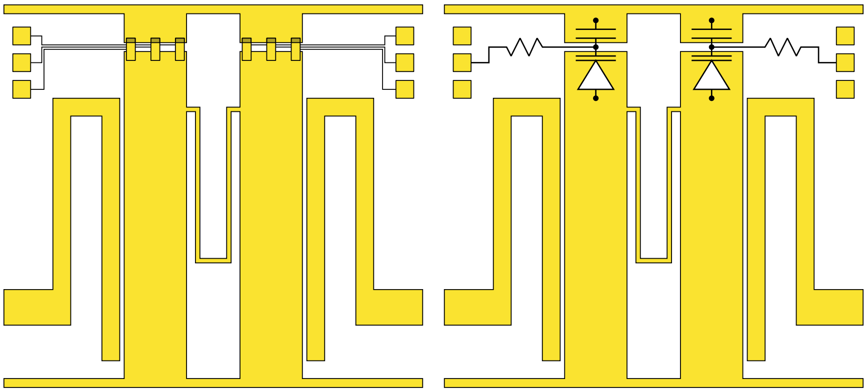

(a) MEMS tuned filter

(b) Varactor tuned filter

Figure 3.13: Schematic diagrams of the MEMS and varactor tuned suspended substrate filter implementations. The MEMS design has three MEMS tuning elements per resonator while the varactor tuned design has a single varactor per resonator.

3.3.1 Two Pole Measurement Results

A photograph of the MEMS-tuned 2-pole suspended substrate filter prototype housed in a gold plated aluminum housing is shown in Fig. 3.12. The prototype alumina die is fabricated in the UW MEMS process described in Appendix A. MEMS variable capacitor and semiconductor varactor tuned designs were fabricated.

The alumina die is mounted inside of a gold plated aluminum housing with K-connectors as shown in Fig. 3.12. DC biasing is provided by feeding wire through small holes in the housing that are subsequently sealed up with epoxy. The DC leads and K-connector beads are spot-welded to the alumina die using gold ribbon.

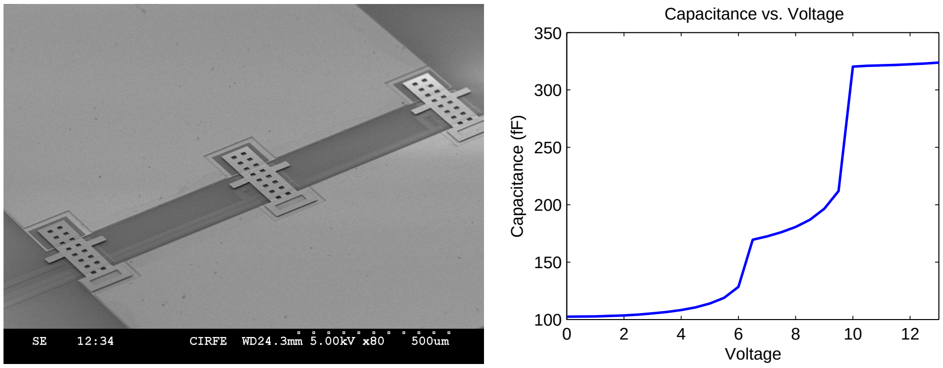

(a) SEM (b) CV

Figure 3.14: SEM of the MEMS devices and the C-V characteristic of a single MEMS varactor.

The variable capacitive loads are realized using both MEMS variable capacitors and varactor diodes as shown in Fig. 3.13. The MEMS variable capacitors are monolithically integrated during the fabrication process. The MEMS capacitors are of a fixed-free cantilever type, identical to those used in [97], and exhibit a hybrid switched and continuous C-V response. An SEM image of three MEMS variable capacitors mounted at the end of one of the resonators is shown in Fig. 3.14a. The C-V response obtained in the initial fabrication of this device from [97] is shown in Fig. 3.14b.

The tuning element capacitances are extracted from simulation for the MEMS-based design. Due to the residual stress in the final fabrication run the tuning range was only 115 fF total with 3 tuning elements on each resonator while 3 × 220 fF was expected based on the C-V curve of the preliminary run shown in Fig. 3.14b. The MEMS-based tuning range was less than $^1/_5$ of the anticipated value. The measured results with MEMS tuning elements closely match the simulated results for ideal capacitors as shown in Fig. 3.15. The insertion loss decreases with reduced frequency when the filter is tuned with the MEMS tuning elements as expected from the simulated results. The MEMS implementation tunes from 5.91 GHz to 5.43 GHz and the bandwidth varies from 546 MHz to 589.2 MHz for a voltage bias from 0 V to 150 V.

In order to validate the broadband tuning capability of the design, a varactor-tuned implementation is also demonstrated. The MA46H120 Series Hyper-abrupt GaAs varactor diodes from M/A-COM are biased using 47 kΩ 0201 resistors and 5.6 pF MIS capacitors from Skyworks as shown in Fig. 3.13b. The varactors and MIS capacitors are bonded

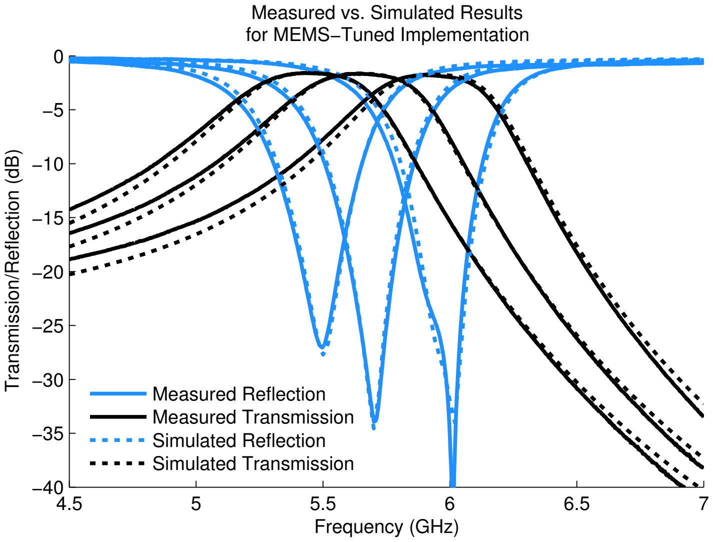

Figure 3.15: Simulated versus measured response of the MEMS-tuned version of the two-pole tunable filter. Bandwidths: 546 MHz at 5.91 GHz, 572 MHz at 5.64 GHz and 590 MHz at 5.43 GHz.

onto the suspended substrate die using silver epoxy, and the resistors are mounted using 5 minute epoxy. Interconnections are made using gold wire bonds. The center frequency of the varactor implementation varies from 3.69 GHz to 5.46 GHz and the bandwidth varies from 503.4 MHz to 588.6 MHz with a voltage bias from 2 V to 12 V, respectively. The measured and simulated results of the varactor tuned filter are shown in Fig. 3.16 where the varactor is modeled as a series RLC circuit with fixed inductance and a variable resistance and capacitance. Combining the results of the MEMS and varactor implementations yields an aggregate bandwidth of 546.4 MHz±7.8 % over a tuning range of 4.79 GHz±23 % for the implemented filter design.

3.3.2 Three-Pole Filter Measurement Results

Two implementations of the three pole filter were also fabricated. One implementation is tuned using MGV100-20 GaAs hyperabrupt varactor diodes from Aeroflex and the other uses monolithically integrated MEMS devices. Both implementations use identical circuit layouts. The varactors were mounted with silver epoxy and decoupled using 10 pF MIS single layer capacitors from Skyworks. Wire bonding was used to connect the anode to the biasing network and the varactors were tuned using a negative bias voltage. Biasing

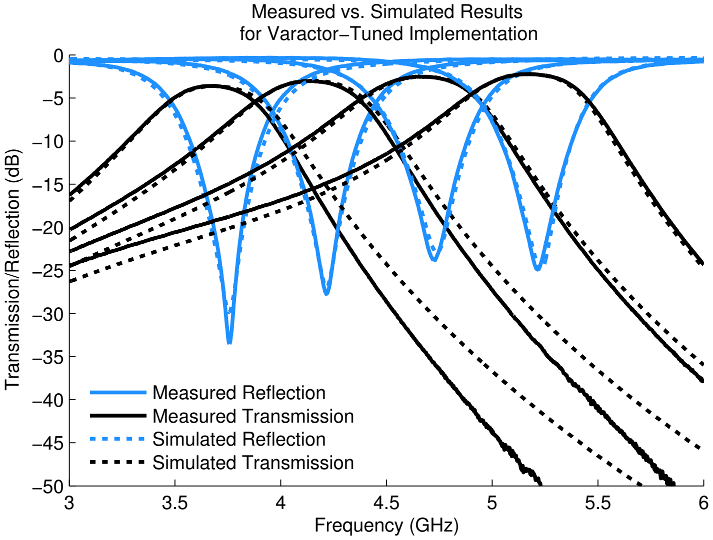

Figure 3.16: Measured and simulated response of the varactor tuned version of the two-pole tunable filter. Bandwidth: 589 MHz at 5.16 GHz, 586 MHz at 4.65 GHz, 558 MHz at 4.13 GHz and 503 MHz at 3.67 GHz

Table 3.3: Second order filter tuning summary

f_0	3dB Bandwidth	Insertion Loss
5.91 GHz	546 MHz	1.78 *
5.64 GHz	572 MHz	1.66 *
5.43 GHz	590 MHz	1.58 *
5.16 GHz	589 MHz	2.22
4.65 GHz	586 MHz	2.51
4.13 GHz	558 MHz	3.02
3.67 GHz	503 MHz	3.59
* indicates MEMS tuned		

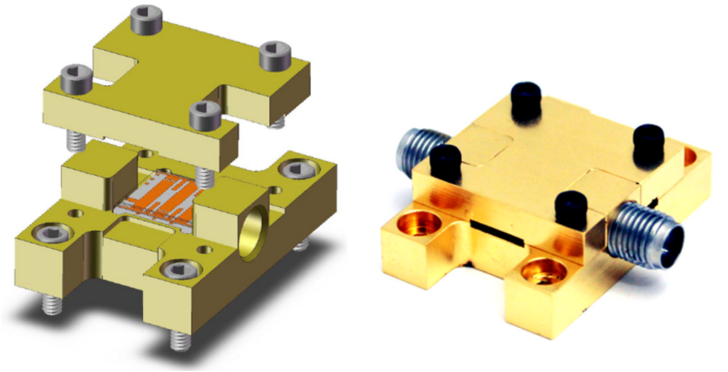

(a) Exploded CAD view (b) Photograph of housed filter

Figure 3.17: Exploded CAD view and photograph of assembled gold plated housing.

of both the varactor and MEMS devices was done using resistors; chip resistors in the varactor tuned case and integrated chromium biasing lines in the MEMS tuned case. The suspended substrate filter die were mounted inside of a gold plated aluminum housing with 5 minute epoxy. Spark plug style K-Connectors were used as filter terminations. Biasing voltages were supplied using an off-the-shelf flex jumper cable that was epoxied to the housing. Wire bonds were used between the filter die and the flex cable on the inside of the housing.

An exploded CAD drawing and photograph of an assembled housing are shown in Fig. 3.17. The flex cables are not shown. The flex cables are fed through the slots which are visible next to the K-Connectors. Vias were not available in our fabrication process so ridges in the lid of the housing clamp the die at the top and bottom to provide RF ground terminations. The MEMS die is 1 cm × 1 cm and the total size of the filter including mounting tabs and the K-Connectors is 35 mm × 32.5 mm × 10 mm.

Simulated and measured results for both the MEMS and varactor tuned implementations were obtained. In both cases, the simulated results were obtained from the same *em* simulation. The MEMS devices were treated as ideal capacitors while the varactors were modeled as series RLC circuits. The simulated results included losses associated with the housing and stripline metalization.

The MEMS tuned result is shown in Fig. 3.18 and is contrasted with simulated results that include fitting for the input coupling load capacitance. Only conduction losses of the housing and circuit metalization were included in simulation—i.e. the MEMS devices

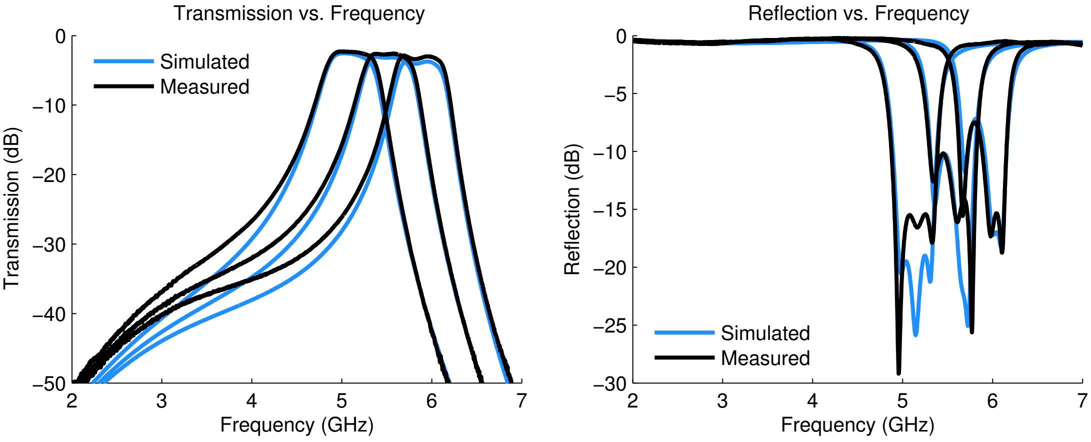

(a) Transmission results

(b) Reflection results

Figure 3.18: Comparison of simulated and measured results for the MEMS tuned implementation. Bandwidths: 577 MHz at 5.87 GHz, 576.5 MHz at 5.52 GHz and 591.5 MHz at 5.1 GHz.

were considered lossless. In this design, the conduction loss of the thin film gold was the dominant loss mechanism and not the quality factor of the MEMS tuning elements.

The MEMS devices implemented did not produce the anticipated tuning range. Therefore, as in the second order filter example, a varactor implementation was also assembled to cover the remainder of the tuning range. The varactor-tuned measured and simulated results are shown in Fig. 3.19. In the varactor tuned case, the loss of the varactor diode is the dominant loss mechanism. The varactor diode in this case is modeled as a series RLC circuit with a fixed bond-wire inductance of 0.15 nH and a capacitance tuning range from 0.4 pF to 1.24 pF. The loss increases with lower bias voltages and higher capacitance values. The resistance was assumed to be proportional to the capacitance with a range from 0.5 Ω to 1.8 Ω. An equal ripple return loss was obtained for all tuning states due to the continuous tuning range of the varactor diode. The simulated results were tuned using asynchronous capacitance tuning with a maximum deviation of 15 fF required to achieve an equal-ripple return loss for the simulated result.

If the losses of the varactor are removed from the simulated result of Fig. 3.19 then we obtain the result shown in Fig. 3.20. The bandwidth variation of Fig. 3.19 is therefore a consequence of poor roll-off due to reduced Q and not due to poorly synthesized coupling values. A wideband MEMS tuned implementation would not suffer such large losses. A

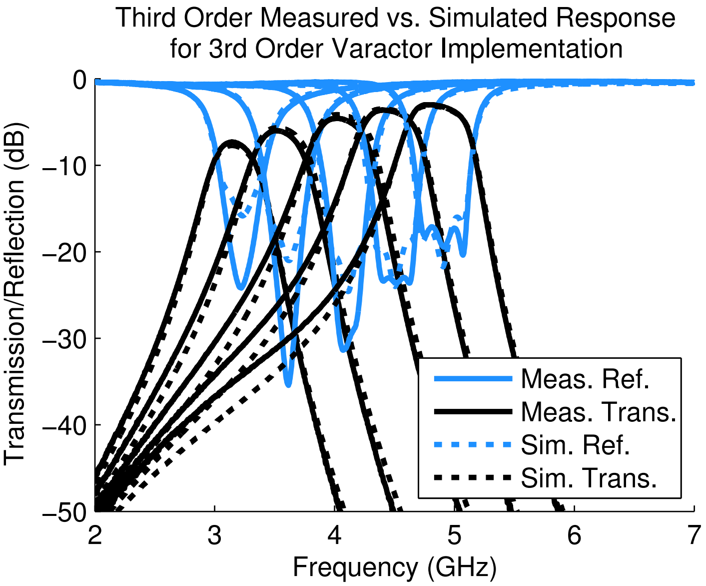

Figure 3.19: Measured and simulated results for varactor tuned implementation. Bandwidths: 523 MHz at 4.85 GHz, 494 MHz at 4.45 GHz, 464 MHz at 4.04 GHz, 422 MHz at 3.53 GHz, 380 MHz at 3.16 GHz.

Table 3.4: Third order filter tuning summary

f_0	3dB Bandwidth	Insertion Loss
5.87 GHz	577 MHz	2.87 *
5.52 GHz	577 MHz	2.64 *
5.10 GHz	592 MHz	2.26 *
4.85 GHz	523 (545) MHz	3.01
4.45 GHz	494 (532) MHz	3.62
4.04 GHz	464 (511) MHz	4.57
3.53 GHz	422 (473) MHz	5.99
3.16 GHz	380 (436) MHz	7.33

* indicates MEMS tuned
() indicate lossless varactor simulation

summary of the performance is shown in Table 3.4.

The aggregate results of the two implementations result in a 3 dB bandwidth variation of 577 MHz to 436 MHz from 5.87 GHz to 3.1 GHz.

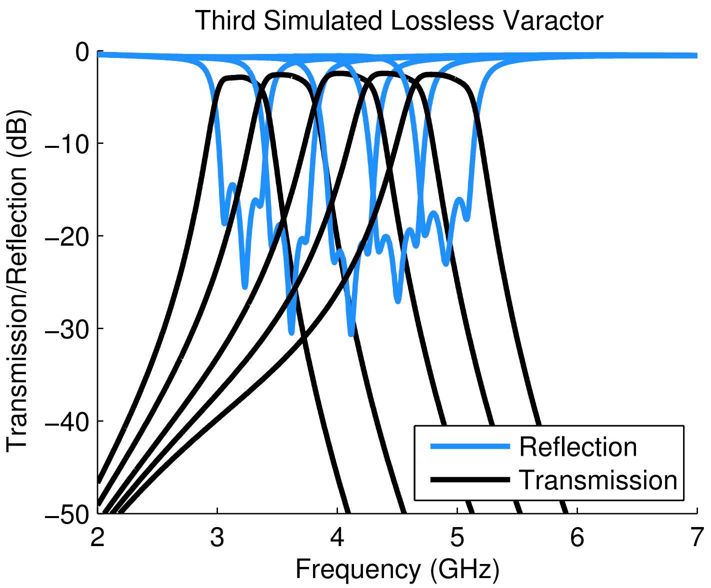

Figure 3.20: Simulated lossless varactor result based on simulation parameters extracted from the simulated result shown in Fig. 3.19. Bandwidths: 545 MHz at 4.86 GHz, 532 MHz at 4.46 GHz, 511 MHz at 4.08 GHz, 473 MHz at 3.58 GHz, 436 MHz at 3.19 GHz.

3.4 Summary

A coupling matrix-based technique for the synthesis of tunable filters with constant absolute bandwidth has been demonstrated. A tapped meandered inter-resonator coupling was used to maintain coupling variation across the tuning range, and an inverted T inductive loading was introduced to the middle resonator for synchronous capacitance tuning. Two filter realizations, one MEMS-tuned and the other varactor-tuned, were presented with measured results. Measured results from MEMS and varactor-tuned prototypes have been presented to validate the proposed concept and verify the simulated results. The modeling and design technique presented is particularly attractive because it is implementation technology agnostic. The same approach can be used to design both cavity and planar filters that exhibit constant bandwidth and a prescribed minimum return loss.

A wideband two-pole tunable filter design that maintains a bandwidth of 568 MHz±3.9% over a tuning range of 5.02 GHz±17.8% has been presented. The constant bandwidth performance is state of the art compared to the constant bandwidth designs presented in Table 2.1. A three pole filter was also fabricated in order to demonstrate the ease of extension to higher order filters. The fabricated three-pole filter exhibited a bandwidth variation of 536 MHz±7.7% over a tuning range of 5.16 GHz±14%. The varactor tuned three-pole filter suffered from substantial loss that limited the useful tuning range.

Chapter 4

Filter Tuning Techniques Based on Scalar Transmission Measurement

Tunable Chebyshev filters are controlled by a number of frequency and/or coupling tuning elements. The tuning elements may be any of a number of tunable components such as tuning screws, semiconductor varactors, MEMS switches, BST varactors, etc. The prescribed purpose of each tuning element is the adjustment of either a resonator's center frequency, the coupling between two adjacent resonators or the input and output coupling. The filter tuning problem is complex due to the high level of interaction between the center frequency of each resonator and the couplings that combine to generate the final filter response.

The cost of commercial microwave filters is highly dependent on the amount of effort and equipment required for post-production tuning. The process generally requires skilled technicians and expensive vector network analyzers. The desire to reduce filter tuning costs has led to the development of sequential tuning techniques for synchronous coupled resonator filters. Group delay [73], time-domain [72] and fuzzy logic [71] techniques have been developed to reduce the complexity of the filter tuning problem. These techniques were all developed for the design and post-production tuning of coupled resonator filters and rely on the phase and/or magnitude quantities of the reflection coefficient. A completely automated system was demonstrated in [81] for the post production tuning of microwave filters using phase and magnitude data measured by a VNA. The parameter extraction based tuning methods described in [98–100] rely on the pole and zero identification of the filter transfer function from the phase data and eventual transcription to the coupling matrix model for tuning and, therefore, also require the use of a VNA for filter measurement. Scalar characterization, as shown in Fig. 4.1b, is a legacy and lower cost option. Using an scalar network analyzer (SNA) results in a less precise measurement since full calibration requires vector data. The use of SNAs has largely been discontinued in production environments where accuracy is paramount.

Integrated tunable filters, however, need to be tuned in-circuit and need to be tuned in a fully-automatic manner with minimal additional hardware. The aim of this work is to eliminate the necessity of the VNA and factor the required functionality to a subset necessary for sequential filter tuning. The proposed scalar transmission magnitude based tuning techniques described in this chapter do not require the use of any directional couplers or quadrature receivers. Scalar transmission based approaches reduce the required tuning hardware and cost as shown in Fig. 4.1 and enable the integration of closed-loop tuning with minimal additional hardware. In addition, the components necessary for tuning can all be found in commercial off-the-shelf transceivers resulting in reduced incremental cost as shown in Fig. 4.1c. Fig. 4.1c shows the basic tuning system required to implement the proposed approaches. The measurement setup consists of a frequency synthesizer, a power detector and a processor. These three elements are already integrated into commercial wireless devices. The techniques presented here are, therefore, highly amenable to monolithic integration.

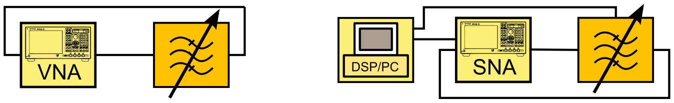

(a) VNA-based (high cost) (b) SNA-based (medium cost)

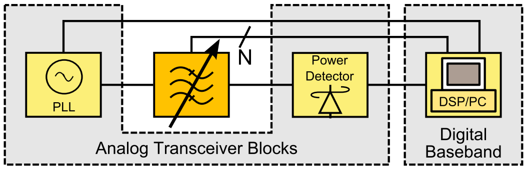

(c) Integrated tuning hardware (low cost)

Figure 4.1: Filter measurement configurations with cost comparison. The VNA (vector network analyzer) configuration is the most expensive followed by the SNA (scalar network analyzer) configuration. The commercial off-the-shelf hardware configuration shown in Fig. 4.1c is highly amenable to integration. The highlighted blocks in Fig. 4.1c are readily available components in commercial transceivers and can be integrated into a monolithic solution.

Two tuning techniques are presented in this Chapter. The technique presented in Section 4.1 uses the Hilbert transform to derive a relative group delay from a scalar transmission response measurement. The tuning procedure is similar to the one described in [73] with the notable difference being the use of a scalar transmission measurement in the work presented in Section 4.1 as opposed to vector reflection measurement as presented in [73]. The second technique in this Chapter is presented in Section 4.2 and uses a single frequency magnitude measurement to achieve the filter tuning objective. The advantages of the scalar transmission based tuning technique are that the scalar based technique requires less computational complexity and results in much faster tuning than the Hilbert transform based technique. However, the scalar tuning technique presented in Section 4.2 has a finite tuning error and does not have a means to tune inter-resonator coupling.

4.1 Hilbert Transform Derived Relative Group Delay Method

The aim of the Hilbert transform derived relative group delay (HGD) technique is to accomplish sequential tuning while only requiring the measurement of the transmission magnitude. This is accomplished by applying the Hilbert transform to the magnitude response of filter transmission to derive the relative group delay. The use of the Hilbert transform technique for relative group delay approximation was demonstrated by Perry and Brazil in [101] for the measurement of passband group delay ripple.

The tuning technique is similar to the one described by Ness in [73] with the noted exception that only the magnitude of S_{21} is measured instead of the group delay of S_{11}. The group delay of S_{21} is derived from the Hilbert transform of the magnitude response. This approach does away with the need for phase detection or the use of directional couplers.

4.1.1 Theory

A common design technique for synchronous bandpass filters is to use the low pass prototype followed by impedance and frequency transformations to arrive at a bandpass model. Inverters are then employed to arrive at a coupled resonator model as described in [102] and shown in Fig. 4.2. Here, we first extend the traditional group delay technique demonstrated by Ness in [73] to S_{21}. We then extend the technique to use a relative measurement as opposed to the absolute value of the group delay at the center frequency. Finally, we show that the Hilbert transform derived group delay can be used instead of the absolute group delay.

Extending Ness's method to S_{21}

As described in [73], the group delay of the bandpass filter can be determined from the low-pass prototype by applying the relationship

$$\Gamma_d = -\frac{\partial \phi'}{\partial \omega'}\frac{\partial \omega'}{\partial \omega}. \tag{4.1}$$

Where ϕ' is the phase response of the low-pass prototype, ω' is the low pass angular frequency variable and ω is the bandpass angular frequency variable. The transformation from ω' to ω is

$$\omega' = \frac{\omega_0}{\omega_2 - \omega_1}\left(\frac{\omega}{\omega_0} - \frac{\omega_0}{\omega}\right). \tag{4.2}$$

Contrary to the method described by Ness, we seek the group delay of the transmission parameter S_{21} when successive resonators are effectively shorted. This poses a dilemma since clearly a filter with a shorted shunt resonator should have no transmission. To circumvent this dilemma and to show that the group delay still exists, we insert a shunt conductance Y_{sc} into the model shown in Fig. 4.2 after the first inductance g_1. The S_{21} is determined by cascading the ABCD parameters of the series inductance g_1 and the shunt conductance of Y_{sc}. S_{21} can then be expressed as (4.3).

$$S'_{21} = \frac{2}{2 + Y_{sc}g_0 + j\omega g_1(1/g_0 + Y_{sc})} \tag{4.3}$$

Next, we find the phase of S_{21} as

$$\phi' = -\tan^{-1}\left(\frac{\omega' g_1(1/g_0 + Y_{sc})}{2 + Y_{sc}g_0}\right) \tag{4.4}$$

and then take the limit

$$\lim_{Y_{sc}\to\infty}\phi' = -\tan^{-1}\left(\frac{\omega' g_1}{g_0}\right). \tag{4.5}$$

The group delay of the low-pass prototype with all but the first reactance shorted is therefore

$$\Gamma_d' = -\frac{\delta\phi'}{\delta\omega'} = \frac{g_1}{1+\omega'^2 {g_1}^2}. \tag{4.6}$$

Applying the frequency transformation to bandpass we get

$$\Gamma_d(\omega) = \Gamma_d' \frac{\partial\omega'}{\partial\omega} = \Gamma_d' \frac{\omega^2+\omega_0^2}{\omega^2(\omega_2-\omega_1)}. \tag{4.7}$$

From (4.2) at $\omega = \omega_0$, $\omega' = 0$ therefore,

$$\Gamma_d(\omega_0) = \frac{2\Gamma_d'}{\Delta\omega} \tag{4.8}$$

where $\Delta\omega = \omega_2 - \omega_1$. The group delay for subsequent resonators can be similarly expressed by placing a shunt conductance after a series reactance (inductor) of the low pass prototype and a series resistance after a shunt reactance (capacitor). The limit of the group delay is then taken as the inserted series resistance or conductance tends to infinity. This is analogous to detuning (shorting) a parallel resonator after the bandpass transformation.

Hilbert transform derived group delay

The relationship between the phase response and the magnitude of a minimum phase network is well known. This relationship is shown below in (4.9) for the continuous case where $\alpha(\xi) = \ln(|H(\omega)|)$ [101]

$$\begin{aligned}\phi_m(\omega) &= \frac{-1}{\pi}\int_{-\infty}^{\infty}\frac{\alpha(\xi)}{\omega-\xi}d\xi \\ &= \frac{-1}{\pi\omega} * \alpha(\omega).\end{aligned} \tag{4.9}$$

By transforming the convolution to frequency domain (with v as the post-FFT trans-

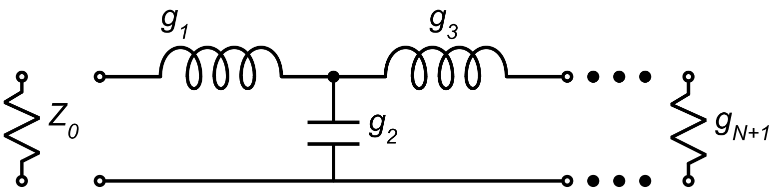

(a) Low-pass filter prototype

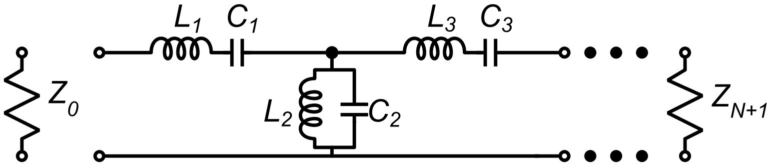

(b) Bandpass transformation

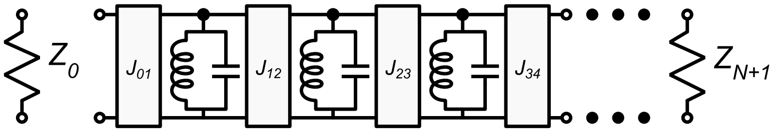

(c) Inverter coupled resonator model

Figure 4.2: Coupled resonator filter design process

formation frequency domain variable) and moving to the discrete case we have,

$$\phi_h(\omega) = IFFT\left(FFT(\alpha(\omega)) \cdot (-j \cdot sign(v))\right). \tag{4.10}$$

Here, FFT and IFFT denote the fast Fourier transform and inverse fast Fourier transform respectively.

In the case of bandpass networks we only desire the magnitude response from ω_l to ω_h and as a result perform the same operation over these bounds. This results in an approximation of the actual phase response. Experiments and simulations in [101] and those performed by us show that the error is approximately constant across the band of interest. This group delay function was termed in [101] as Hilbert transform derived relative group delay or HGD for short and will be so called here as well.

The simulated HGD versus simulated group delay response for a 3rd order Chebyshev filter at 14 GHz with the third resonator detuned is shown in Fig. 4.3. Note that the error is effectively flat over the band of interest (frequency range with local extrema).

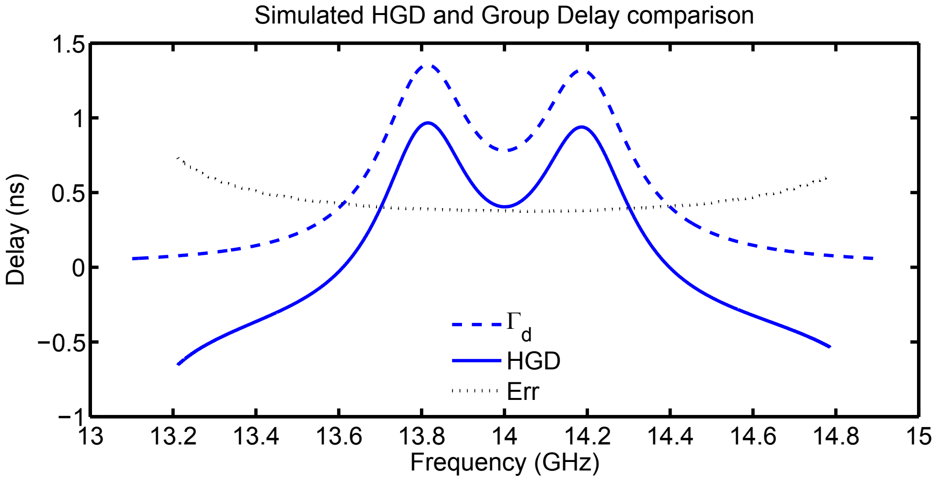

Figure 4.3: Simulated comparison between HGD and group delay showing the simulated group delay, HGD and the difference $Err = \Gamma_d - HGD$.

Relative group delay tuning method

The group delay tuning method described by Ness in [73] proceeds by shorting or detuning all the resonators and sequentially tuning each resonator and coupling value in turn starting from the input and proceeding one by one to the output. At each step, the goal is to tune the magnitude of the actual group delay of S_{11} at the center frequency while maintaining symmetry across the center frequency (f_0).

The magnitude of the group delay is not a reliable tuning criterion when using the HGD due to the magnitude shift introduced by the approximation of the Hilbert transform. To overcome this, a template is created for each tuning step by applying the same transformation parameters to the filter design model and the measured response. The transformation parameters are center frequency, span, number of samples and the length of the FFT/IFFT operations as well as any smoothing aperture that may be used to reduce the noise of the numerical computation.

The tuning templates for the three steps of a 3 pole filter tuning example from Section 4.1.2 is shown below in Fig. 4.4. The templates were generated using the coupling matrix filter model and detuning the specified resonators by setting the appropriate diagonal element of the coupling matrix to a high value.

Intuitively, if a resonator is perfectly shorted then there should be no transmission and therefore no signal from which to derive the Hilbert transform. In Section 4.1.1

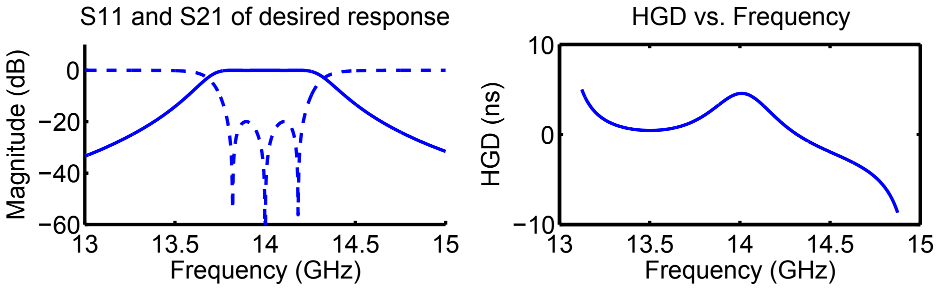

(a) Desired response (b) Resonators 2 and 3 detuned

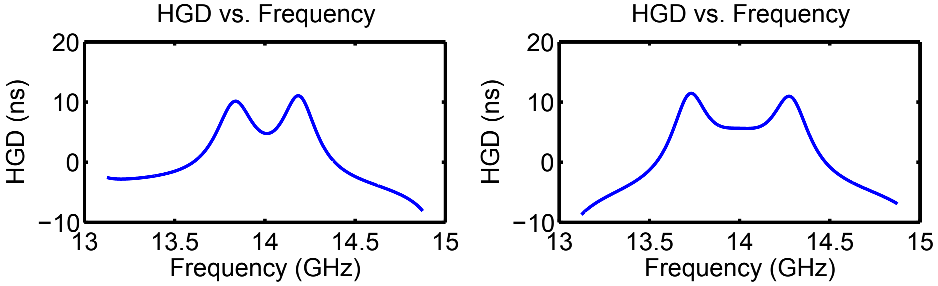

(c) Resonator 3 detuned (d) Final desired response

Figure 4.4: Tuning templates for a 3rd order filter with a center frequency at 14GHz and a bandwidth of 3%: (a) the desired S_{11} and S_{21} magnitude response, (b) HGD vs. Frequency template for step 1 with resonators 2 and 3 detuned, input coupling and resonator 1 are tuned, (c) HGD vs. Frequency template for Step 2 with resonator 3 detuned and tuning resonator 2 and 1-2 coupling and (d) HGD vs. Frequency for perfectly tuned response

we showed that the group delay does indeed approach a limit. Therefore, we do not need to completely short the subsequent resonators. The resonators need to be detuned enough such that they do not impact the in-band group delay while also ensuring that the magnitude of the transmitted signal is within the dynamic range of the measurement system. This introduces a limitation in the order of the filter that can be practically tuned using this technique.

4.1.2 Results

Figure 4.5 shows the simulated versus measured results while tuning the 3-pole filter described above. The HGD and Γ_d show good agreement in the relative measurement. In addition, since the Hilbert transform parameters (center frequency, span, number of points and smoothing aperture) were the same for both the measured and simulated data, the absolute value of the simulated and measured HGD are also in close agreement.

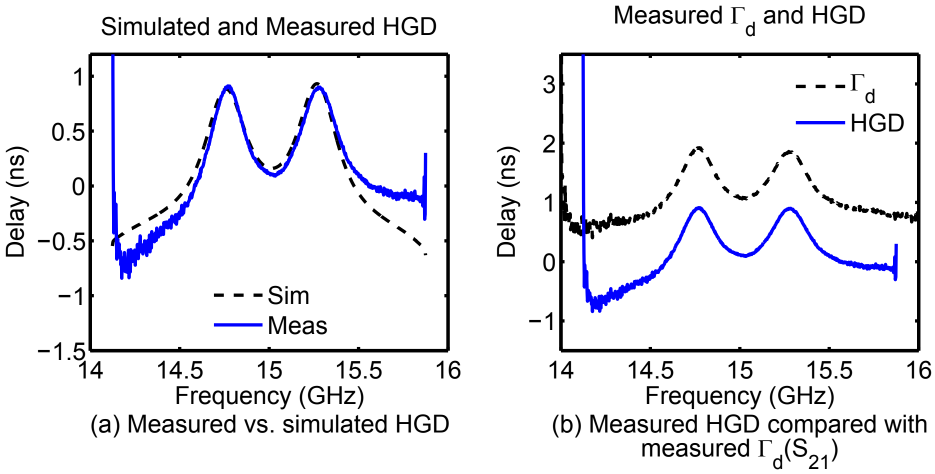

(a) Measured vs. simulated HGD

(b) Measured HGD compared with measured $\Gamma_d(S_{21})$

Figure 4.5: Comparison between measured and simulated HGD (a) and the actual measured Γ_d (b) from the VNA while resonator 3 is detuned.

To illustrate the tuning technique we now proceed to tune a 3-pole inductively coupled, coupled cavity waveguide filter. To demonstrate the concept, we use the VNA as an SNA, i.e. we only use the magnitude information of S_{21} to derive the group delay. During the tuning process we *only* use the derived HGD data for tuning. The magnitude response is shown in the figures below for illustration purposes only and was not used during the tuning process.

First, we detune resonators 2 and 3 and adjust the input coupling and resonator 1 to match the response shown in Fig. 4.6. To adjust the frequency of the peak of the HGD we tune the resonator frequency and to tune the magnitude we adjust the input coupling. Note the noisy signal due to the measurement system approaching the limit of its dynamic range. This is due to the use of a high intermediate frequency in the VNA setup to reduce sweep time.

Next, we tune resonator 2 and the 1-2 coupling to match the response generated by the filter model as shown in Fig. 4.7. Here, we also illustrate the meaning of *sufficiently* detuned. Note in Fig. 4.7a the group delay appears shifted up in frequency, yet when we detune the third resonator some more as shown in Fig. 4.7b we see that the response is in fact precise. However, at this level of detuning, we note that both the magnitude and HGD response appears more noisy as we approach the limit of the instrument's dynamic range.

Finally, we tune resonator 3, the 2-3 coupling and the output coupling to arrive at

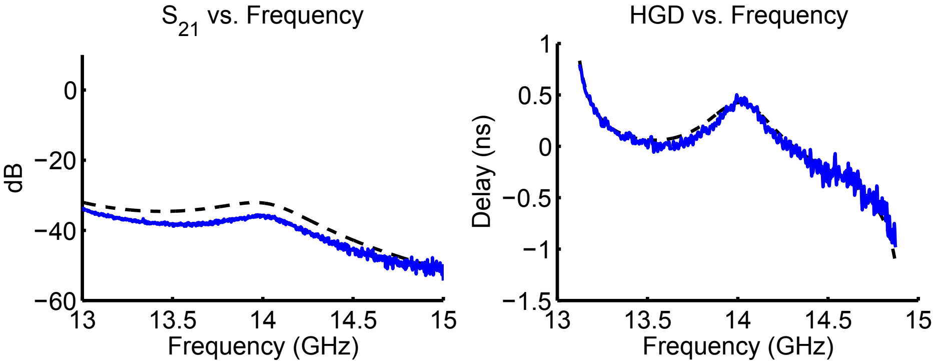

Figure 4.6: Tuning step 1: Tuning resonator 1 and input coupling while resonators 2 and 3 are detuned. (Dashed line is simulated while solid line is measured)

the response shown in Fig. 4.8. This seems like a more daunting task than the previous steps but each tuning element affects the group delay in a unique fashion. Tuning the 2-3 coupling primarily affect the gap between the peaks of the response while tuning the output coupling determines the magnitude of the dip between the peaks. Meanwhile, the resonator is tuned to achieve symmetry. A good agreement was achieved between the desired and final tuned response demonstrating the usefulness of the method for coarse tuning.

4.1.3 Summary

A Hilbert transform derived group delay tuning technique for synchronous coupled resonator filters that requires only the magnitude response of the transmission was presented. The technique utilizes the Hilbert transform of the transmission response to derive the relative group delay of a series of subfilters whose response is matched to a simulated response. The technique promises to enable quick coarse tuning at a drastically lower hardware cost.

The presented HGD technique is capable of tuning center frequency, input coupling and inter-resonator coupling and is therefore well-suited for low-cost tuning of tune-all filters. However, it requires a swept frequency measurement of the transmission response that is not as fast as a single frequency tuning technique since the frequency synthesizer must settle at at each frequency before a measurement can be taken. The technique presented in the following section uses a scalar measurement at only a single frequency permitting much faster tuning at the expense of an inability to tune input or inter-

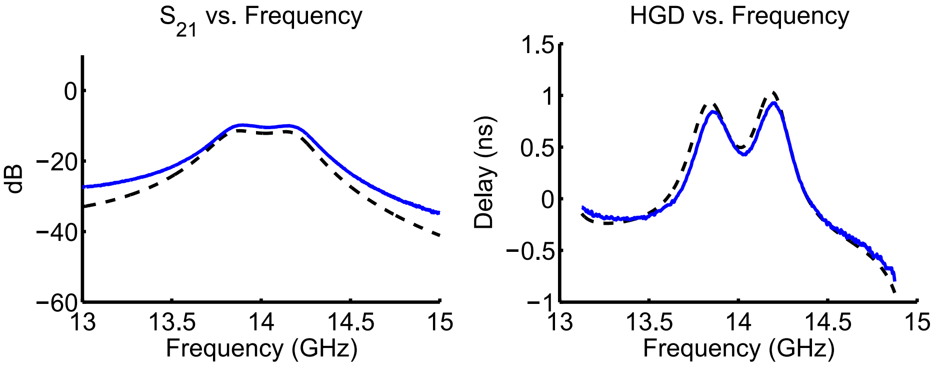

(a) Resonator 3 insufficiently detuned

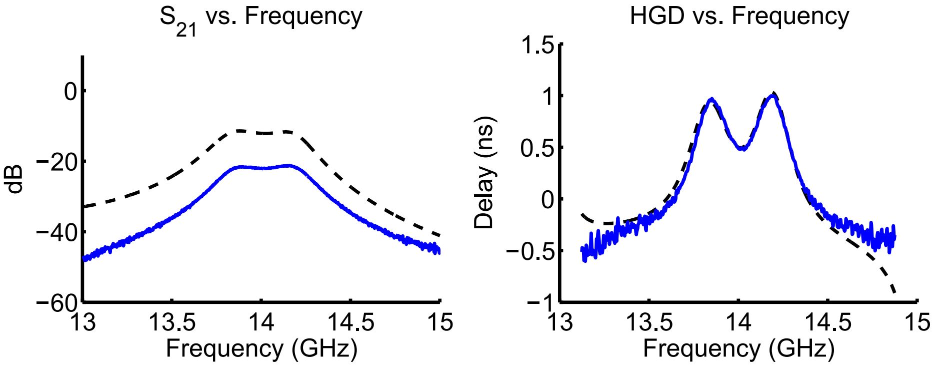

(b) Resonator 3 further detuned

Figure 4.7: Tuning step 2: Tuning resonator 2 and 1-2 coupling while resonator 3 is detuned. The resonator must be sufficiently detuned to eliminate its effects from the HGD response and approach the ideal shorted response. (Dashed line is simulated while solid line is measured)

resonator coupling.

4.2 Automated Scalar Transmission Based Filter Tuning

The work presented here addresses the problem of integrated filter tuning with a low-cost and highly integrated approach. It is envisioned that the proposed technique may be used as an initial calibration method during band switching of a tunable multiband radio system. The proposed tuning algorithm is computationally efficient and only relies on the measurement of the transmission response of the tunable filter for full calibration/tuning

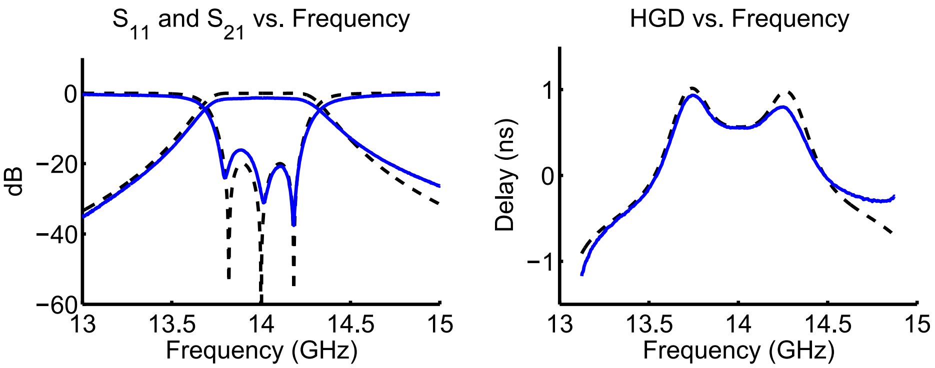

Figure 4.8: Tuning step 3: Tuning resonator 3, output coupling and 2-3 coupling. The rest of the parameters were tuned in the preceding steps. (Dashed line is simulated while solid line is measured)

of Chebyshev-class filters.

4.2.1 Algorithm Description

The proposed scalar transmission-based tuning algorithm relies on a sequential tuning concept similar to the Hilbert transform-derived group delay tuning method [74], group delay tuning method [73], and the alternating short and open method [84]. The primary concept borrowed from the other sequential tuning techniques is the assumption of minimal loading if there is *sufficient* separation in center frequency between resonators. Ideally, as in [73] and [84], all detuned resonators are completely short circuited to eliminate the loading effects entirely. A filter with a perfectly shorted resonator will not transmit any signal and, therefore, the techniques of [73] and [84] rely on the measurement of the reflected signal or S_{11}. The measurement of the reflected signal requires the use of directional couplers that make integration more difficult. Therefore, as in [74], we create an *effective* short in the filter by detuning a resonator and measuring the magnitude of the transmission characteristic or $|S_{21}|$. For example, if it is desired that a filter be tuned to a target frequency, f_t, an effective short of a resonator is realized at f_t by ensuring that its resonant frequency is $f_t \pm \Delta f_t$ where Δf_t is chosen to be large compared to the bandwidth of the filter. A limit on the magnitude of Δf_t is imposed by the order of the filter and the dynamic range of the tuning hardware. Incomplete detuning results in finite tuning error due to the loading caused by the incompletely shorted resonators. As shown in Section 4.2.2, as $\Delta f_t \to \infty$ the tuning error tends to zero.

The algorithm begins with the assumption that the filter is tuned at an initial center frequency, f_i, and that the desired (target) center frequency is f_t. Tuning the filter from an initial frequency f_i to a target frequency f_t is referred to as a tuning hop. If $\Delta f_t = |f_t - f_i|$ is sufficiently large, such that a resonator tuned at f_i appears as an *effective* short at frequency f_t, then this tuning hop is performed directly; otherwise, an intermediate tuning hop may be required to achieve a particular frequency tuning accuracy. A frequency hop from f_i to f_t proceeds as follows.

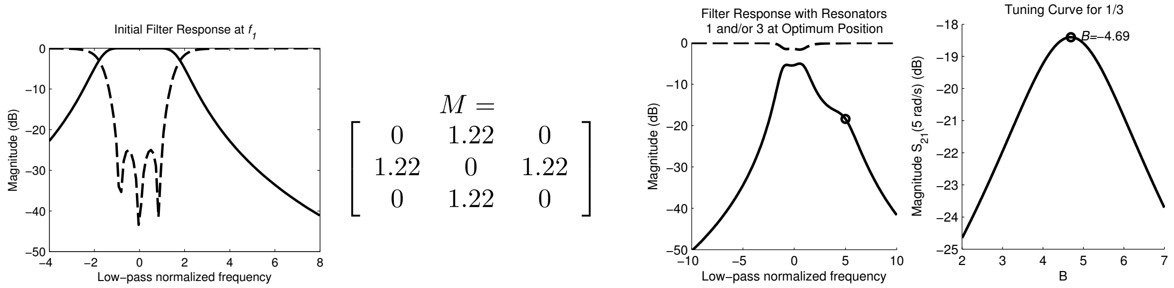

$$M = \begin{bmatrix} 0 & 1.22 & 0 \\ 1.22 & 0 & 1.22 \\ 0 & 1.22 & 0 \end{bmatrix}$$

(a) Initial response at $\vec{S_i}$

(b) Resonators 1 (3) at $S_{t1/3}$

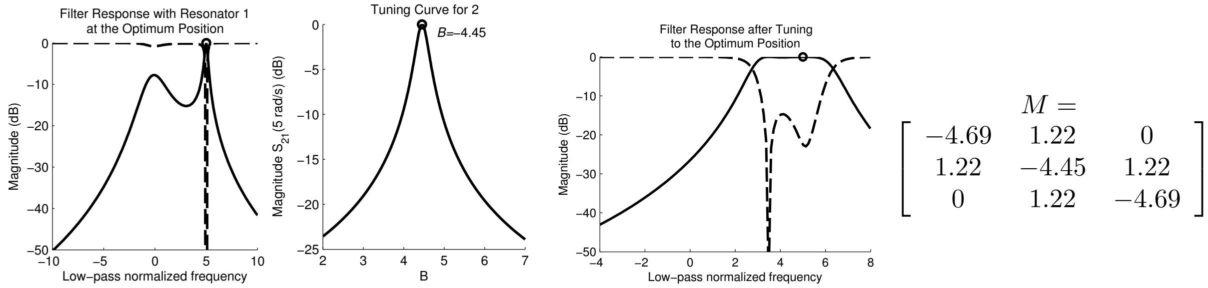

$$M = \begin{bmatrix} -4.69 & 1.22 & 0 \\ 1.22 & -4.45 & 1.22 \\ 0 & 1.22 & -4.69 \end{bmatrix}$$

(c) Resonator 2 at S_{t2}

(d) Final response $\vec{S} = \vec{S_t}$

Figure 4.9: The initial filter response using a coupling matrix model for a third order filter with 25 dB return loss is shown in Fig. 4.9a. The filter response at the end of each tuning step and the tuning curves when each resonator is tuned are shown in Fig. 4.9b and Fig 4.9c. The plots for resonators 1 and 3 are the same due to symmetry and are shown in Fig. 4.9b. The final response after setting the algorithm determined coupling matrix values is shown in Fig. 4.9d.

A tuning hop commences with the position of all the center frequency tuning elements at the initial state $\vec{S_i}$ where $\vec{S_i} = [S_{i1}, S_{i2}, \cdots S_{iN}]$ is the state vector containing the position of each of the tuning elements and N is the number of resonators. It is assumed that the initial state of the filter has all the tuning elements set to the same frequency. The filter tuning process is illustrated using Fig. 4.9 where a coupling-matrix based model is used to illustrate the tuning algorithm. The details of the coupling matrix model are described in Section 4.2.2. Fig. 4.9 represents the filter in the lowpass domain with the initial frequency normalized to 0 rad/s as shown in Fig. 4.9a and, therefore, initial state vector $\vec{S_i} = [0, 0, 0]$. The first resonator is swept from its initial position, S_{i1}, to find the position of the tuning element that results in a maximum of signal transmission through the filter at the target frequency f_t =5 rad/s as shown in Fig. 4.9b. A sample filter response with the first tuning element set to the position of maximum transmission at f_t is shown in Fig. 4.9b with the tuning curve used to find the point of maximum transmission shown next to the filter response. The tuning element position resulting in the maximum transmission at f_t is recorded in the target state vector $\vec{S_t}$ as $S_{t1} = -4.69$. The first resonator is returned to its initial state $S_{i1} = 0$ such that it appears as an effective short for the tuning of the subsequent resonators; thus, completing the tuning of the first resonator. The algorithm resumes with the second tuning element being swept to determine S_{t2}, as shown in Fig. 4.9c, and so on until the complete target state vector $\vec{S_t} = [S_{t1}, S_{t2}, \cdots S_{tN}]$ is determined. The tuning hop is completed by positioning all the tuning elements to positions recorded in the target state vector $\vec{S_t}$—thus, nominally tuning the filter at the target frequency, $f_t = 5$ rad/s as shown in Fig. 4.9d. The tuning curves shown adjacent to the filter response in Fig. 4.9b and Fig. 4.9c are formed as plots of $|S_{21}|$ vs. tuning element state, S_{tn}, at the target frequency f_t. The tuning curves of $|S_{21}|$ vs. S_{tn} are well behaved containing a single maxima and are, therefore, amenable to peak finding using simple optimization routines.

An integrated tunable system would implement the tuning algorithm as follows. A frequency synthesizer, such as the phase locked loop (PLL) of a transceiver, is set to the target frequency, f_t, of the filter. The first tuning element state is swept over its entire state space with the magnitude of transmission being noted over the full sweep. The maximum of transmission is determined and the state of the tuning element at the point of maximum transmission is recorded as S_{t1}. The tuning element is returned to its starting position S_{i1}. The same process is repeated with each tuning element to find the complete target state vector $\vec{S_t}$. Upon completing the process with the final resonator, the target state vector is applied to the filter to set it at the algorithm determined target frequency.

The maximum hop is limited by the dynamic range of the filter characterization hardware. The dynamic range of a single chip transceiver implementation would most likely be limited by the isolation between the receive and transmit signal chains since both signal chains would be tuned to the same frequency, f_t. In the case of a single chip transceiver this is on the order of 30 to 40 dB. The isolation between the signal source (PLL) and the receiver effectively sets the limit on the dynamic range of the transmission measurement. Due to the limitations imposed by the dynamic range of the measurement hardware, the adjacent resonators can only be detuned as far as a signal is still detectable with reasonable fidelity at the output of the filter. Tuning of higher order filters also requires higher dynamic range measurement hardware.

4.2.2 Theory

A theoretical basis for the tuning algorithm is developed using a coupling matrix model for coupled resonator filters. The model has already been summarized in Section 2.3 and is reproduced here in (4.11)–(4.14) as an aid to the following discussion. In the following analysis, the frequency invariant elements of the coupling matrix model are used to represent the effects of center frequency tuning.

$$\begin{aligned} S_{11} &= 1 + 2jR_1(\lambda \boldsymbol{I} - j\boldsymbol{R} + \boldsymbol{M})^{-1}_{1,1} \\ S_{21} &= -2j\sqrt{R_1 R_N}(\lambda \boldsymbol{I} - j\boldsymbol{R} + \boldsymbol{M})^{-1}_{N,1} \end{aligned} \tag{4.11}$$

$$\boldsymbol{R} = \begin{bmatrix} R_1 & 0 & \cdots & 0 \\ 0 & 0 & \cdots & 0 \\ \vdots & \vdots & \ddots & \vdots \\ 0 & 0 & \cdots & R_N \end{bmatrix} \tag{4.12}$$

$$\boldsymbol{M} = \begin{bmatrix} 0 & M_{1,2} & 0 & \cdots & 0 & 0 \\ M_{1,2} & 0 & M_{2,3} & \cdots & 0 & 0 \\ 0 & M_{2,3} & 0 & \cdots & 0 & 0 \\ \vdots & \vdots & \vdots & \ddots & \vdots & \vdots \\ 0 & 0 & 0 & \cdots & 0 & M_{N-1,N} \\ 0 & 0 & 0 & \cdots & M_{N,N-1} & 0 \end{bmatrix} \tag{4.13}$$

$$\lambda = \frac{f_0}{f_2 - f_1}\left(\frac{f}{f_0} - \frac{f_0}{f}\right) \tag{4.14}$$

The coupling matrix given in (4.13) is augmented to form the tunable coupling matrix $\boldsymbol{M_t}$ by introducing frequency invariant reactances into the main diagonal of the coupling matrix as given in (4.15). In (4.15), $\boldsymbol{I}$ is the NxN identity matrix and $\vec{S}$ is the state vector of the tunable filter where $\vec{S} = [B_1, B_2, \cdots, B_N]$. The B_i frequency invariant reactances model the tuning elements of the filter and end up on the main diagonal of the tunable coupling matrix $\boldsymbol{M_t}$. All the elements of the state vector are initially set to zero. The initial state, $\vec{S_i} = [0, 0, \cdots, 0]$, represents the filter tuned at its initial center frequency f_i. A filter exhibiting an ideal equal-ripple Chebyshev response has all the diagonal elements of its coupling matrix set to 0. Effectively, the tunable filter bandpass response is normalized to the lowpass domain such that the initial center frequency f_i is normalized to 0 rad/s in the lowpass domain.

$$\boldsymbol{M_t}(\vec{S}) = \boldsymbol{M} + \vec{S}\boldsymbol{I} \tag{4.15}$$

The tunable coupling matrix of (4.15) is substituted into the expressions relating the S-Parameters and the coupling matrix (4.11) and yield the S-Parameters as a function of the state vector and frequency as given in (4.16). Thus, (4.16) gives the S-Parameters as a function of the state of the filter tuning elements. The effectiveness of the tuning algorithm is now evaluated using the model relating the state of the tunable filter and the S-Parameters.

$$\begin{aligned} S_{11}(\vec{S}, \lambda) &= -2jR_1(\lambda\boldsymbol{I} - j\boldsymbol{R} + \boldsymbol{M_t}(\vec{S}))^{-1}_{1,1} - 1 \\ S_{21}(\vec{S}, \lambda) &= -2j\sqrt{R_1 R_N}(\lambda\boldsymbol{I} - j\boldsymbol{R} + \boldsymbol{M_t}(\vec{S}))^{-1}_{N,1} \end{aligned} \tag{4.16}$$

The algorithm within the context of the tunable filter model is described as follows. The magnitude of the filter transmission at the target frequency f_t is found by evaluating the magnitude of S_{21} as a function of the state vector $\vec{S}$ at the frequency f_t or $|S_{21}(\vec{S}, f_t)|$. The maximum of transmission at f_t is found for each resonator by solving the set of independent equations given in (4.17). The resulting vector $\vec{S}_t' = [B_1', B_2', \cdots, B_N']$ is the scalar algorithm-determined target state vector. The $'$ superscript designates a value determined by the scalar tuning algorithm. The ideal tuning states are designated with a

* with the ideal target state vector designated S_t^*. The tuning error vector is now defined as $\vec{E}_t = \vec{S}_t' - \vec{S}_t^*$.

$$\begin{aligned}\frac{\delta|S_{21}([B_1', 0, \cdots, 0], f_t)|}{\delta B_1'} &= 0\\ \frac{\delta|S_{21}([0, B_2', \cdots, 0], f_t)|}{\delta B_2'} &= 0\\ \vdots \;\vdots &\;\vdots\\ \frac{\delta|S_{21}([0, 0, \cdots, B_N'], f_t)|}{\delta B_N'} &= 0\end{aligned} \tag{4.17}$$

The tuning algorithm model of (4.17) is confirmed to result in analytical solutions regardless of the order of the filter. The analytical results of the modeled tuning algorithm serve to illustrate the fundamental limitations of the tuning approach and to aid in determining the bounds on the tuning error. The relationship between the target center frequency f_t and the ideal state vector $\vec{S}_t^*$ for perfect tuning is easily solved. A resonator i that is desired to have a lowpass normalized resonant frequency of +1 rad/s needs to have $B_i = -1$. Therefore, $\vec{S}_t^*(f_t) = [-f_t, -f_t, \cdots, -f_t]$. The solution of (4.17) evaluates the result of the tuning algorithm and captures the systematic errors of imperfect detuning. The error function for a particular element of the tuning state is defined in (4.18)

$$E_t(f_t) = S_t'(f_t) + f_t \tag{4.18}$$

where $S_t'(f_t)$ is the tuning algorithm determined state for the target frequency, f_t.

A Quantitative Example of the Modeled Tuning Algorithm

The behavior of the tuning algorithm is illustrated with a numerical example based on the tunable coupling matrix presented above. A third order filter with 25 dB return loss is used as the example. The low order filter is typical of what may be encountered in a front-end filter and results in manageable symbolic algebraic solutions in print form. Higher order solutions are still analytical but result in long symbolic expressions.

The coupling matrix $\boldsymbol{M}$ and load matrix $\boldsymbol{R}$ are given in (4.19) and (4.20), respectively, for the specific case of this filter example. This synthetic example is identical to the one used in Section 5.1 with response curves shown in Fig. 4.9.

$$\boldsymbol{M} = \begin{bmatrix} 0 & 1.2197 & 0 \\ 1.2197 & 0 & 1.2197 \\ 0 & 1.2197 & 0 \end{bmatrix} \tag{4.19}$$

$$\boldsymbol{R} = \begin{bmatrix} 1.4918 & 0 & 0 \\ 0 & 0 & 0 \\ 0 & 0 & 1.4918 \end{bmatrix} \tag{4.20}$$

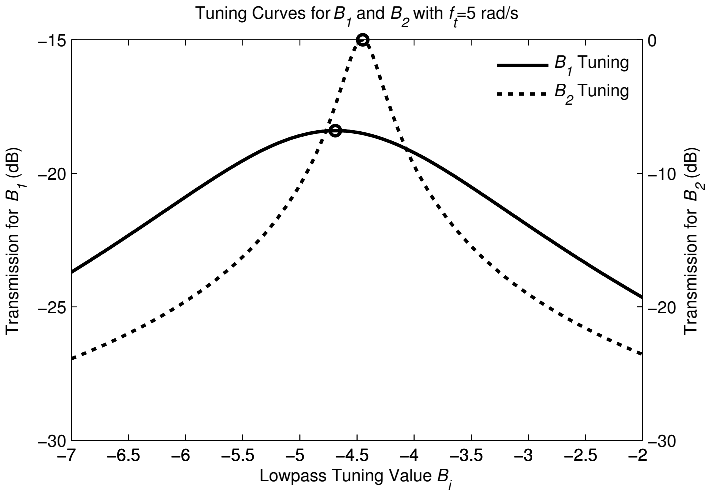

Figure 4.10: Tuning curves for elements B_1 and B_2 of the tunable coupling matrix (4.19). The curves are generated by plotting $|S_{21}([B_1, 0, 0], 5)|$ and $|S_{21}([0, B_2, 0], 5)|$ as a function of B_1 and B_2, respectively. These plots are analogous to generating a transmission magnitude sweep versus tuner position for $f_t = 5$ rad/s.

The squared magnitude response of the transmission coefficient for a third order filter can be expressed as (4.23) for the outer resonator tuning case $S_{21}([B_1, 0, 0], f_t)$ and middle resonator tuning case $S_{21}([0, B_2, 0], f_t)$. The outer resonator tuning functions apply to both resonators 1 and 3. In order to find the tuning curves shown in Fig. 4.10, $f_t = 5$ is substituted into the expressions given in (4.23) and the magnitude of transmission $|S_{21}|$ is plotted versus B_i with the coupling matrix values for $\boldsymbol{M}$ and $\boldsymbol{R}$ substituted from (4.19) and (4.20), respectively. The expressions for the magnitude of transmission versus the values of B_1 and B_2 for this filter example are given in (4.21) and (4.22), respectively.

The plot of Fig. 4.10 indicates that a dynamic range of at least 20 dB is necessary to identify the transmission peak for resonators 1 and 2 at a lowpass hop distance of 5 rad/s.

$$|S_{21}|(B_1) = \frac{4.4386}{\sqrt{608.4664B_1^2 + 5701.7713B_1 + 14721.4227}} \tag{4.21}$$

$$|S_{21}|(B_2) = \frac{4.4386}{\sqrt{741.2261B_2^2 + 6602.2115B_2 + 14721.4227}} \tag{4.22}$$

$$|S_{21}(B_1, f_t)|^2 = 4\,\frac{{M_{1,2}}^4 R^2}{f^6 + 2\,f^5 B_1 + \left(-4\,{M_{1,2}}^2 + {B_1}^2 + 2\,R^2\right) f^4 + 2\,B_1\,\left(-3\,{M_{1,2}}^2 + R^2\right) f^3 +} \cdots \tag{4.23}$$

$$\cdots \frac{}{\left(-2\,{M_{1,2}}^2 + R^2\right)\left(R^2 - 2\,{M_{1,2}}^2 + {B_1}^2\right) f^2 - 2\,{M_{1,2}}^2 B_1\,\left(-2\,{M_{1,2}}^2 + R^2\right) f + {M_{1,2}}^4\left(4\,R^2 + {B_1}^2\right)}$$

$$|S_{21}(B_2, f_t)|^2 = \frac{4\,{M_{1,2}}^4 R^2}{\left(R^2 + f^2\right)\left(f^4 + 2\,B_2\,f^3 + f^2 R^2 - 4\,f^2 {M_{1,2}}^2 + f^2 {B_2}^2 + 2\,f\,R^2 B_2 - 4\,f\,B_2\,{M_{1,2}}^2 +\right.} \cdots$$

$$\cdots \frac{}{\left. 4\,{M_{1,2}}^4 + {B_2}^2 R^2\right)} \tag{4.24}$$

In the normalized lowpass domain a shift of +1 rad/s in frequency is the result of setting the diagonal elements of the coupling matrix to -1. However, it has been noted that the effects of non-ideal detuning will hamper the performance of the algorithm. As seen in Fig. 4.10, the maxima of transmission at the target frequency of $f_t = 5$ rad/s does not occur at the ideal value of -5. This highlights the presence of error inherent in the tuning algorithm.

Taking the derivatives of the expressions (4.21) and (4.22) with respect to B_1' and B_2', respectively, and equating them to zero allows expressions for the tuned resonant frequency with respect to target frequency to be developed as given in (4.25) and (4.26), respectively. In order to quantify the effects of non-ideal detuning on the proposed tuning algorithm, the tuning error function can be found by taking the difference of the solution of (4.17) and $S_t^*(f_t) = [-f_t, -f_t, -f_t]$. The error can be expressed versus target frequency to determine the size of the required step and the expected magnitude of the inherent tuning error using (4.18). The result of the tuning law (4.17) for the outer and middle resonators in the case of the example third order filter are listed in (4.25) and (4.26), respectively, where $B_i'(f_t)$ is the algorithm-derived diagonal element value as a function of the target frequency f_t.

$$B_1'(f_t) = -\frac{f_t\,\left(2\,{M_{1,2}}^4 + R^2{f_t}^2 - 3\,{M_{1,2}}^2{f_t}^2 + {f_t}^4 - {M_{1,2}}^2R^2\right)}{-2\,{M_{1,2}}^2{f_t}^2 + {M_{1,2}}^4 + {f_t}^4 + R^2{f_t}^2} \tag{4.25}$$

$$B_3'(f_t) = B_1'(f_t)$$

$$B_2'(f_t) = -\frac{\left({f_t}^2 - 2\,{M_{1,2}}^2 + R^2\right)f_t}{{f_t}^2 + R^2} \tag{4.26}$$

The limit of the expressions (4.25) and (4.26) as f_t approaches infinity is $-f_t$. Consequently, the tuning error as given in (4.18) will tend to zero as f_t approaches $\pm\infty$. It should also be noted that since the initial center frequency is normalized to 0 rad/s in the lowpass domain the initial center frequency is always $f_i = 0$ in the lowpass domain. Therefore, the tuning hop magnitude $|f_t - f_i| = |f_t|$ in this example since we are formulating the theory in the normalized lowpass domain.

The tuning error for the example filter is plotted with respect to target frequency f_t for the tuning of the middle resonator tuning element (B_2) and end resonator tuning element (B_1) and is shown in Fig. 4.11. The magnitude of the tuning error is shown in Fig. 4.11 for both the middle and end resonators versus the size of the tuning hop $|f_t - f_i|$ in both the downward and upward tuning directions as shown in Fig. 4.11a and Fig. 4.11b, respectively. Fig. 4.11 shows the tuning error rises quickly if a small step is made from the initial passband. The error is at a maximum as the tuning hop distance approaches the vicinity of the band edge of the filter's initial state where the adjacent resonators are insufficiently detuned. Therefore, for the assumption of minimal loading to hold true, the hop should be at least a couple of filter bandwidths away to be performed directly. The error can be ensured to be below a certain threshold if the hop size is maintained above a prescribed minimum. The tuning error decreases with the tuning hop distance once the maximum near the initial filter band edge is passed.

In Fig. 4.11a two tuning offsets are noted for comparison. Tuning offset (a) is 3 rad/s while tuning offset (b) is 9 rad/s. Both tuning offsets (a) and (b) are in the negative tuning direction with $f_t < f_i$ or $f_t = -3$ rad/s and $f_t = -9$ rad/s, respectively. The algorithm-tuned response for tuning offsets (a) and (b) are shown using solid lines in Fig. 4.12 with $S_t = [B_1'(f_t), B_2'(f_t), B_3'(f_t)]$. The ideal filter response at $f_t = -3$ rad/s and $f_t = -9$ rad/s are shown with dotted lines where $S_t = [-f_t, -f_t, -f_t]$. The comparison in Fig. 4.12 shows that the response at offset (b) is closer to the ideal dotted response than

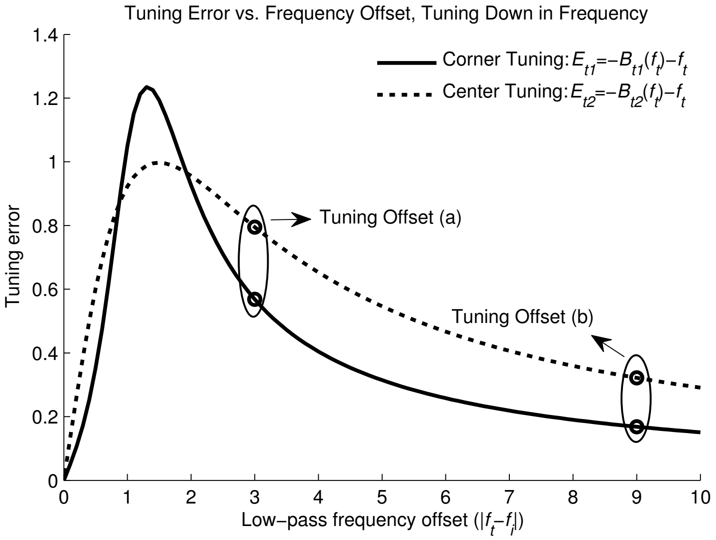

(a) Tuning down ($f_t < f_i$)

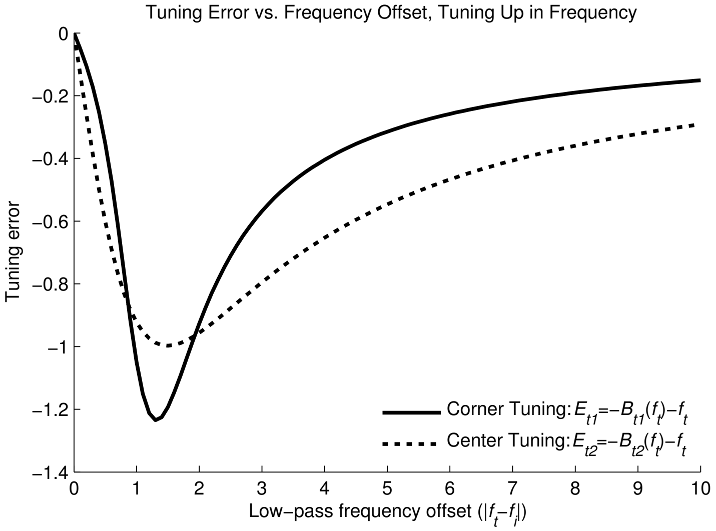

(b) Tuning up ($f_t > f_i$)

Figure 4.11: The magnitude of the tuning error versus frequency offset for tuning in the downward (Fig. 4.11a) and upward (Fig. 4.11b) cases. Error curves are shown for both the outer (E_{t1}) and middle (E_{t2}) resonators.

the response at offset (a). The result at offset (a) shows a greater center frequency error compared to offset (b) since it is the result of a smaller tuning hop. In both offsets (a) and (b) the algorithm-tuned filter response errs on the side of the initial center frequency.

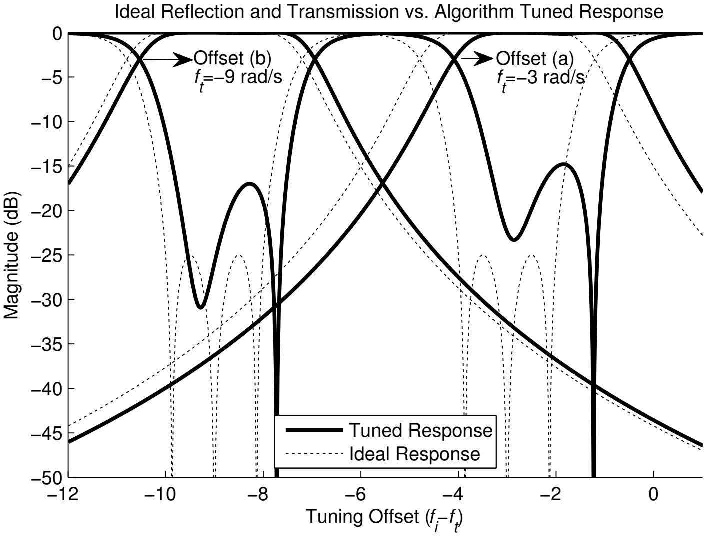

Figure 4.12: A lowpass normalized prototype comparison of an ideal third order Chebyshev coupling matrix response and that of a worst-case tuned Chebyshev filter using the proposed tuning algorithm with 25 rad/s error. The ideal response is shown with the dotted curves while the algorithm-tuned response is shown with solid lines.

In general, the coupling element values $M_{i,j}$ do not remain constant over all tuning states of the tunable filter state vector $\vec{S}$ as assumed by this model. A filter with constant $M_{i,i+1}$ and R is a filter with constant fractional bandwidth. It is often more desirable for a tunable filter to exhibit constant absolute bandwidth over the center frequency tuning range. However, it is noted that many tunable filters exhibit a nearly constant fractional bandwidth making this model fairly accurate in those cases [25, 30, 43]. The presented analytical model results in a reasonable approximation of the tuning behavior in general and serves as an adequate model to illustrate the concept and limitations of the proposed tuning scheme.

4.2.3 Measured Results

Two measurement hardware configurations are presented for the validation of the scalar tuning algorithm. One hardware configuration uses a traditional VNA instrument for both scalar measurement and final filter characterization. The other configuration uses a discrete PLL circuit as a continuous-wave signal source and a log-amplifier detector to form a low-cost scalar measurement system. The VNA measurement setup serves to illustrate the accuracy of the tunable filter model and verify the postulates of the tuning algorithm, while the scalar hardware measurement setup serves to demonstrate the capability of a low-cost hardware implementation of the algorithm.

A large scale tunable filter is used to demonstrate the performance of the algorithm. The tunable filter is a servo-motor-controlled evanescent mode coupled rectangular coaxial cavity combline filter. Tuning is accomplished using #4-40 tuning screws that are automatically adjusted using flexible couplings driven by servo motors. The same flexible coupling/servo motor configuration was used in [71] to demonstrate post-production filter tuning using automated fuzzy logic techniques.

Initialization of the tunable filter hardware is done manually by homing the servo actuators at the lowest possible position (screws inserted as far into the cavity as possible) without shorting the tuning screw to the resonator post. This lowest-most position corresponds to an encoder reading of 0 counts. Turning the motor in the positive direction, so as to increase the encoder count, retracts the screw out of the cavity and increases the resonance frequency of the resonator being tuned. The coaxial resonator tunable filter has a tuning range of 800 MHz (from 4 GHz to 4.8 GHz). The tuning characteristic of the rectangular coaxial resonator versus screw position is simulated in Ansoft HFSS. The tuning screw is modeled as a smooth-walled cylinder with a diameter of 2.72 mm, corresponding to the minimum major diameter of a #4 screw. A parametric simulation was performed using Ansoft HFSS to determine the center frequency tuning characteristic of the cavity and is shown in Fig. 4.13. The result shown in Fig. 4.13 is nonlinear. Therefore, in order to ensure a constant frequency resolution across the tuning range, the function shown in Fig. 4.14 is applied to linearize the response between sweep step and resonator frequency. Fig. 4.14 is an inversion of the simulated tuning response of Fig. 4.13. The linearized frequency step characteristic of Fig. 4.14 was used for both the VNA and scalar measurement hardware configurations.

Scalar Measurement Based Tuning Implementation Using a VNA

A block diagram of the VNA-based test configuration is shown in Fig. 4.15. A PC running LabVIEW is used to run the algorithm while the VNA is used to measure

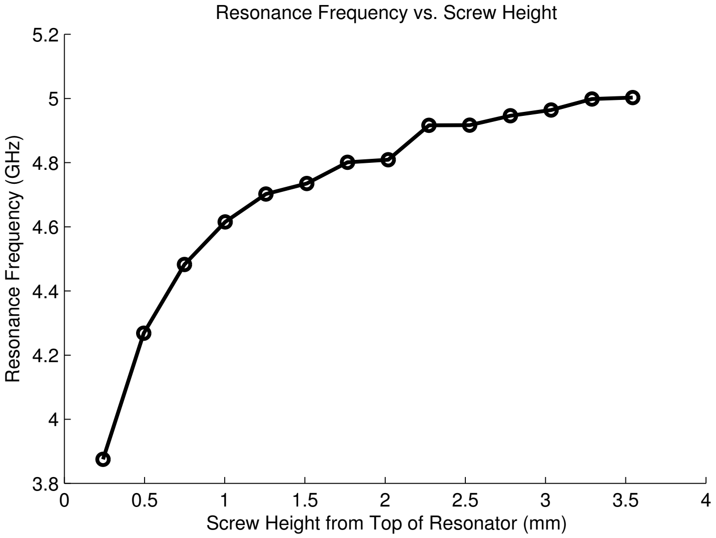

Figure 4.13: Center frequency tuning characteristic for the center frequency resonator results obtained from simulation using Ansoft HFSS.

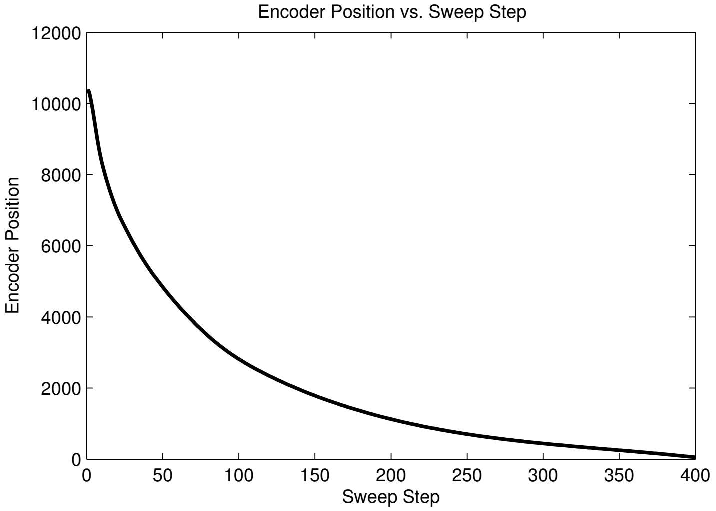

Figure 4.14: Encoder position versus tuning sweep step. This curve inverts the tuning characteristic to approximate a linear response between sweep step and resonator frequency.

the log-magnitude of the transmission response of the filter during the tuning process. During the tuning process, the VNA is used strictly to measure the relative transmission magnitude. After a particular tuning hop is completed, the VNA is returned to its vector measurement state to capture the complete two-port characteristics of the filter. In this fashion, both tuning and response validation is performed in a single physical configuration.

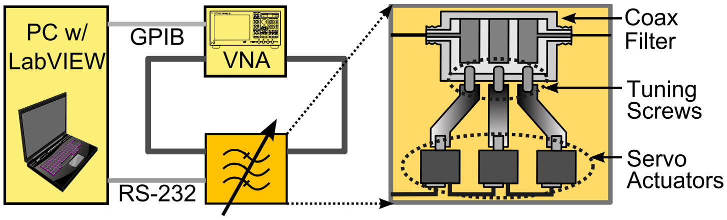

Figure 4.15: Tuning algorithm model validation setup using a VNA for the measurement of the transmission magnitude response.

The tuning algorithm is tested over two multi-hop scans of the tuning range in the increasing frequency (upward) and decreasing frequency (downward) directions as shown in Table 4.1. The initial frequency position, f_i, for each of the upward hops is set to 4 GHz while the f_i for each of the downward hops is set to 4.8 GHz. During each actuator tuning sweep the VNA is set to continuous wave mode at the target frequency of the hop. Eleven samples of the transmission response are taken over 5.5 ms and averaged for each sample of the transmission magnitude versus actuator position sweep. The actuator tuning sweeps generate the three tuning curves, one for each resonator, as shown in Fig. 4.16. Once the tuning curves of Fig. 4.16 are generated for a particular hop, the positions resulting in maximum transmission are selected as the target positions for each resonator and make up the target state vector $\vec{S_t}$. The tuning hop is concluded by setting the positions of the actuator to the determined target positions $\vec{S_t}$ and the complete tuned two-port response is measured over the tuning range of the filter and logged as an s2p file. The initial position is returned to f_i and a new f_t is set on the VNA for the next hop.

The results of the logged s2p files are shown in Fig. 4.17 for the target frequencies of 4200 MHz, 4400 MHz, 4600 MHz and 4800 MHz for the up-sweep (Fig. 4.17a) and 4000 MHz, 4200 MHz, 4400 MHz and 4600 MHz for the down sweep (Fig. 4.17b). These target frequencies are selected to have non-overlapping responses in the same figure.

Table 4.1: Hop sweep configuration for the up sweep and down sweep plans

Hop Number	Up Sweep Freq. f_t (f_i=4000 MHz)	Down Sweep Freq. f_t (f_i=4800 MHz)
1	4200 MHz	4000 MHz
2	4300 MHz	4100 MHz
3	4400 MHz	4200 MHz
4	4500 MHz	4300 MHz
5	4600 MHz	4400 MHz
6	4700 MHz	4500 MHz
7	4800 MHz	4600 MHz

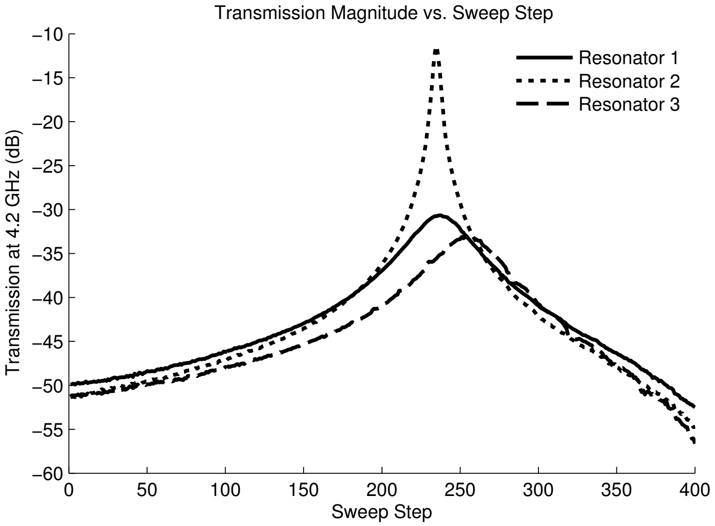

Figure 4.16: The transmission response sweep versus actuator position step for the three tuning actuators while performing a hop from 4.8 GHz to 4.2 GHz. The maximum of the transmission response for each actuator is selected as the tuned position for 4.2 GHz. Note that a nonlinear step size is used based on the simulated tuning characteristic as shown in Fig. 4.14.

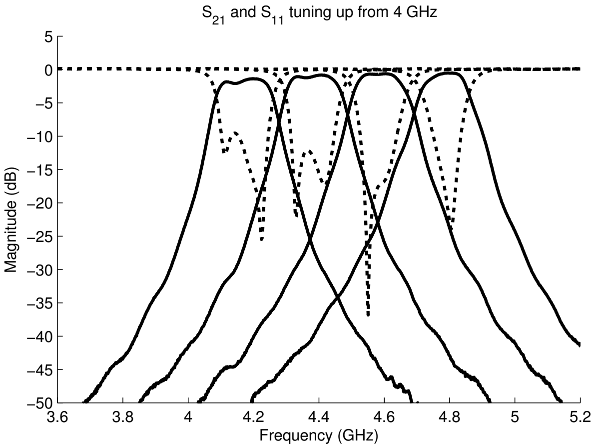

(a) Tuning results using a VNA as a scalar network analyzer for tuning and final measurement for $f_t > f_i$. The f_i is 4 GHz while results are plotted with f_t at 4.2 GHz, 4.4 GHz, 4.6 GHz and 4.8 GHz.

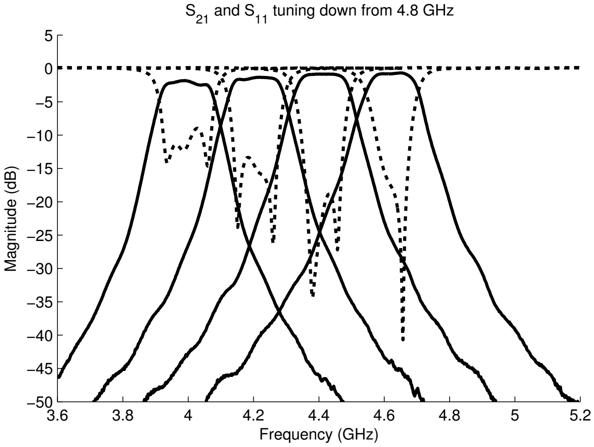

(b) Tuning results using a VNA as a scalar network analyzer for tuning and final measurement $f_t < f_i$. The f_i is 4.8 GHz while results are plotted with f_t at 4 GHz, 4.2 GHz, 4.4 GHz and 4.6 GHz.

Figure 4.17: Upward and downward tuning results compared. The transmission response is shown using solid lines while the reflection is shown with dotted lines.

The scalar algorithm only tunes the center frequency of each resonator. As a result, the return loss shown in Fig. 4.17 is poor at the low end of the tuning range since the coupling tuning screws were fixed for the duration of testing. The algorithm presented here makes no attempt to tune the coupling and, as a consequence, the return loss is determined by the coupling variation with center frequency. The increase in insertion loss with lower frequency is attributed to a reduction in quality factor caused by increased cavity loading as the tuning screws penetrate deeper into the cavity as well as the aforementioned reduced return loss.

The asymmetric response of the reflection coefficient is a result of the second resonator not being tuned to the same frequency as the other two and is predicted by the coupling matrix model. Both the up-sweep and the down-sweep have symmetric responses at their longest hops—4.8 GHz for the up-sweep and 4 GHz for the down sweep. The symmetric response indicates a better tuning accuracy for an increased and is also predicted by the coupling matrix-based tuning model.

Fig. 4.18 shows the return loss comparison for the up and down sweeps at target frequencies of 4.2 GHz, 4.4 GHz and 4.6 GHz. The coupling matrix-based theory predicts that the tuning error for the up-sweep will be negative, meaning that the resulting tuned frequency will be below the target while the tuning error for the down sweep will be positive, meaning that the resulting tuned frequency will be above the target. The results shown in Fig. 4.18 corroborates these expectations. The measured return loss is nearly symmetric about the target frequency when comparing the up- and down-sweep return loss at a particular target frequency (keeping in mind the decreasing return loss with frequency).

A second set of frequency hops was performed in order to verify the tuning error curves predicted by the coupling matrix model. The second set of tuning hops was performed in 25 MHz increments in the up- and down-sweeps with $f_i = 4\,\text{GHz}$ and $f_i = 4.8\,\text{GHz}$, respectively. The center frequency is calculated by taking the average of the two frequencies that bound the 5 dB bandwidth of the filter. The tuning error with respect to the hop distance and direction are shown in Fig. 4.19. As predicted, the tuning error is positive for the down-ward hops and negative for the up-ward hops with the error magnitude decreasing with increasing hop distance.

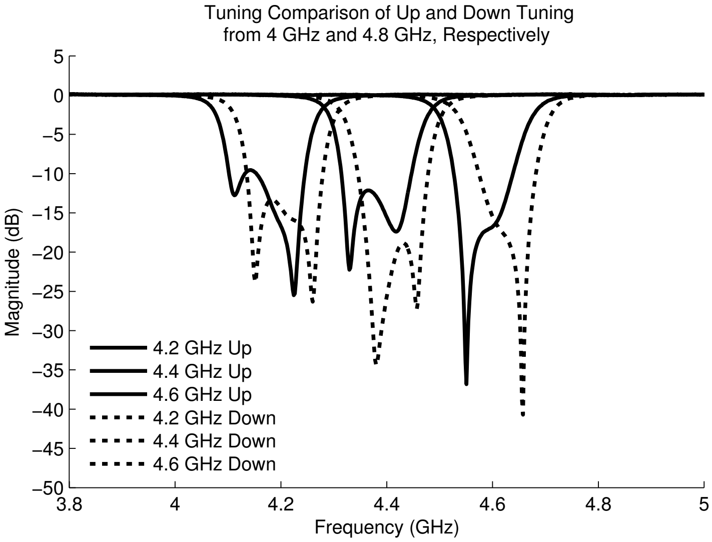

Figure 4.18: The return loss (S_{11}) is plotted for both the up and down sweeps of f_t at 4.2 GHz, 4.4 GHz and 4.6 GHz. The final center frequency is higher than f_t in the down-sweep and less than f_t in the up sweep as predicted by the model. The responses are nearly symmetrical about f_t.

Low Cost Scalar Measurement Hardware Implementation

Two states of the low-cost scalar measurement tuning system are shown in Fig. 4.20. The evaluation system includes two transfer switches that are used to switch the system between scalar tuning and VNA measurement as shown in Fig. 4.20a and Fig. 4.20b, respectively. The scalar measurement portion is composed of a frequency synthesizer and a log detector. Digital control is handled by a LabVIEW application running on a PC platform with a data acquisition board from National Instruments and implementing the described algorithm. A photograph of the prototype hardware with the VNA disconnected is shown in Fig. 4.21.

A schematic of the frequency synthesizer circuit is shown in Fig. 4.22. The frequency synthesizer is composed of an Analog Devices ADF4156 phase locked loop (PLL) and a DCYS300600 voltage controlled oscillator (VCO) from Spectrum Microwave. An active loop filter is used to amplify the 5 V charge pump of the PLL to the 15 V required by the VCO. The synthesizer has a frequency tuning range from 3 to 6 GHz and spans the 4 to 4.8 GHz tuning range of the filter. The PLL is controlled through a 3-wire serial interface using the digital signal lines of the data acquisition card. The power detector

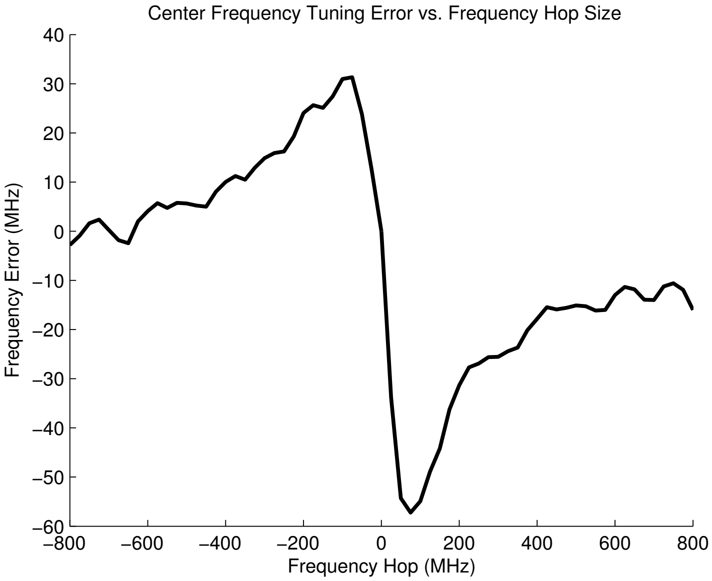

Figure 4.19: Plot of the tuning error versus hop-size with the VNA acting as a scalar analyzer. The results correspond to the curves predicted by the coupling matrix model with a positive error when tuning in the negative direction and a negative error when tuning in the positive direction. The magnitude of the error decreases with the magnitude of the frequency hop, as expected. The center frequency is defined as the center of the 5 dB bandwidth.

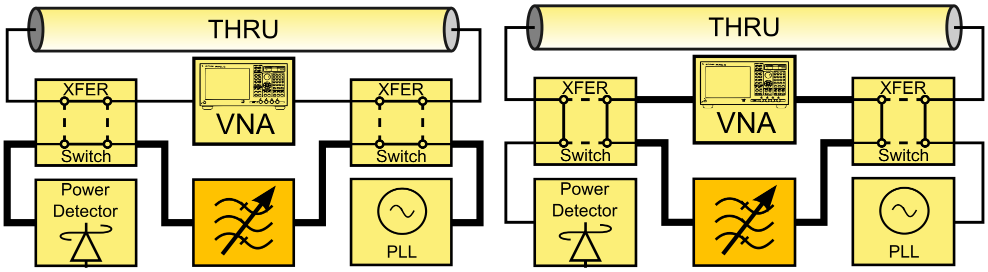

(a) Tuning state (b) Verification state

Figure 4.20: Low-cost scalar tuning setup including VNA measurement for automated testing and evaluation of the tuning algorithm. The signal path through the filter is highlighted in the two states.

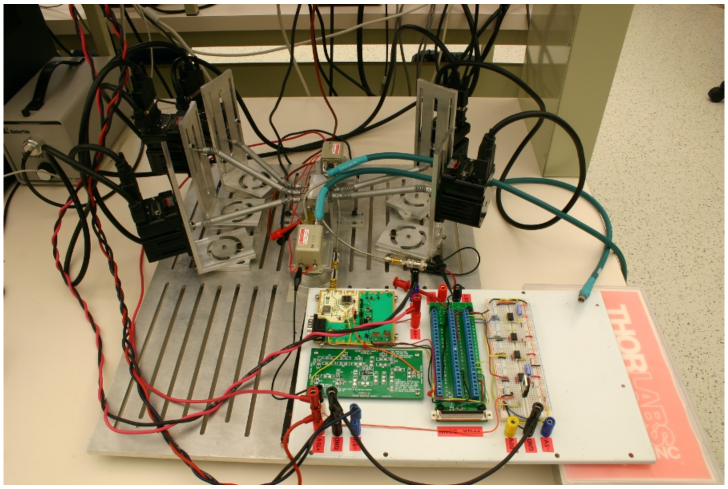

Figure 4.21: A photo of the tuning setup with the VNA disconnected.

is an Analog Devices AD8318 log-amplifier with an analog output voltage proportional to the log of the input power. The log amplifier is interfaced using one of the analog to digital inputs of the National Instruments data acquisition board. The two transfer switches are actuated by using one of the digital signal lines of the data acquisition card to drive a semiconductor switch. Finally, the VNA is interfaced to the LabVIEW application using a GPIB interface.

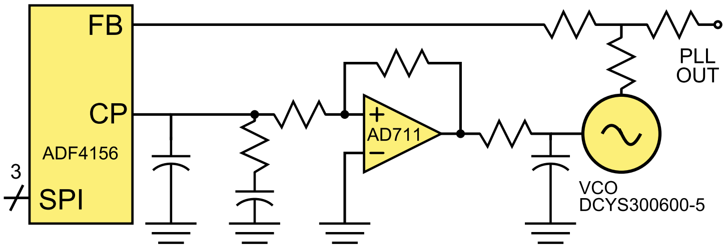

Figure 4.22: A simplified schematic of the PLL circuit.

The two ports of the filter are either connected to the source/detector pair of the scalar tuning hardware as shown in Fig. 4.20a or the VNA for filter performance verification as shown in Fig. 4.20b. This dual configuration is accomplished using two mechanical transfer switches and permits the verification of the tuner performance with a precise calibrated VNA measurement. While the transfer switches are in the verification state (Fig. 4.20b) the scalar measurement hardware is connected to a piece of transmission line permitting a through calibration. The nature of the algorithm does not depend on the absolute value of the scalar measurement and, therefore, the scalar calibration is a redundant step as far as the algorithm is concerned. However, it does serve to illustrate the measurement performance attainable with a simple hardware configuration by permitting a comparison between the VNA measured filter response and that measured using the scalar measurement hardware.

The tuning system and algorithm were evaluated by running a sequence of tuning steps over the full tuning range of the filter. The tuning hops were chosen so as to satisfy the requirements for *sufficient* detuning between steps. In this case, sufficient detuning was chosen as 300 MHz. The three tuning curves for a frequency hop characteristic of the tuning algorithm are shown in Fig. 4.23. The three curves correspond to the tuning sweeps of each of the resonators. The log detector has an output voltage that is inversely proportional to the log of the detected power. The inverse relationship is why the tuning curves result in a minimum as opposed to a maximum value at the output of the analog to digital converter. The results shown in Fig. 4.23 closely resemble the expected shape of the tuning curves as predicted by the coupling matrix based tuning model as shown in Fig. 4.10. The tuning step size is selected based on the simulated tuning model to linearize the frequency step of the resonator tuning sweep as discussed above.

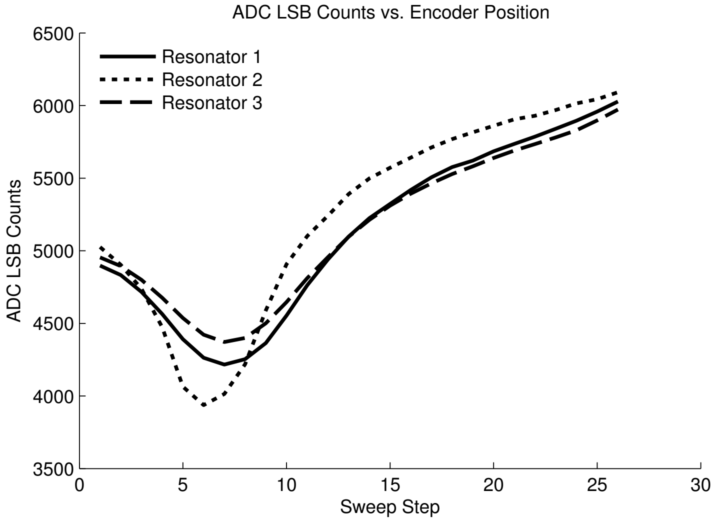

Figure 4.23: Sweep result for a hop from 4.45 GHz to 4.75 GHz plotted versus step index.

The scalar measurement data was plotted with the measured VNA data for five states in order to highlight the quality of the scalar measurement. The comparison between

VNA and scalar measurement insertion loss data is shown in Fig. 4.24. Figure 4.24 shows a good agreement between the VNA and scalar data down to approximately 40 dB of insertion loss. The -40 dB magnitude of transmission corresponds to the 40 dB dynamic range of the scalar measurement system. The dynamic range is limited at the lower end of the frequency sweep by the poor isolation between the unshielded PLL circuit board and the detector. At the higher end of the frequency sweep the dynamic range is limited by the output power of the frequency synthesizer. Neither parameter was optimized in this design since a 40 dB dynamic range is a reasonable approximation to what is attainable in a single chip filter tuner implementation. The plots of Fig. 4.24 are the result of the scalar measurement hardware operating as the active measurement system for tuning and the VNA is only used to measure the final response.

4.2.4 Summary

In many cases, the exact relationship between the state of a tuning element of a filter and a resonator's resonance frequency are not precisely known. The uncertainty in resonance frequency may be attributed to long-term drift, temperature, or manufacturing process variation. A scalar measurement-based tuning algorithm for Chebyshev-type low-order filters has been presented to circumvent these problems during the tuning process. Analytical closed form solutions have been derived for the errors inherent to the algorithm. The predicted tuning behavior of the algorithm using a coupling matrix-based model has been verified by measured results, with good agreement between tuning behavior predicted by the model and the measured results. The tuning approach is intended for on-board tuning without requiring a VNA.

The presented approach does not purport to tune input or output couplings. It is therefore best suited for tuning filters with input and interresonator coupling variation that are prescribed at design time. The constant bandwidth filters described in Chapter 3 are examples of filters that exhibit prescribed bandwidth variation. The coupling matrix models generated using the design and modeling methods described in Chapter 3 can be used to analytically derive the tuning performance and predict the deterministic tuning error of the scalar single-frequency tuning algorithm presented in this chapter. With an accurate model of the tuning error, it is possible to create a feed-forward error correction to minimize the deterministic error present in the proposed tuning method.

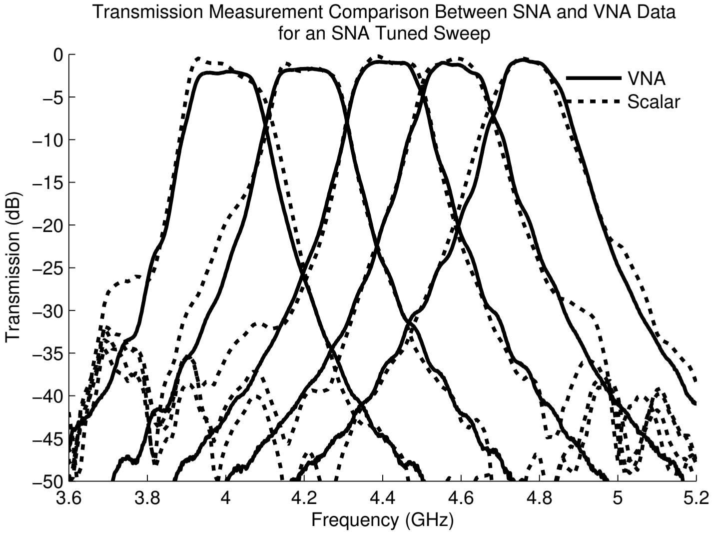

(a) VNA vs. scalar measurement insertion loss comparison

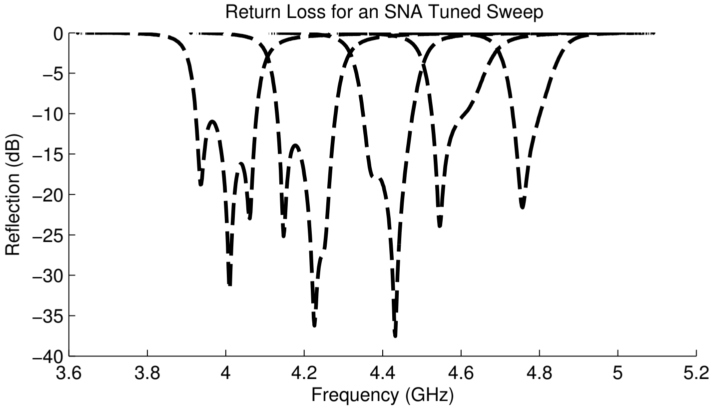

(b) Return loss of the states shown in Fig. 4.24a

Figure 4.24: Comparison between the VNA measurement and scalar measurement for demonstration of the scalar measurement hardware's measurement and tuning accuracy. The insertion loss comparison is shown in Fig. 4.24a. The return loss attained using the scalar measurement hardware for tuning is shown in Fig. 4.24b and is measured using the VNA.

Chapter 5

Piezoresistive Feedback for Position Sensing of CMOS-MEMS Variable Capacitors

5.1 Introduction

RF MEMS have been demonstrated as effective tuning elements for tunable filters, impedance matching networks, and phase shifters [1, 103]. RF MEMS reconfigurable elements have higher quality factor, linearity and power handling than competing technologies [1]. Switched capacitors, contact switches, capacitive switches and variable capacitors are several of the demonstrated types of RF MEMS reconfigurable elements.

Interest in MEMS variable capacitors in particular has waned in favor of MEMS switched capacitor banks due to reliability and controllability challenges of continuously variable MEMS capacitors. The preferred control mechanism for RF MEMS is electrostatic actuation due to its low power consumption. However, electrostatic actuation naturally exhibits a bistable response and is best suited as an actuation principle for switched capacitors. Switched capacitors require predictable performance in only two states resulting in simple control and requiring mechanical design for only two positions. The simplified control and mechanical design make switched capacitors easier to realize for reliability and control.

Nonetheless, significant research has been done on continuously tunable electrostatically actuated MEMS variable capacitors despite practical challenges. Research in continuous tuning of RF MEMS devices has been driven by applications that require fine resolution, such as tunable filters, where capacitance control down to 1 fF may be required [104].

Most reported tunable MEMS varactors have tuning ranges that are limited by the electrostatic pull-in phenomenon. It has been shown that in a simplified parallel plate variable capacitor model the force balance equation has an instability at $g = \frac{2}{3}g_0$ resulting in a collapse of the suspended plate at the pull-in voltage given in (5.1) where g_0 is the initial gap, A is the area of the plates, k is the spring constant, t_ϵ is the thickness of the dielectric and ϵ_r is the relative dielectric constant of the dielectric. Similarly, a force balance equation can be written to solve for the voltage necessary for the plate to release as given in (5.2). The pull-out voltage is generally lower than the pull-in voltage resulting in a hysteresis effect in the capacitance versus voltage curve. The hysteresis effect makes control of a variable capacitor beyond pull-in difficult.

$$V_{PI} = \sqrt{\frac{8k}{27\epsilon_0 A}\left(g_0 + \frac{t_\epsilon}{\epsilon_r}\right)} \tag{5.1}$$

$$V_{PO} = \sqrt{\frac{2kg_0t_\epsilon^2}{\epsilon_0\epsilon_r^2 A}} \tag{5.2}$$

Several methods have been proposed to extend the tuning range of tunable MEMS capacitors through mechanical design and control techniques [56,75]. One mechanical design method for the extension of the analog tuning range is the application of a piece-wise linear spring to extend the tuning range of the capacitance versus voltage characteristic (CV) [56,105]. In some cases, the piece-wise linear spring constant may result in multiple pull-in events and lead to a multi-step behavior [55,97]. However, each pull-in event also leads to hysteresis making the control of analog tunable MEMS devices difficult beyond pull-in instabilities.

The reliability and controllability of electrostatically actuated MEMS devices is further affected by dielectric charging effects that lead to an evolution of the capacitance versus voltage characteristic and have even been shown to lead to device failure in long term reliability testing [106]. The evolution of the capacitance versus voltage curves further compound the difficulty of controlling MEMS variable capacitors. MEMS capacitors have the distinction that their electrical behavior is determined by the mechanical position of the movable plates. The effects of both hysteresis and charging are manifested as a deflection of the mechanical structure. Therefore, it is proposed that if the position of the mechanical structure can be precisely controlled then the electrical characteristics will follow.

The aim of this work is to demonstrate an integrated sensing mechanism that is capable of detecting the effects of both hysteresis and dielectric charging in RF MEMS variable capacitors. Non-ideal effects, such as dielectric charging and hysteresis, result in mechanical deflection. Therefore, detecting plate position also enables the detection of hysteresis and dielectric charging. Furthermore, it has been demonstrated in the literature [107,108] that closed-loop position control can extend the stable range of electrostatic actuators beyond the pull-in point. Position control, therefore, has the potential to solve many of the fundamental problems in analog tunable RF MEMS variable capacitors. Integrated position sensing is a necessary first step to fully integrated position control.

5.2 Fabrication Process

The fabrication process used for this design employs a CMOS post-processing technique to release MEMS structures from the CMOS metal and polysilicon routing layers. The base CMOS process used here is a two-polysilicon four-metal layer 0.35 μm process as shown in Figure 5.1a. The 0.35 μm process was chosen because of its low cost and its capacity to support four planarized metal layers. At least four metal layers are required for the release of parallel plate MEMS structures using the University of Waterloo (UW) CMOS post-processing technique.

The four metal layers are composed of aluminum with silicon dioxide inter-metal dielectrics as shown in Fig. 5.1a. Interconnect between metal layers is accomplished using tungsten via plugs. In the UW CMOS-MEMS process the aluminum metal layers act as patterning, structural and release layers. The metal layers can also be used to route electrical signals through the MEMS structure for actuation and sensing.

The residual stress of the aluminum layer is tensile while the residual stress in the oxide layer is compressive. The metal and the oxide have coefficients of thermal expansion (CTE) that differ by an order of magnitude. The large difference in CTE makes lateral thermal actuators popular in other CMOS-MEMS processes such as the ASIMPS

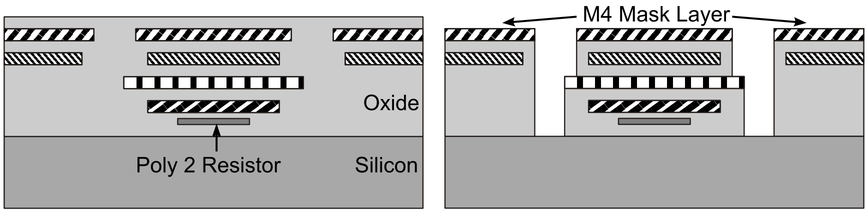

(a) Initial CMOS die (b) Oxide RIE

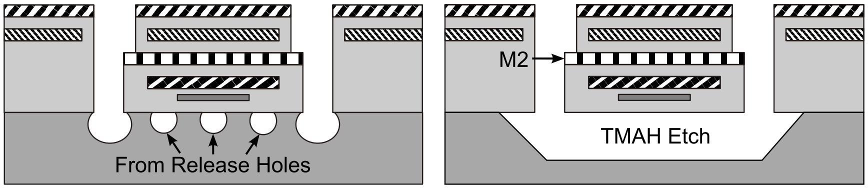

(c) Isotropic Si etch with RIE (d) TMAH anisotropic Si etch

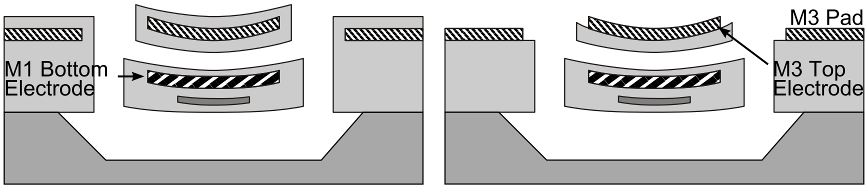

(e) PAN and H_2O_2 release (f) Final oxide etch

Figure 5.1: CMOS-MEMS process flow used in the fabrication of the CMOS-MEMS variable capacitor with integrated position sensing

process [109]. The differences in CTE are parasitic to this design and are beyond the scope of this work.

In addition to the four metal layers, the 0.35 μm process also offers two polysilicon layers. The first polysilicon layer is primarily intended for logic level (3.3 V) transistors, while the second polysilicon layer is used to define 5 V transistors. The two polysilicon layers can also be used to fabricate resistors and high capacitance density polysilicon-insulator-polysilicon capacitors. Only the second polysilicon layer (Poly2) is used in this design. The higher resistivity of the second polysilicon layer makes it better suited for strain sensing applications. A higher resistance strain sensing resistor reduces the current necessary for readout of the resistance bridge and reduces the power dissipation within the mechanical structure that can cause parasitic deflection.

The post-processing procedure used to fabricate the variable capacitors with position sensing is similar to the one used in [55] and is summarized in Fig. 5.1. The fabrication of this device uses the top metal layer (M4) as the masking layer, the second metal layer (M2) as the sacrificial layer, and the first (M1) and third (M3) metal layers as the bottom and top electrodes of the MEMS variable capacitor, respectively.

The fabrication process begins with loose die provided by a CMOS multi-project wafer or shuttle run as shown in Fig. 5.1a. The first post-processing step is a reactive ion etching (RIE) step using CF_4 and H_2 to expose the silicon substrate as shown in Fig. 5.1b. The M4 metal is used as a mask for the oxide etching step. M4 covers all structural metal by at least 1-2 µm such that structural layers do not have any metal exposed by the first processing step. The two hours of oxide etching step results in RIE grass formation that is removed using a one hour soak in EKC 265 at room temperature. After the removal of the RIE grass the result is shown in Fig. 5.1b. The third step is to etch the silicon substrate using 20 minutes of RIE using SF_6 to isotropically etch the substrate and enlarge the exposed surface area of the silicon substrate as shown in Fig. 5.1c. The increased surface area of the silicon substrate reduces the time required for the tetramethylammonium hydroxide (TMAH) wet etching step to achieve complete release. The TMAH wet etching step takes 90 minutes at 80 °C resulting in a structure resembling the one shown in Fig. 5.1d. TMAH also attacks aluminum and at this point the M4 aluminum masking layer and the M2 sacrificial aluminum layer are partially removed. The remainder of the mask and sacrificial metal layers are removed using a phosphoric-ascetic-nitric (PAN) acid solution for 40 minutes, followed by 40 minutes in hydrogen peroxide (H_2O_2) and another 40 minutes in PAN etch. All the metal etching steps were done at 60 °C yielding a structure as shown in Fig. 5.1e. All of the wet etching steps are done in sequence without permitting the dies to dry. After the final wet etching step, the dies are dried using a critical point dryer to prevent stiction and complete the release process. M4 is etched away during the metal release step and is not available for electrical contacts. Therefore, M3 is used as the top metal for wire bonds and electrical probing. The M3 pads are exposed using a final 30 minute oxide etching step that exposes M3 and permits the formation of electrical contacts.

5.3 Theory

The transduction principle for position sensing employed in this work is based on piezoresistance. The piezoresistive effect causes a change in resistance that is proportional to the change in length of a resistive material. The piezoresistive property of a material is characterized by its piezoresitive gauge factor G_f as shown in (5.3). The piezoresistive gauge factor relates the proportional change in resistance to the proportional change in length. The proportional change in length is known as the strain of a material and is represented by $\epsilon = \Delta L/L$.

$$G_f = \frac{\frac{\Delta R}{R}}{\frac{\Delta L}{L}} = \frac{1}{\epsilon}\frac{\Delta R}{R} \tag{5.3}$$

Traditionally, piezoresistors in strain gauge applications are realized using p-type crystalline silicon and have gauge factors around 100 [110]. In the CMOS-MEMS process the bulk silicon is used as a sacrificial layer and therefore cannot be integrated into the mechanical structure to realize a strain gauge. Another available material in the CMOS process with piezoresistive properties is polysilicon. Polysilicon is used in CMOS circuits for the gate electrode of field effect transistors and for the fabrication of resistors and polysilicon-insulator-polysilicon capacitors. Polysilicon appears next to the substrate in the CMOS-MEMS beam stack. Therefore the polysilicon layer can only be used for position sensing of structures composed of the bottom of the material stack. As a strain gauge, polysilicon has a reasonable gauge factor of about 20 [110].

The piezoresistive position sensing mechanism has been reported in the literature in sensor applications such as scanning probe microscopy [111], ultrasonic transducers [112] and micro-resonators [76]. In [112] piezoresistive feedback was found to be more area efficient than capacitive position transduction for MEMS-based ultrasonic transducers.

The readout of a piezoresistive strain gauge can be done using several methods. The three methods discussed here are the current-source method, the half-bridge and full-bridge configurations as shown in Fig. 5.2. The current-source method is essentially a two-wire resistance measurement such as the one done using a digital multimeter (DMM). A current source applies a current I_b as shown in Fig. 5.2a and the resistance is measured as a ratio of the output voltage V_o and I_b ($R_1 = V_o/I_b$). This measurement method lumps all resistance effects into the measurement. The effects of temperature on the resistance are measured in addition to the piezoresistive effect.

The half-bridge configuration is used to cancel temperature effects from a resistance measurement. Consider the half-bridge configuration shown in Fig. 5.2b. The output voltage of the half bridge is $V_{DD} \cdot R_1/(R_1 + R_2)$ where R_1 is the resistance of the strain

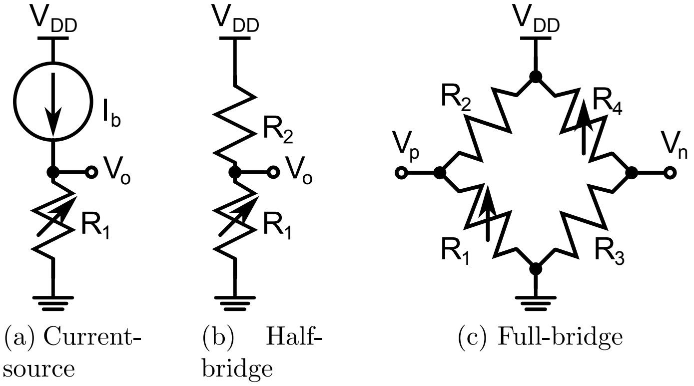

(a) Current-source (b) Half-bridge (c) Full-bridge

Figure 5.2: Current-source, half-bridge and full-bridge configurations for voltage read-out of a piezoresistive strain gauge

gauge or sense resistor and R_2 is the resistance of the reference resistor. If the reference resistor is selected to have a nominal resistance equal to the sense resistor then the temperature coefficient can be cancelled to the first order [111]. However, sensitivity due to the supply voltage is not improved. The sensitivity of the half-bridge circuit to a change in the sense resistance R_1 is shown in (5.4) where the nominal resistance of $R_1 = R_2 = R$ [111].

$$S_{R_1} = \frac{\delta}{\delta R_1}\left[\frac{R_1}{R_1 + R_2} V_{DD}\right] \approx \frac{1}{R} \cdot V_{DD} \tag{5.4}$$

A full-bridge configuration is shown in Fig. 5.2c. The full-bridge configuration has the added benefit of enhancing the supply noise rejection. Since the measurement is made as a differential signal across the two anti-parallel half-bridges the supply voltage appears as a common-mode signal and is effectively cancelled. In addition, the anti-parallel configuration of the two bridges results in a differential signal level from the full-bridge that is double that of a half-bridge. The sensitivity of the full-bridge circuit to change in the two sense resistors R_1 and R_3 is given in (5.5) [111] where the nominal resistance of all the resistors in the bridge is assumed to be equal to R.

$$\begin{aligned} S_{R_{1,4}} &= \frac{\delta}{\delta R_1}\left[\left(\frac{R_1}{R_1 + R_2} + \frac{R_4}{R_3 + R_4}\right) \cdot V_{DD}\right] \\ &\approx \frac{2}{R} \cdot V_{DD} \end{aligned} \tag{5.5}$$

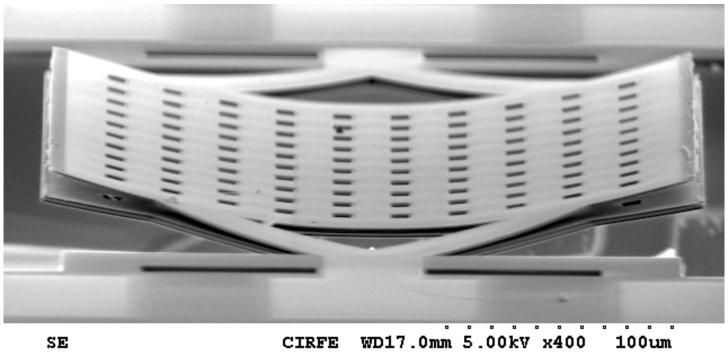

Figure 5.3: SEM picture of the fabricated device after complete release process

The capital benefit of the CMOS-MEMS process is the ability to monolithically integrate the sensing circuit and MEMS device on a single die. Amplification of resistance bridges is done using an instrumentation amplifier due to the instrumentation amplifier's high input impedance and negligible read error due to loading effects. An instrumentation amplifier can easily be integrated in CMOS using three operational amplifiers. In an on-chip circuit, the full-bridge configuration is the preferred voltage readout configuration for its common mode noise rejection.

5.4 Design

The polysilicon layer is found at the bottom of the CMOS-MEMS material stack-up as shown in Fig. 5.1a. In order to use the polysilicon layer for position sensing, the bottom of the CMOS-MEMS material stack needs to be included in the structure whose position is being sensed. For this reason, the curled plate design from [55] was chosen as a basis for this work with two key design improvements; the use of an isolated DC actuation electrode and the integration of a position sensing piezoresistor.

An SEM picture of the fabricated device is shown in Fig. 5.3 and the layout of the top and bottom plates is shown in Fig. 5.4. The near pads in Fig. 5.3 are the RF pads while the far pads are for DC biasing and piezoresistor based position sensing (left and right pads in Fig. 5.4). The upward curl of both the top and bottom plates is caused by the residual stresses in the metal and oxide layers. The residual stress establishes the up-state, zero-bias capacitance as shown in Fig. 5.5a. The application of a DC voltage between the top and bottom plates establishes an electrostatic field that applies a force that is

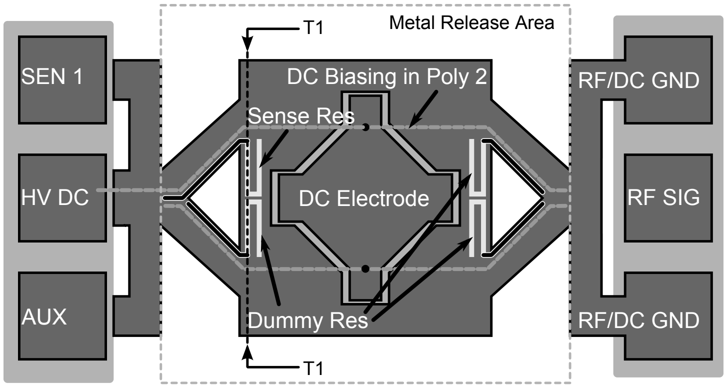

(a) Variable capacitor bottom plate

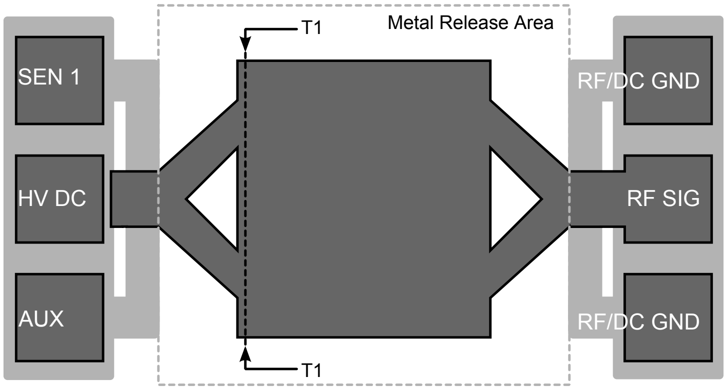

(b) Variable capacitor top plate

Figure 5.4: The layouts of the top and bottom plates of the parallel plate variable capacitor with integrated position sensing. The bottom plate includes a sense resistor and dedicated DC actuation pad for simplified biasing.

proportional to $\frac{1}{2}CV^2/g$ [113]. The electrostatic force brings the two plates together causing them both to deform as shown in Fig. 5.5b. The deflection of the bottom plate also deforms the strain sensing resistor that is integrated into the composite structure.

The variable capacitor is connected to ground-signal-ground (GSG) co-planar probe pads with 150 μm pad pitch as show in Fig. 5.4. The bottom plate of the variable capacitor is connected to the RF ground pads while the top plate is connected to the RF signal pad as shown in Fig. 5.4a and Fig 5.4b, respectively. The modifications to the design from [55] lie in the configuration of the bottom plate as shown in [114]. The bottom plate area is divided into two electrically isolated segments—one for DC bias and the other for RF ground. One of the target applications for integrated CMOS-MEMS variable capacitors is for CMOS integrated reconfigurable RF components. Biasing circuits can consume

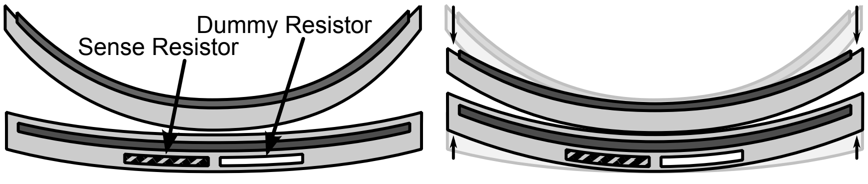

(a) Initial device deflection (b) Actuated device

Figure 5.5: The deflection of the top and bottom plates during actuation. Both the top and bottom plates deflect with an applied voltage. The bottom plate contains the piezoresistor and registers deflection of the bottom plate as a change in resistance.

appreciable die area and may require off-chip components. This design incorporates a separate actuation pad for the isolation of the DC biasing and RF ports in order to simplify biasing requirements. The biasing electrode is integrated into the bottom plate since there are additional isolated electrical routing layers in the bottom plate (M1 and Poly1/Poly2). The Poly2 layer is used to route the DC bias to the actuation electrode in the bottom plate. The resistance of the polysilicon layer does not affect electrostatic biasing since there is no DC current at steady state. A highly resistive bias also reduces the leakage of RF energy through the DC biasing electrode.

The sense resistor is integrated into the bottom plate adjacent to the plane of symmetry. The length is set to achieve a resistance of $3.3\,\mathrm{k\Omega}$ and limit the current consumption to $0.5\,\mathrm{mA}$ per half-bridge at $3.3\,\mathrm{V}$. The test chips fabricated for the characterization of piezoresistive feedback for RF MEMS control were area limited by the number of pads. Due to pad limitations, only a single sense resistor could have a dedicated bonding pad. The three remaining resistors are used as dummy devices to maintain device symmetry for mechanical purposes. Since only a single sense resistor is available for measurement, the full-bridge configuration for sensing could not be implemented. In this design we are limited to using the current source-based readout method.

The common connection of the sense resistor is tied to the RF ground that composes the majority of the bottom plate area and is connected to the ground of the RF GSG pads. Parasitic resistance is minimized by routing to the polysilicon sense resistors using the first metal layer in order to maximize the relative change in resistance. Signal routing to the DC electrode is done by routing using the Poly2 layer underneath the first metal layer. The integration of the DC actuation electrode results in a substantially lower capacitance since a large area of the bottom plate is consumed by the DC electrode. The

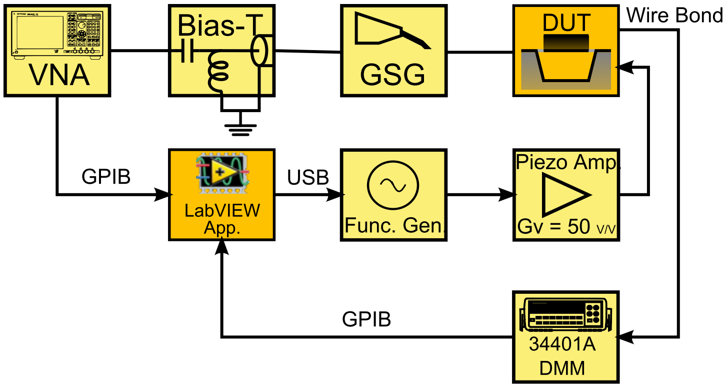

Figure 5.6: Block diagram of the measurement setup

biasing simplicity achieved using an isolated DC electrode plate is traded-off against a reduction in capacitance density.

5.4.1 Measurement Setup

Capacitance versus voltage (CV) and resistance versus voltage (RV) measurements were performed using an automated test setup on a Cascade vibration isolated wafer probe station. The MEMS die was mounted using epoxy onto a two layer gold plated printed circuit board. The DC bias pad and sense resistor read-out pad were wire bonded to two traces on the PCB that led to two soldered wire connections that were connected to a Trek PZD350 high-voltage amplifier and Agilent 34401A digital multimeter (DMM) as shown in Fig. 5.7. The instrumentation setup is shown in Fig. 5.6. The RF GSG pads were probed using a Cascade ACP-40 GSG probe that was connected to an Agilent 8722ES vector network analyzer (VNA) through a bias-T. The bias-T set the DC bias on the RF ground and signal lines to 0 V DC. The RF ground and signal were DC shorted together through the RF choke of the bias-T. The common connection for RF ground, high-voltage ground and the sense resistor is made at the RF choke of the bias-T. The high-voltage amplifier was driven by an Agilent function generator that acted as a digital to analog converter for the LabVIEW application. The VNA and DMM were interfaced to the PC running the LabVIEW application using GPIB through a GPIB-to-USB adapter. The function generator was directly interfaced to the PC using a USB interface.

In order to collect the RF capacitance of the variable capacitor as quickly as possible, the VNA was set to operate in continuous wave mode at 5 GHz with only 11 points

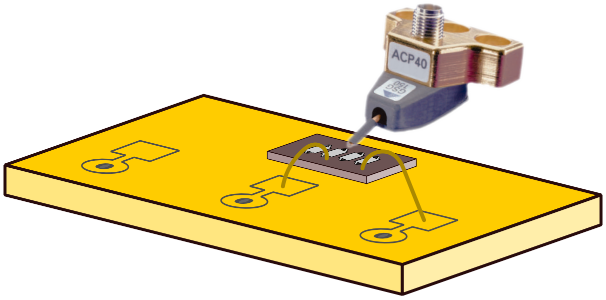

Figure 5.7: Illustration of the probing configuration with the test chip mounted on a gold plated PCB and probed using Cascade ACP-40 RF GSG probes.

captured per sweep. The VNA was calibrated using a one-port SOL calibration on a Cascade impedance standard substrate. The capacitance was extracted by first converting the S-parameters to Z-parameters and then calculating the capacitance using (5.6).

$$C = -\frac{1}{2\pi \cdot 5 \times 10^9 \cdot \Im\{Z_{11}\}} \tag{5.6}$$

The offset and gain of the amplifier were calibrated at output voltage set points of 0 V and 100 V, respectively. The gain of the Trek amplifier was set using a potentiometer while the offset was corrected in software using the LabVIEW application. The gain of the amplifier was set to 50 V/V in order to avoid an output voltage discontinuity caused by the function generator when switching to a voltage above 2 V.

At each voltage step of the tested waveform a sequence of measurements was made: first, the voltage was set, then the VNA data was captured and then the resistance measurement was made. The VNA data at each voltage step was stored in a touchstone file while the resistance data for each piecewise linear ramp was stored in a comma separated values (CSV) file. Each voltage step took 1.4 s to measure, format and store all the data. Each of the waveforms tested was run for 50 periods each in sequence. The positive triangle waveform was applied first, immediately followed by the bipolar waveform and finally the negative triangle waveform.

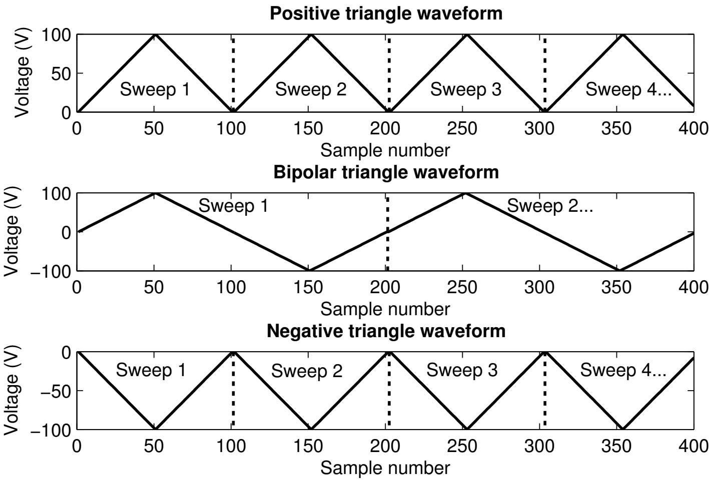

Figure 5.8: Three test waveforms. The top waveform is a positive triangle waveform from 0 V to 100 V, the second waveform is a bipolar triangle waveform from -100 V to 100 V and the third waveform is a negative triangle waveform from 0 V to -100 V. A sample is taken every 2 V in all cases. Each sweep (period) of the positive and negative waveforms is 101 points, while each sweep of the bipolar waveform is 201 points.

5.5 Measurement Results

The three test waveforms are shown in Fig. 5.8. Testing of all three waveforms was performed using 2 V steps. The first waveform tested was a positive triangle waveform with the voltage ramped between 0 V and 100 V. The second test was a bi-polar triangle waveform ramped between -100 V and +100 V. Finally, the negative triangle waveform was tested between 0 V and -100 V. Fig. 5.8 indicates the sweep number of each period of a waveform as well as the sample number. The evolution of the capacitance versus voltage for each sweep are logged as well as the corresponding sense resistance per sample. Each sweep number identifies a complete waveform period.

The thermal coefficient of resistance for the polysilicon resistors in this process had an impact on the absolute value of resistance that was read using the direct measurement with a DMM. The DMM measures the absolute value of resistance and not the relative value such as the full-bridge. Therefore, the resistance data was normalized to the peak resistance read during a sweep to reduce the effects of temperature drift on the presented data. The peak resistance corresponds to the capacitor in its up-most relaxed state. In an on-chip implementation, the half-bridge or full-bridge read-out could accomplish the same effect. The resistance data is presented as a percentage change in resistance from the maximum read during a sweep as given in (5.7).

$$R_{norm} = \left(\frac{R}{\max(R)} - 1 \right) \cdot 100 \tag{5.7}$$

In order to eliminate the capacitance drift from the data, the capacitance values are also presented as normalized values. The data for the three waveforms was collected overnight for 8 hours. The calibration of the VNA drifts somewhat over this time frame. Therefore, the capacitance is normalized to the minimum capacitance. The nominal minimum capacitance is 0.845 pF. In this case, the minimum (up-state) capacitance is normalized to 1 using the expression given in (5.8).

$$C_{norm} = \frac{C_{meas}}{\min(C)} \tag{5.8}$$

The effects of hysteresis and dielectric charging were clearly detectable using the piezoresistive feedback mechanism. First, we present the results for the detection of dielectric charging and then we present the results for the detection of hysteresis and electrostatic pull-in discontinuities.

5.5.1 Detection and Tracking of Dielectric Charging

The evolution of the capacitance versus voltage (CV) and resistance versus voltage (RV) characteristics for the uni-polar positive triangle waveform is shown in Fig. 5.9. Three characteristic sweeps are shown for the second, ninth and fiftieth sweeps of the positive voltage waveform. The hysteresis data is not shown in order to reduce the clutter in the plot. Only the data collected for the positive ramp is shown—i.e., for the first half of the positive triangle waveform period as shown in Fig. 5.8. The effects of dielectric charging are manifested as the capacitance versus voltage curve shifting in the positive voltage direction with each subsequent sweep. The shift of the curve is observed in both the CV and RV curves shown in Fig. 5.9a and Fig. 5.9b. No attempt was made to optimize this device for dielectric charging and the materials are from a standard CMOS process. The measured charging effects are substantial. The CV characteristic shifts up to a point where the charging effect appears to saturate—in this case, between 40 V and 45 V. The

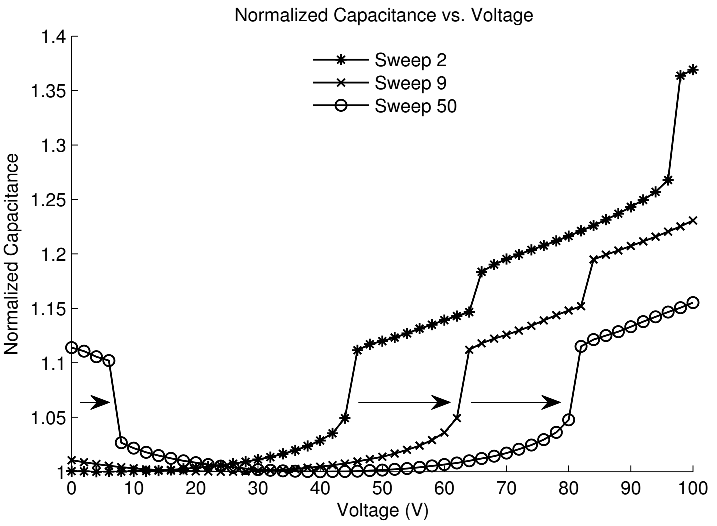

(a) Capacitance versus voltage evolution

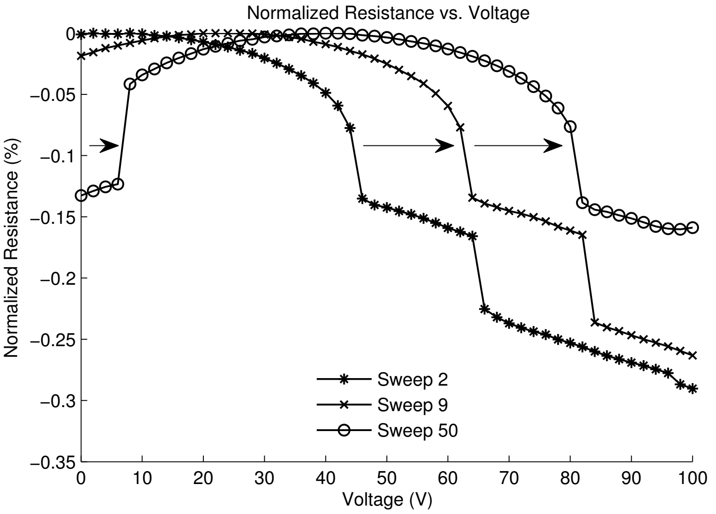

(b) Resistance versus voltage evolution

Figure 5.9: The evolution of the capacitance versus voltage and resistance versus voltage characteristics for a positive triangle waveform excitation with the voltage ramped between 0 V and 100 V. Each sweep takes, on average, 141 s. Therefore, sweep 2 is the data collected during testing between 141 s and 242 s into the test.

data for the up-state voltage using the sense resistor closely follows the up-state voltage measured using the capacitance data.

The minimum capacitance occurs when there is maximum separation between the top and bottom plates. In traditional single movable plate variable capacitors the point of

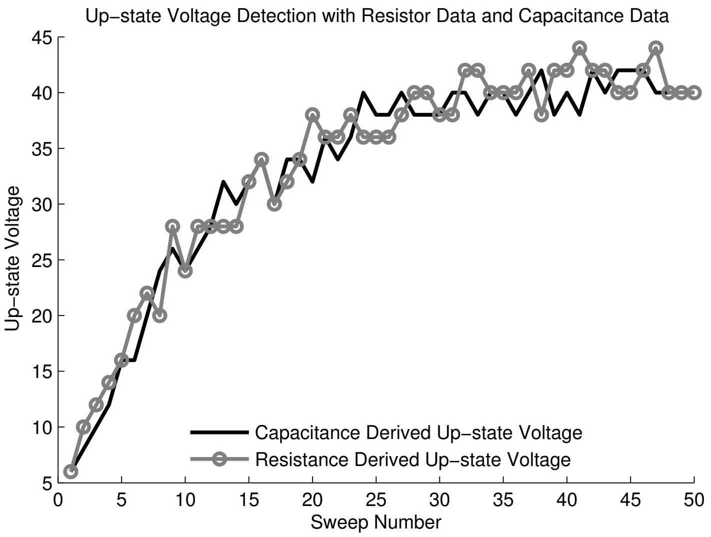

Figure 5.10: The up-state voltage versus sweep number as determined by the minimum capacitance and maximum resistance for each sweep of the positive triangle waveform.

minimum capacitance is referred to as the up-state capacitance. The applied voltage that results in the up-state capacitance moves along the voltage axis as the CV curve shifts due to charging. The voltage that corresponds to the up-state capacitance is referred to here as the up-state voltage. With a positive triangular voltage waveform, the up-state voltage shifts in the positive voltage direction with each subsequent sweep until it saturates at a voltage between 40 V and 45 V.

The up-state voltage versus sweep number is shown in Fig. 5.10 for the positive triangle waveform. The up-state voltage is extracted from both the strain sensor resistance data and the capacitance from the measured scattering parameters. The up-state would correspond to the maximum of resistance shown in Fig. 5.9b and the minimum of capacitance Fig. 5.9a. Fig. 5.10 plots the voltage required for minimum capacitance and maximum sense resistance for each waveform period with good agreement between both. The data shown in Fig. 5.10 appears noisy since it is difficult to find the minimum of curves that flat near the minimum in the presence of noise.

The bipolar measurement was performed by actuating the device with a ramp between -100 V up to 100 V and back to -100 V for 50 periods in 2 V increments. The duration of a bipolar period, therefore, is twice as long. The bipolar test commenced immediately following the positive actuation sweep and the up-state voltage already having been shifted.

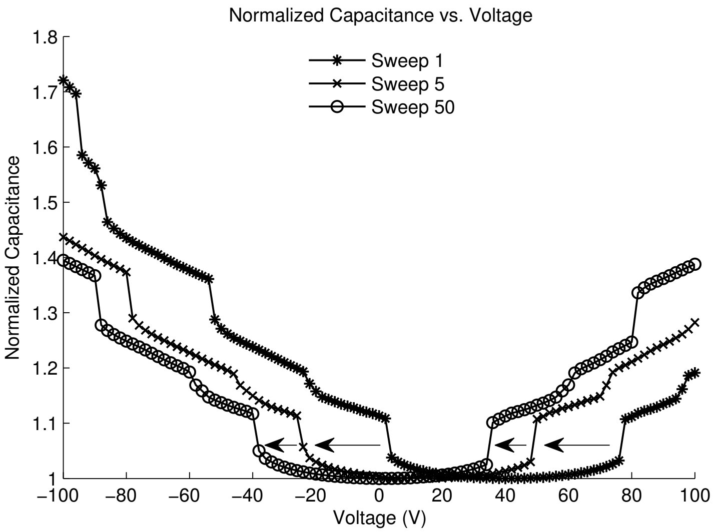

Figure 5.11: The evolution of the capacitance versus voltage characteristic with a bipolar triangle waveform with voltage ramped between -100 V and 100 V. Each sweep takes 282 s for 202 points.

The evolution of the CV curve for the bipolar triangle waveform is shown in Fig. 5.11. Although the positive triangle waveform actuation shifted the CV curve significantly in the positive actuation direction, the switch to a bipolar actuation waveform acts to shift the up-state capacitance of the CV curve back towards 0 V as shown in Fig. 5.11. After the 50th sweep of the bipolar waveform the charging effect of the positive triangular waveform is nearly eliminated as shown in Fig. 5.12.

Finally, the triangle waveform tests are completed with the test of a negative waveform with ramps between 0 V and -100 V. The application of a negative bias results in the up-state voltage shifting in the negative voltage direction. The negative triangle waveform appears to progress in a slower fashion than the positive waveform in when comparing Fig. 5.10 and Fig. 5.13. The evolution of the CV curve under a negative triangle waveform is shown in Fig. 5.14.

5.5.2 Detection of Hysteresis Events

Operating an electrostatic MEMS variable capacitor beyond its initial pull-in has the added complexity of requiring the control scheme to deal with hysteresis of the electrostatic pull-in discontinuities. Devices that exhibit multi-step behavior are therefore par-

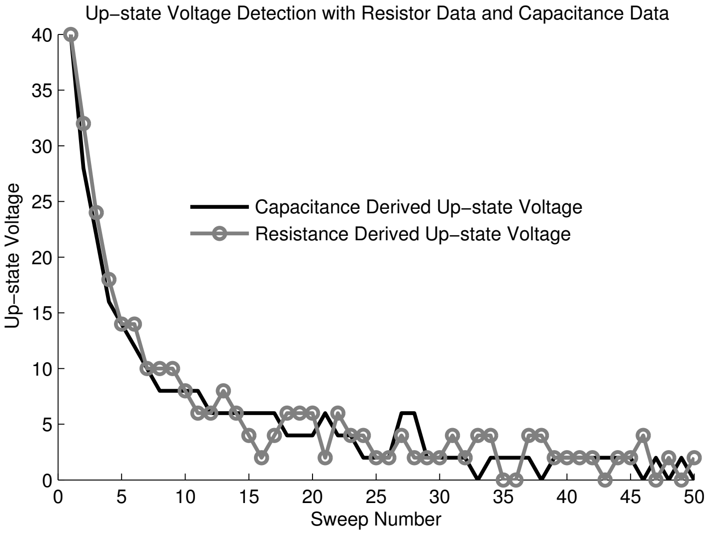

Figure 5.12: The up-state voltage versus sweep number for the bipolar voltage waveform showing the elimination of the up-state voltage shift caused by the positive triangle waveform.

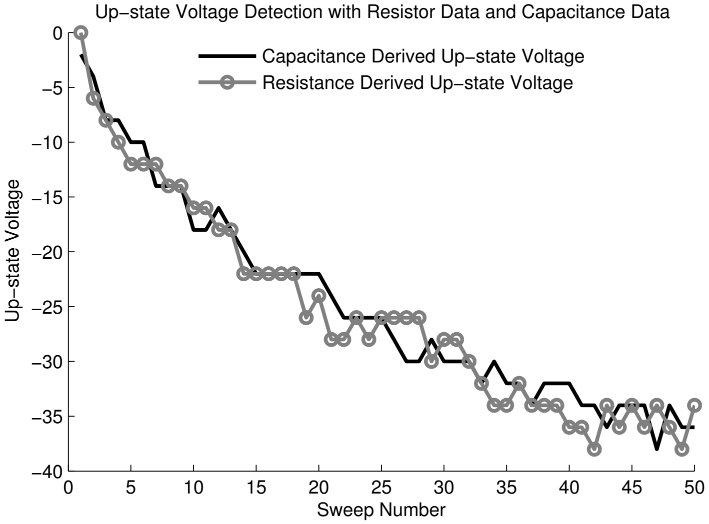

Figure 5.13: The up-state voltage versus sweep number as determined by the minimum capacitance and maximum resistance for the negative triangle waveform.

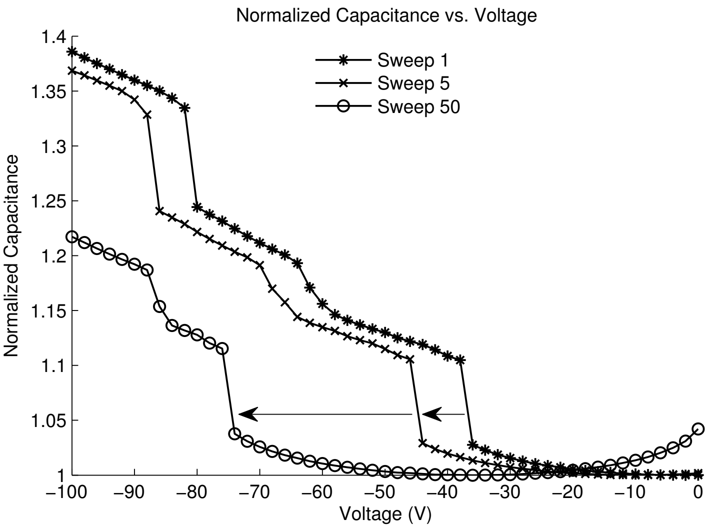

Figure 5.14: The evolution of the capacitance versus voltage characteristic with a negative triangle waveform with voltage ramped between 0 V and -100 V.

ticularly challenging to control since they have multiple hysteresis regions. The CMOS-MEMS variable capacitor presented here has a particularly complex capacitance versus voltage characteristic with multiple discontinuities. Each discontinuity results in a degree of hysteresis imposed by the step change in capacitance as discussed above. In this section we investigate the ability of the sense resistor to distinguish hysteresis events resulting from pull-in discontinuities.

The hysteresis curves for capacitance versus voltage and resistance versus voltage for a bipolar triangle waveform are shown in Fig. 5.15. The data shown in Fig. 5.15 is from sweep number 50 of the bipolar waveform test. By sweep 50, the residual effects of dielectric charging caused by the positive triangle waveform have settled out. Therefore, the up-state capacitance voltage in Fig. 5.15 is near zero. The discontinuities in both the resistance and capacitance curves match up precisely within the 2 V voltage resolution. As a result, it can be concluded that the pull-in events can be detected through position sensing of the bottom plate over the hysteresis boundaries.

5.5.3 Evaluation for Closed Loop Control

Evaluation of the sensing mechanism for closed-loop control was performed by plotting a scatter plot of capacitance versus voltage and capacitance versus resistance for the data

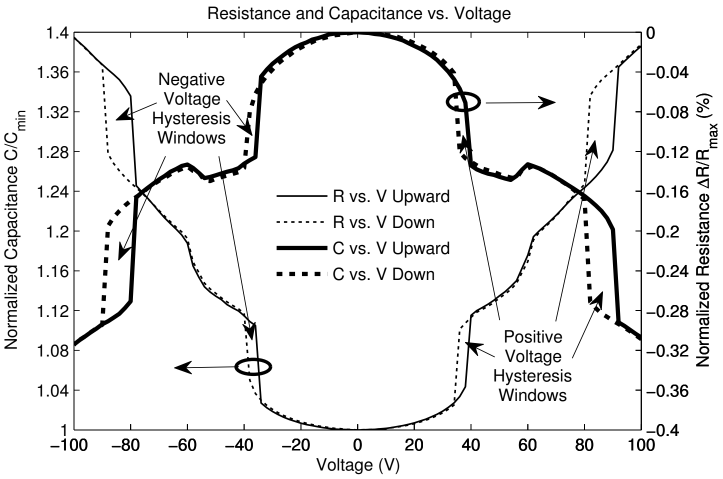

Figure 5.15: Hysteresis curves for resistance and capacitance versus actuation voltage are shown. Thicker lines are used to plot the normalized resistance while the thinner lines are used for capacitance. The solid lines are for increasing voltage sweeps while the dashed lines are used for decreasing voltage sweeps.

collected during the bipolar waveform test immediately following the positive triangle waveform test. Fifty bipolar actuation sweeps were collected with 202 (R,C) points per sweep represented in Figs. 5.16 and 5.17. The data shown in Fig. 5.16 is the same data shown in Fig. 5.11 with all 50 waveforms represented. A total of over 10 000 points are shown in each plot with data collected over nearly 4 hours.

In Fig. 5.16, there are continuous bands of potential capacitance values for a given voltage due to hysteresis and dielectric charging effects. Re-plotting the same data with respect to resistance results in Fig. 5.17. In Fig. 5.17 there are 3 distinct lines on the scatter plot that correspond to operating regions with stable position using fixed voltage control. The gaps are caused by areas of capacitance and resistance that are not reachable using voltage control. Only a small region of the domain, circled in Fig. 5.17, results in multiple capacitance values for a measured resistance. In comparison to Fig. 5.16, the continuous bands of capacitance versus voltage have been reduced to narrow lines of capacitance versus resistance, thus, significantly improving the capacitance uncertainty.

The multiple capacitance values per resistance circled in Fig. 5.17 have been traced to the mechanical design resulting in multiple stable states for a given voltage. Consider Fig. 5.18 schematically depicting the cross-section of the two curled plates during actuation. The sense resistor is placed on the left half of the structure as shown in Fig. 5.18.

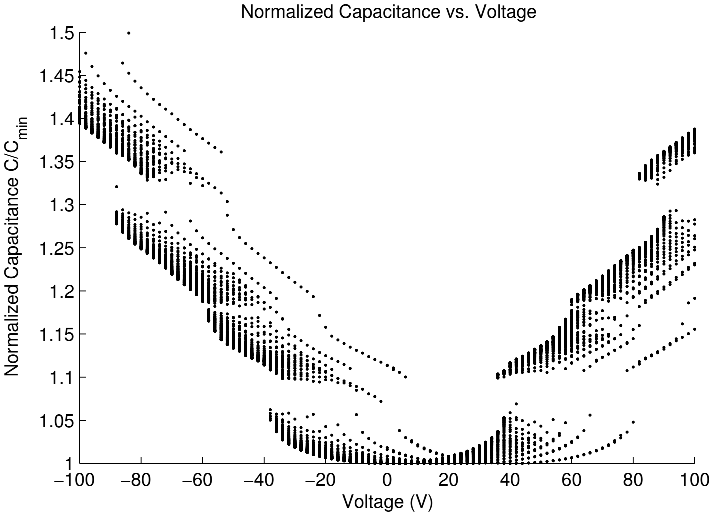

Figure 5.16: The scatter plot of capacitance for the collected data points of capacitance versus voltage for the bipolar actuation waveform immediately following a positive triangle waveform. There are many potential capacitance values for a given voltage set point. This figure indicates that controlling a variable capacitor using fixed voltage control has significant capacitance uncertainty when taking into account hysteresis and dielectric charging.

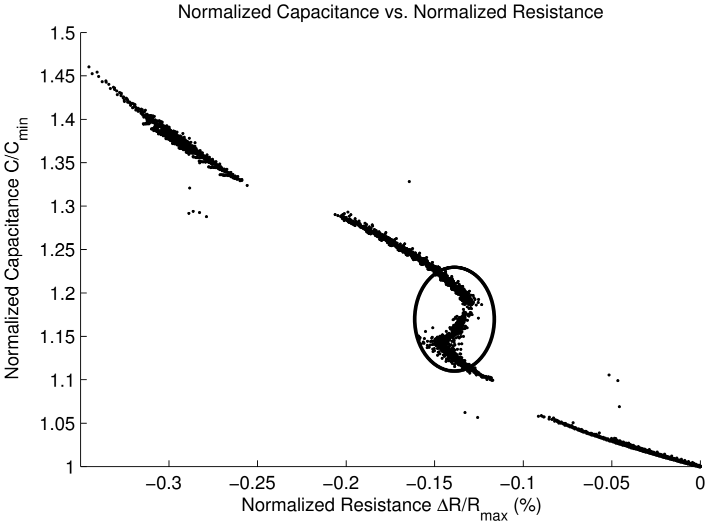

Figure 5.17: The scatter plot of capacitance versus resistance for the bipolar actuation waveform. The capacitance vs. resistance points form straight lines. There are a finite number of capacitance points with respect to resistance.

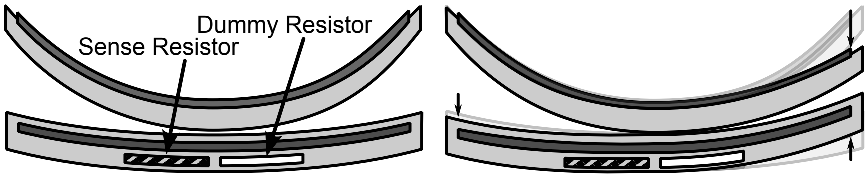

(a) Initial position (b) One side first

Figure 5.18: Capacitor actuation schematic showing the effect on the deflection of the resistor if one side actuates before the other. The sense resistor is located on the left half of the capacitor.

The sensor is placed on only one half of the structure since a symmetric mechanical response was initially expected. Viewing the actuation of the device using a microscope during testing, it was discovered that in some instances one half of the structure would actuate before the other. Since the sense resistor is installed in only one half of the structure, only the strain of that half results in a sensed resistance change. This discrepancy also registers in the scatter plot data of Fig. 5.17 as an array of circled points where the resistance-based control law would fail. Further increase of the bias voltage returns the capacitance to a function of resistance.

Still, despite the uncertainty in the circled region of Fig. 5.17, the capacitance versus resistance shows a substantial improvement in precisely determining the capacitance compared to voltage control as shown in Fig. 5.16.

5.6 Summary

A position sensing scheme for the control of CMOS-MEMS variable capacitors has been demonstrated in a commercial CMOS process with MEMS post-processing. The results demonstrate the potential for closed-loop control of capacitor position to mitigate hysteresis and charging effects in CMOS-MEMS capacitors. The sensing scheme promises to reduce the uncertainty in capacitance when using a position control scheme based on piezoresistive feedback despite the charging and hysteresis effects. Piezoresistive feedback has the advantage of easy integration with on-chip electronics and no interference with the RF signal since the measurement is made at DC.

Chapter 6

Conclusion

The primary contributions of this research and recommendations for future study are summarized in the following sections.

6.1 Contributions

The primary contributions of this research are as follows:

- A coupling matrix based design technique for tunable filters with controlled bandwidth and return loss across the tuning range has been developed. The proposed technique is implementation technology independent and is capable of predicting the filter response across the tuning range for filters with synchronous tuning. Two-pole and three-pole tunable suspended substrate filters with novel inter-resonator couplings and compensated resonators for synchronous capacitance tuning are demonstrated using the proposed design technique.

- Novel scalar transmission measurement based tuning algorithms using Hilbert transform derived group delay and single-frequency magnitude response have been developed. The two approaches are well suited for low-order integrated filter tuning. The single-frequency tuning algorithm was modeled using coupling matrix techniques with error bounds determined analytically from the theoretical model. The tuning algorithm was implemented into a fully automated tuning system with good agreement between predicted results and measured automated tuning performance.

- A position sensing scheme for CMOS-MEMS variable capacitors was demonstrated with a capability to detect absolute plate position in the presence of both hysteresis and dielectric charging effects. The correlation of capacitance and piezoresistive sensor signal was demonstrably better than voltage control. The capacitance can therefore be regulated by monitoring the sense resistance. Position sensing resulted in a substantial improvement in tuning accuracy compared to open loop voltage control. The CMOS MEMS variable capacitors were studied for their ability to tune on-chip filters.

6.2 List of Publications

The following is a list of academic publications relating to this thesis.

Journal Publications

N. Zahirovic, R.R. Mansour, and M. Yu, "Scalar measurement-based algorithm for automated filter tuning of integrated Chebyshev tunable filters," *IEEE Trans. Microwave Theory Tech.*, vol. 58 no. 12 pp. 3749-3759, Dec. 2010. [115]

N. Zahirovic, R.R. Mansour, and M. Yu, "Piezoresistive position sensing for the detection of hysteresis and dielectric charging in CMOS-MEMS variable capacitors," *IEEE Trans. Microwave Theory Tech.*, vol. 58 no. 12 pp. 3961-3970, Dec. 2010. [116]

S. Fouladi, F. Domingue, **N. Zahirovic** and R. R. Mansour, "Distributed MEMS tunable impedance-matching network based on suspended slow-wave structure fabricated in a standard CMOS technology," *IEEE Trans Microwave Theory and Tech.*, vol. 58 no. 4 pp. 1056-1064, March 2010. [117]

N. Zahirovic, S. Fouladi, R. R. Mansour, and M. Yu, "The design and modeling of tunable filters for constant bandwidth using coupling matrix techniques." (Pending)

Conference Publications

N. Zahirovic, S. Fouladi, R.R. Mansour, and M. Yu, "Tunable suspended substrate stripline filters with constant bandwidth," *2011 IEEE MTT-S Int. Microwave Symp. Dig.* Jun. 2011.

N. Zahirovic, R.R. Mansour, and M. Yu, “A MEMS variable capacitor with piezoresistive position sensing fabricated in a standard 0.35 m CMOS process,” *2010 IEEE MTT-S Int. Microwave Symp. Dig.* pp. 1154-1157, Jun. 2010. [114]

N. Zahirovic, R.R. Mansour, and M. Yu, “A three-step high-Q variable MEMS capacitor with low actuation voltage,” *2009 European Microwave Conference* pp. 1136-1139, Oct. 2009. [97]

N. Zahirovic and R. R. Mansour, “Sequential tuning of coupled resonator filters using Hilbert transform derived relative group delay,” *2008 IEEE MTT-S Int. Microwave Symp. Dig.* pp. 739-742, Jun. 2008. [74]

6.3 Future Work

The proposed future work in the three main contribution areas is as follows:

- The coupling matrix based tunable filter design method may be extended for controlled coupling variation of cross-coupled filters. Further inter-resonator coupling structures may be developed that maintain constant bandwidth in other resonator technologies such as evanescent mode cavity filters and dielectric resonator filters.
- The automated scalar tuning measurement technique for inter-resonator coupling control may be extended to enable closed loop tuning of variable bandwidth filters. The tuning error of the scalar transmission tuning approach may be corrected by applying a model-predicted correction factor based on tuning hop size or measuring the error and re-tuning with an error corrected target frequency.
- The position sensing scheme may be integrated with a closed-loop controller to create a regulated capacitance network. The linearity performance as a result of self actuation may be substantially improved since a controller with sufficient bandwidth may act to maintain plate position in presence of the self-actuation by the RF signal. The performance over temperature may also be improved with a balanced sensor feedback.

APPENDICES

Appendix A

UW MEMS Process

The UW MEMS process is a 7 mask process used for the design of high quality factor RF MEMS devices. The process supports three metal layers and one released structural layer. The first metal layer is chromium and is used as a resistive layer for the biasing of electrostatic MEMS. The second metal layer is gold for coplanar RF circuits and finally the structural MEMS layer is a second layer of gold.

The simplified process for fabricating the three-step capacitor is outline in Fig. A.1. The process begins with a bare polished alumina wafer which is cleaned using an RCA cleaning solution. The first mask step is to pattern a 50 nm layer of chromium to define the resistive bias lines for the MEMS devices. The next step is to deposit and pattern a 0.5 μm layer of silicon nitride to act as an insulator between the bias lines and the first gold layer. The first gold layer is then molded using electroplating to a thickness of 1 μm followed by the deposition and patterning of a second layer of 0.5 μm silicon nitride to act as a dielectric between the first and second gold. A 2.5 μm sacrificial layer of polyimide is then spin-coated and the anchor mask is used to define contacts between the two gold layers. The sacrificial layer is then patterned by the dimple mask to create indentations that will create topological features in the second gold layer through conformal deposition. The second gold is deposited and patterns the structural gold layer by electroplating to a thickness of 1.25 μm. This layer is released in the final step by removing the polyimide using an oxygen plasma in an reactive ion etcher (RIE) chamber.

Before the final release the devices are annealed at 360 °C for 3 hours to reduce the residual stress in the second gold structural layer. This residual stress causes cantilevers to deflect out of plane and significantly increases the actuation voltage. The pull-in

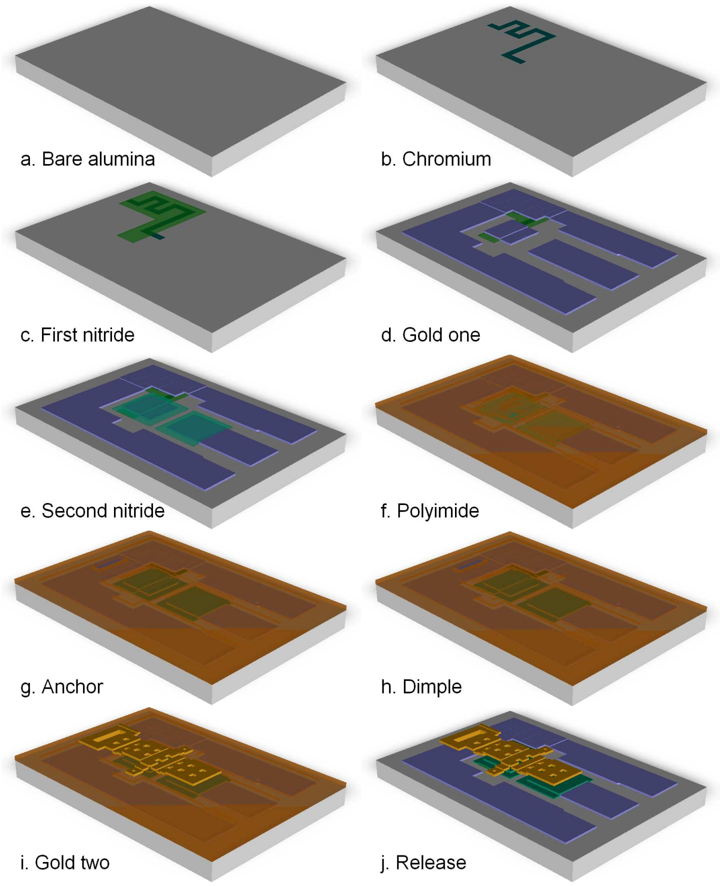

a. Bare alumina
b. Chromium
c. First nitride
d. Gold one
e. Second nitride
f. Polyimide
g. Anchor
h. Dimple
i. Gold two
j. Release

Figure A.1: Layout dimensions are 580 μm by 400 μm

voltage of the three-step capacitor before annealing is in excess of 75 V and drops to below 12 V after the annealing step.

Glossary

log detector
is a component that provides an output voltage that is proportional to the input power level in dB scale.

paraelectric
is a material whose dielectric constant varies with the applied electric field.

piezoelectric
is a solid material in which a charge accumulates in response to an applied mechanical stress and conversely an applied mechanical stress results in charge accumulation.

Acronyms

BST
barium strontium titanate–a paraelectric material ($Ba_{1-x}Sr_xTiO_3$) with good properties at microwave frequencies.

CIRFE
Centre for Integrated RF Engineering.

CMOS
complementary metal-oxide-semiconductor.

CMOS MEMS
CMOS MEMS.

CPW
co-planar waveguide.

EM
electro magnetic.

FPGA
field programmable gate array.

GPIB
general purpose interface bus.

GUI
graphical user interface.

HGD
Hilbert transform derived relative group delay.

HTS
high temperature superconductor—a material that becomes superconducting (exhibits zero electrical resistance) at a temperature above 30 K.

IIP3
input third order intercept point.

LTCC
low temperature co-fired ceramic.

MEMS

micro-electro-mechanical system.

MIM

metal-insulator-metal—a parallel plate capacitor configuration where two metals are separated by an insulating layer.

PCB

printed circuit board.

Q

quality factor.

RF

radio frequency.

RF MEMS

radio frequency micro-electro-mechanical systems.

RIE

reactive ion etcher.

SNA

scalar network analyzer.

SRF

self resonance frequency.

TMAH

tetramethylammonium hydroxide—a clear liquid often used as an anisotropic etchant of silicon or as a solvent for the development of photoresist.

TSMC

Taiwanese Semiconductor Manufacturing Company.

VNA

vector network analyzer.

References

[1] G. Rebeiz, K. Entesari, I. Reines, S.-J. Park, M. El-Tanani, A. Grichener, and A. Brown, "Tuning in to RF MEMS," *IEEE Microw. Mag.*, vol. 10, no. 6, pp. 55 –72, Oct. 2009, doi: 10.1109/MMM.2009.933592.

[2] R. Mansour, "High-q tunable dielectric resonator filters," *IEEE Microw. Mag.*, vol. 10, no. 6, pp. 84–98, 2009, doi: 10.1109/MMM.2009.933591.

[3] (2011, Nov. 2) WiSprys New Antenna Tuner Enables Small Antennas to Deliver High Speed Connections across Worldwide Frequency Bands. Online. [Online]. Available: http://www.wispry.com/newsmedia_pressrelease_click.php?id=138

[4] Cavendish kinetics. [Online]. Available: http://www.cavendish-kinetics.com/

[5] E. Dahlman, S. Parkvall, J. Skold, and P. Beming, *3G Evolution: HSPA and LTE for Mobile Broadband*. Oxford, UK: Elsevier Ltd., 2007.

[6] Infineon. (2006) PMB 5701; SMARTi 3G - The First Single-Chip Multi-Band CMOS Radio Frequency (RF) UMTS Transceiver IC. Infineon Technologies AG. 81726 Munich, Germany. [Online]. Available: http://www.infineon.com/cms/en/product/channel.html?channel=ff80808112ab681d0112ab6acf4c062f

[7] Tuning elements. Johanson Manufacturing. [Online]. Available: http://www.johansonmfg.com/pdf/Tuning-Elements.pdf

[8] G. Tsuzuki, M. P. Hernandez, and B. A. Willemsen, "Tuning fork filter design for hand scribe tuning," in *Proc. IEEE MTT-S Int. Microw. Symp. Digest*, 12–17 June 2005, p. 4pp.

[9] (2008, April) On line catalogue. RS Microwave Company, Inc. 22 Park Place, PO Box 273, Butler, NJ 07405. [Online]. Available: http://www.rsmicro.com/catalog.htm

[10] BT Series - Tunable Bandpass Filters. K&L Microwave. [Online]. Available: http://www.klmicrowave.com/product_attach/0/_plk196_1_BTSeriesNEW.pdf

[11] Tunable Bandpass Filter. Wainwright Instruments GmbH. [Online]. Available: http://www.wainwright-filters.com/pdf/bandpass/tunable/bcj-3900-4900-100-40-6-tun.pdf

[12] B. Yassini, M. Yu, D. Smith, and S. Kellett, "A Ku-band high-Q tunable filter with stable tuning response," *IEEE Trans. Microw. Theory Tech.*, vol. 57, no. 12, pp. 2948–2957, Dec. 2009, doi: 10.1109/TMTT.2009.2034215.

[13] W. W. Cavey, "Tunable ceramic filters," U.S. Patent 6,147,577, 2000.

[14] N. Alford, O. Buslov, V. Keis, I. Kotelnikov, A. Kozyrev, P. Kulic, and P. Petrov, "Tunable 4-pole piezoelectric filter based on two dielectric resonators," *Integrated Ferroelectrics*, vol. 77, pp. 123–128(6), 2005. [Online]. Available: http://www.ingentaconnect.com/content/tandf/ginf/2005/00000077/00000001/art00016

[15] H. Joshi, H. H. Sigmarsson, D. Peroulis, and W. J. Chappell, "Highly loaded evanescent cavities for widely tunable high-q filters," in *Proc. IEEE/MTT-S Int. Microwave Symp*, 2007, pp. 2133–2136.

[16] H. Joshi, H. H. Sigmarsson, S. Moon, D. Peroulis, and W. J. Chappell, "High-q fully reconfigurable tunable bandpass filters," *IEEE Trans. Microw. Theory Tech.*, vol. 57, no. 12, pp. 3525–3533, 2009, doi: 10.1109/TMTT.2009.2034309.

[17] S. Moon, H. H. Sigmarsson, H. Joshi, and W. J. Chappell, "Substrate integrated evanescent-mode cavity filter with a 3.5 to 1 tuning ratio," *IEEE Microw. Wireless Compon. Lett*, vol. 20, no. 8, pp. 450–452, 2010, doi: 10.1109/LMWC.2010.2050680.

[18] H. Joshi, H. H. Sigmarsson, S. Moon, D. Peroulis, and W. J. Chappell, "Tunable high q narrow-band triplexer," in *Proc. IEEE MTT-S Int. Microwave Symp. Digest MTT '09*, 2009, pp. 1477–1480.

[19] H. H. Sigmarsson, J. Lee, D. Peroulis, and W. J. Chappell, "Reconfigurable-order bandpass filter for frequency agile systems," in *Proc. IEEE MTT-S Int. Microwave Symp. Digest (MTT)*, 2010, pp. 1756–1759.

[20] E. J. Naglich, J. Lee, D. Peroulis, and W. J. Chappell, "A tunable bandpass-to-bandstop reconfigurable filter with independent bandwidths and tunable response shape," *IEEE Trans. Microw. Theory Tech.*, vol. 58, no. 12, pp. 3770–3779, 2010, doi: 10.1109/TMTT.2010.2086533.

[21] X. Liu, L. P. B. Katehi, W. J. Chappell, and D. Peroulis, "High- img src="/images/tex/228.gif" alt="q"¿ tunable microwave cavity resonators and filters using soi-based rf mems tuners," *J. Microelectromech. Syst.*, vol. 19, no. 4, pp. 774–784, 2010, doi: 10.1109/JMEMS.2010.2055544.

[22] M. S. Arif, W. Irshad, X. Liu, W. J. Chappell, and D. Peroulis, "A high-q magnetostatically-tunable all-silicon evanescent cavity resonator," in *Proc. IEEE MTT-S Int. Microwave Symp. Digest (MTT)*, 2011, pp. 1–4.

[23] J. Lee, E. J. Naglich, H. H. Sigmarsson, D. Peroulis, and W. J. Chappell, "Frequency-agile field-programmable filter array (fpfa) with multiple functionalities," in *Proc. IEEE MTT-S Int. Microwave Symp. Digest (MTT)*, 2011, pp. 1–4.

[24] H. Peng, X. Zhang, X. Guo, L. Mu, B. Wei, B. Gao, and B. Cao, "Mechanism study of mechanical tuning in HTS filter application," *Microw. Opt. Tech. Lett.*, vol. 49, no. 7, pp. 1565–1568, 2007. [Online]. Available: http://dx.doi.org/10.1002/mop.22561

[25] A. R. Brown and G. M. Rebeiz, "A varactor-tuned RF filter," *IEEE Trans. Microw. Theory Tech.*, vol. 48, no. 7, pp. 1157–1160, July 2000, doi: 10.1109/22.848501.

[26] M. Sanchez-Renedo and J. I. Alonso, "Tunable planar combline filter with multiple source/load coupling," in *Proc. IEEE MTT-S Int. Microw. Symp. Digest*, 12–17 June 2005, p. 4pp.

[27] H.-S. Lee and S.-W. Yun, "Microwave planar varactor tuned bandpass filters: Historical overview," *IEICE Trans Electron*, vol. E89-C, no. 12, pp. 1806–1813, 2006, doi: 10.1093/ietele/e89-c.12.1806. [Online]. Available: http://ietele.oxfordjournals.org/cgi/content/abstract/E89-C/12/1806

[28] S.-J. Park and G. M. Rebeiz, "Low-loss two-pole tunable filters with three different predefined bandwidth characteristics," *IEEE Trans. Microw. Theory Tech.*, vol. 56, no. 5, pp. 1137–1148, May 2008, doi: 10.1109/TMTT.2008.921638.

[29] A. Abbaspour-Tamijani, L. Dussopt, and G. Rebeiz, "A high performance mems miniature tunable bandpass filter," in *Microwave Symposium Digest, 2003 IEEE MTT-S International*, vol. 3, 8-13 June 2003, pp. 1785–1788vol.3.

[30] G. M. Kraus, C. L. Goldsmith, C. D. Nordquist, C. W. Dyck, P. S. Finnegan, I. Austin, F., A. Muyshondt, and C. T. Sullivan, "A widely tunable RF MEMS end-coupled filter," in *Proc. IEEE MTT-S Int. Microw. Symp. Digest*, vol. 2, 6–11 June 2004, pp. 429–432.

[31] S.-J. Park, K.-Y. Lee, and G. M. Rebeiz, "Low-loss 5.15-5.70 GHz RF MEMS switchable filter for wireless LAN applications," *IEEE Trans. Microw. Theory Tech.*, vol. 54, no. 11, pp. 3931–3939, Nov. 2006, doi: 10.1109/TMTT.2006.884625.

[32] I. Reines, A. Brown, M. El-Tanani, A. Grichener, and G. Rebeiz, "1.6-2.4 GHz RF MEMS tunable 3-pole suspended combline filter," in *Proc. IEEE MTT-S Int. Microw. Symp. Digest*, 15–20 June 2008, pp. 133–136.

[33] G. Sanderson, A. H. Cardona, T. C. Watson, D. Chase, M. Roy, J. M. Paricka, and R. A. York, "Tunable IF filter using thin-film BST varactors," in *Proc. IEEE MTT-S Int. Microw. Symp. Digest*, 3–8 June 2007, pp. 679–682.

[34] Y.-H. Chun, J.-S. Hong, P. Bao, T. J. Jackson, and M. J. Lancaster, "BST-varactor tunable dual-mode filter using variable Z_C transmission line," *IEEE Microwave and Wireless Components Letters*, vol. 18, no. 3, pp. 167–169, March 2008, doi: 10.1109/LMWC.2008.916778.

[35] M.-T. Nguyen, W. D. Yan, and E. P. W. Horne, "Broadband tunable filters using high Q passive tunable ICs," in *Proc. IEEE MTT-S Int. Microw. Symp. Digest*, 15–20 June 2008, pp. 951–954.

[36] K. Entesari and G. M. Rebeiz, "RF MEMS, BST, and GaAs varactor system-level response in complex modulation systems," *International Journal of RF and Microwave Computer-Aided Engineering*, vol. 18, no. 1, pp. 86–98, 2007, doi: 10.1002/mmce.20275.

[37] A. Tombak, J. P. Maria, F. T. Ayguavives, Z. Jin, G. T. Stauf, A. I. Kingon, and A. Mortazawi, "Voltage-controlled RF filters employing thin-film barium-strontium-titanate tunable capacitors," *IEEE Trans. Microw. Theory Tech.*, vol. 51, no. 2, pp. 462–467, Feb. 2003, doi: 10.1109/TMTT.2002.807822.

[38] J. Nath, D. Ghosh, J. P. Maria, A. I. Kingon, W. Fathelbab, P. D. Franzon, and M. B. Steer, "An electronically tunable microstrip bandpass filter using thin-film barium-strontium-titanate (BST) varactors," *IEEE Trans. Microw. Theory Tech.*, vol. 53, no. 9, pp. 2707–2712, Sept. 2005, doi: 10.1109/TMTT.2005.854196.

[39] K. Zhang, T. Watson, A. Cardona, and M. Fink, "Basrtio3-based 30–88mhz tunable filter," in *Proc. IEEE MTT-S Int. Microwave Symp. Digest (MTT)*, 2010.

[40] K. Entesari and G. M. Rebeiz, "A 12-18 GHz three-pole RF MEMS tunable filter," *IEEE Trans. Microw. Theory Tech.*, vol. 53, no. 8, pp. 2566–2571, Aug. 2005, doi: 10.1109/TMTT.2005.852761.

[41] Y. Kwon and S. Lee, "RF MEMS–enabling technology for millimeter-waves," *IEICE Trans Electron*, vol. E89-C, no. 7, pp. 898–905, 2006, doi: 10.1093/ietele/e89-c.7.898. [Online]. Available: http://ietele.oxfordjournals.org/cgi/content/abstract/E89-C/7/898

[42] S. Fouladi, M. Bakri-Kassem, and R. R. Mansour, "An integrated tunable band-pass filter using MEMS parallel-plate variable capacitors implemented with 0.35μm CMOS technology," in *Proc. IEEE MTT-S Int. Microw. Symp. Digest*, 3–8 June 2007, pp. 505–508.

[43] A. Abbaspour-Tamijani, L. Dussopt, and G. Rebeiz, "Miniature and tunable filters using MEMS capacitors," *IEEE Trans. Microw. Theory Tech.*, vol. 51, no. 7, pp. 1878 – 1885, July 2003, doi: 10.1109/TMTT.2003.814317.

[44] K. Entesari and G. M. Rebeiz, "A differential 4-bit 6.5-10 GHz RF MEMS tunable filter," *IEEE Trans. Microw. Theory Tech.*, vol. 53, no. 3, pp. 1103–1110, March 2005, doi: 10.1109/TMTT.2005.843501.

[45] K. Entesari, K. Obeidat, A. R. Brown, and G. M. Rebeiz, "A 25-75 MHz RF MEMS tunable filter," *IEEE Trans. Microw. Theory Tech.*, vol. 55, no. 11, pp. 2399–2405, Nov. 2007, doi: 10.1109/TMTT.2007.908674.

[46] I. C. Hunter and J. D. Rhodes, "Electronically tunable microwave bandpass filters," *IEEE Trans. Microw. Theory Tech.*, vol. 30, no. 9, pp. 1354–1360, 1982, doi: 10.1109/TMTT.1982.1131260.

[47] A. Guyette, "Alternative architectures for narrowband varactor-tuned bandpass filters," 29 2009-Oct. 1 2009, pp. 1828 –1831. [Online]. Available: http://ieeexplore.ieee.org/search/srchabstract.jsp?tp=&arnumber=5296161

[48] X. Y. Zhang, Q. Xue, C. H. Chan, and B.-J. Hu, "Low-loss frequency-agile bandpass filters with controllable bandwidth and suppressed second harmonic," *IEEE Trans. Microw. Theory Tech.*, vol. 58, no. 6, pp. 1557–1564, 2010, doi: 10.1109/TMTT.2010.2048250.

[49] B.-W. Kim and S.-W. Yun, "Varactor-tuned combline bandpass filter using step-impedance microstrip lines," *IEEE Trans. Microw. Theory Tech.*, vol. 52, no. 4, pp. 1279–1283, 2004, doi: 10.1109/TMTT.2004.825626.

[50] M. A. El-Tanani and G. M. Rebeiz, "Corrugated microstrip coupled lines for constant absolute bandwidth tunable filters," *IEEE Trans. Microw. Theory Tech.*, vol. 58, no. 4, pp. 956–963, 2010, doi: 10.1109/TMTT.2010.2042517.

[51] L. Athukorala and D. Budimir, "Compact second-order highly linear varactor-tuned dual-mode filters with constant bandwidth," *IEEE Trans. Microw. Theory Tech.*, vol. 59, no. 9, pp. 2214–2220, 2011, doi: 10.1109/TMTT.2011.2160279.

[52] S. Chang and S. Sivoththaman, "A tunable RF MEMS inductor on silicon incorporating an amorphous silicon bimorph in a low-temperature process," *IEEE Electron Device Letters*, vol. 27, no. 11, pp. 905–907, Nov. 2006, doi: 10.1109/LED.2006.884712.

[53] J. Muldavin, C. Bozler, S. Rabe, and C. Keast, "Large tuning range analog and multi-bit MEMS varactors," in *Proc. IEEE MTT-S Int. Microw. Symp. Digest*, vol. 3, 6–11 June 2004, pp. 1919–1922.

[54] T. K. K. Tsang and M. N. El-Gamal, "Very wide tuning range micro-electromechanical capacitors in the MUMPs process for RF applications," in *Proc. Digest of Technical Papers VLSI Circuits 2003 Symposium on*, 12–14 June 2003, pp. 33–36.

[55] M. Bakri-Kassem, S. Fouladi, and R. R. Mansour, "Novel high-Q MEMS curled-plate variable capacitors fabricated in 0.35μm CMOS technology," *IEEE Trans. Microw. Theory Tech.*, vol. 56, no. 2, pp. 530–541, Feb. 2008, doi: 10.1109/TMTT.2007.914657.

[56] M. Shavezipur, A. Khajepour, and S. Hashemi, "A novel linearly tunable butterfly-shape MEMS capacitor," *Microelectronics Journal*, vol. 39, no. 5, pp. 756 – 762, 2008, doi: DOI: 10.1016/j.mejo.2007.12.026.

[57] A. Oz and G. K. Fedder, "RF CMOS-MEMS capacitor having large tuning range," in *Proc. TRANSDUCERS, Solid-State Sensors, Actuators and Microsystems, 12th International Conference on*, vol. 1, 8–12 June 2003, pp. 851–854.

[58] T. Kawakubo, T. Nagano, M. Nishigaki, K. Abe, and K. Itaya, "RF-MEMS tunable capacitor with 3 V operation using folded beam piezoelectric bimorph actuator," *J. Microelectromech. Syst.*, vol. 15, no. 6, pp. 1759–1765, Dec. 2006, doi: 10.1109/JMEMS.2006.885985.

[59] M. Ruan, J. Shen, and C. B. Wheeler, "Latching micromagnetic relays," *J. Microelectromech. Syst.*, vol. 10, no. 4, pp. 511–517, Dec. 2001, doi: 10.1109/84.967373.

[60] E. Chan and R. Dutton, "Electrostatic micromechanical actuator with extended range of travel," *J. Microelectromech. Syst.*, vol. 9, no. 3, pp. 321–328, Sept. 2000, doi: 10.1109/84.870058.

[61] R. Nadal-Guardia, A. Dehe, R. Aigner, and L. Castaner, "Current drive methods to extend the range of travel of electrostatic microactuators beyond the voltage pull-in point," *J. Microelectromech. Syst.*, vol. 11, no. 3, pp. 255–263, June 2002, doi: 10.1109/JMEMS.2002.1007404.

[62] I. Borwick, R. L., P. A. Stupar, J. DeNatale, R. Anderson, C. Tsai, and K. Garrett, "A high Q, large tuning range, tunable capacitor for RF applications," in *Proc. Fifteenth IEEE International Conference on Micro Electro Mechanical Systems*, 20–24 Jan. 2002, pp. 669–672.

[63] M. Bakri-Kassem and R. Mansour, "Two movable-plate nitride-loaded MEMS variable capacitor," *IEEE Trans. Microw. Theory Tech.*, vol. 52, no. 3, pp. 831–837, March 2004, doi: 10.1109/TMTT.2004.823598.

[64] A. Cowen, R. Mahadevan, S. Johnson, and B. Hardy. MetalMUMPs design handbook: a MUMPs process. Online. MEMSCAP. [Online]. Available: http://www.memscap.com/mumps/documents/MetalMUMPs.DR.2.0.pdf

[65] H. Xie and G. K. Fedder, "A CMOS-MEMS lateral-axis gyroscope," in *Proc. 14th IEEE International Conference on Micro Electro Mechanical Systems MEMS 2001*, 21–25 Jan 2001, pp. 162–165.

[66] J.-C. Chang, A. Abidi, and M. Gaitan, "Large suspended inductors on silicon and their use in a 2-μm CMOS RF amplifier," *Electron Device Letters, IEEE*, vol. 14, no. 5, pp. 246–248, May 1993, doi: 10.1109/55.215182.

[67] H. Lakdawala, X. Zhu, H. Luo, S. Santhanam, L. R. Carley, and G. K. Fedder, "Micromachined high-Q inductors in a 0.18μm copper interconnect low-k dielectric CMOS process," *IEEE J. Solid-State Circuits*, vol. 37, no. 3, pp. 394–403, March 2002, doi: 10.1109/4.987092.

[68] D. Jachowski, "System requirements and review of conventional tuning technologies and techniques," in *IMS 2004 Workshop WFE-20*. Naval Research Laboratory, 2004.

[69] M. Kahrizi, S. Safavi-Naeini, and S. K. Chaudhuri, "Computer diagnosis and tuning of microwave filters using model-based parameter estimation and multi-level optimization," in *Proc. IEEE MTT-S Int. Microw. Symp. Digest*, vol. 3, 11–16 June 2000, pp. 1641–1644.

[70] S. Koziel, Q. Cheng, and J. Bandler, "Space mapping," *IEEE Microw. Mag.*, vol. 9, no. 6, pp. 105–122, December 2008, doi: 10.1109/MMM.2008.929554.

[71] V. Miraftab and R. R. Mansour, "Fully automated RF/microwave filter tuning by extracting human experience using fuzzy controllers," *IEEE Trans. Circuits Syst. I: Reg. Papers*, vol. 55, no. 5, pp. 1357–1367, June 2008, doi: 10.1109/TCSI.2008.916614.

[72] J. Dunsmore, "Tuning band pass filters in the time domain," in *Proc. IEEE MTT-S Int. Microw. Symp. Digest*, vol. 3, 13–19 June 1999, pp. 1351–1354.

[73] J. Ness, "A unified approach to the design, measurement, and tuning of coupled-resonator filters," *IEEE Trans. Microw. Theory Tech.*, vol. 46, no. 4, pp. 343–351, April 1998.

[74] N. Zahirovic and R. R. Mansour, "Sequential tuning of coupled resonator filters using Hilbert transform derived relative group delay," in *Proc. IEEE MTT-S Int. Microw. Symp. Digest*, 15–20 June 2008, pp. 739–742.

[75] J. Seeger and S. Crary, "Stabilization of electrostatically actuated mechanical devices," in *Proc. of Int. Solid State Sensors and Actuators Conf. (Transducers '97)*, vol. 2, 16-19 June 1997, pp. 1133–1136.

[76] J.-C. Chiou, L.-J. Shieh, and Y.-J. Lin, “CMOS-MEMS prestress vertical cantilever resonator with electrostatic driving and piezoresistive sensing,” *J. Phys. D: App. Phys.*, vol. 41, no. 20, p. 205102 (8pp), 2008. [Online]. Available: http://stacks.iop.org/0022-3727/41/205102

[77] L.-S. Zheng and M. S. C. Lu, “A large-displacement CMOS-micromachined thermal actuator with capacitive position sensing,” in *Proc. Asian Solid-State Circuits Conference*, Nov. 2005, pp. 89–92.

[78] G. Tsuzuki, M. Hernandez, E. M. Prophet, S. Jimenez, and B. A. Willemsen, “Ultra-selective constant-bandwidth electromechanically tunable HTS filters,” in *Proc. IEEE MTT-S Int. Microw. Symp. Digest*, 11–16 June 2006, pp. 693–696.

[79] H. H. Sigmarsson, A. Christianson, H. Joshi, S. Moon, D. Peroulis, and W. J. Chappell, “In-situ control of tunable evanescent-mode cavity filters using differential mode monitoring,” in *Proc. IEEE MTT-S Int. Microwave Symp. Digest MTT ’09*, 2009, pp. 633–636.

[80] S. Kerkowitz, “Frequency agile HTS filters,” in *IMS 2004 Workshop WFE-20.* Superconductor Technologies Inc., June 2004.

[81] M. Yu and W.-C. Tang (Invited), “A fully automated filter tuning robot for wireless base station diplexers,” in *Workshop: Computer Aided Filter Tuning, IEEE Int. Microw. Symp.*, Philadelphia, PA., June 8–13 2003.

[82] E. Neber, L. Billonnet, B. Jarry, and M. H. W. Hoffmann, “Novel detector structure for automatically tuned filters at microwave frequencies,” in *Proc. IEEE MTT-S Int. Microw. Symp. Digest*, vol. 3, 6–11 June 2004, pp. 1963–1966.

[83] S. Quintanel, H. Serhan, B. Jarry, L. Billonnet, and P. Guillon, “Theoretical and experimental analysis of automatic frequency control techniques for microwave active filters,” in *Proc. 30th European Microwave Conference*, Oct. 2000, pp. 1–4.

[84] M. Dishal, “Alignment and adjustment of synchronously tuned multiple-resonant-circuit filters,” *Proc. IRE*, vol. 39, no. 11, pp. 1448–1455, Nov. 1951.

[85] J. Dunsmore, “Advanced filter tuning using time domain transforms,” in *Proc. 29th European Microwave Conference*, vol. 2, Oct. 1999, pp. 72–75.

[86] ——, “Novel filter design method using time domain transforms,” in *Proc. 29th European Microwave Conference*, vol. 3, Oct. 1999, pp. 211–214.

[87] Agilent, “Agilent network analysis solutions advanced filter tuning using time domain transforms,” *Application Note 1287-10.* [Online]. Available: http://cp.literature.agilent.com/litweb/pdf/5980-2785EN.pdf

[88] F. Seyfert, L. Baratchart, J. P. Marmorat, S. Bila, and J. Sombrin, “Extraction of coupling parameters for microwave filters: determination of a stable rational model from scattering data,” in *Proc. IEEE MTT-S Int. Microw. Symp. Digest*, vol. 1, 8–13 June 2003, pp. 25–28.

[89] A. B. Jayyousi and M. J. Lancaster, “An algorithm for tuning microwave resonator filters using short circuit admittance parameters,” in *Proc. European Microwave Conference*, vol. 2, 4–6 Oct. 2005, p. 4pp.

[90] V. Miraftab and R. R. Mansour, "Automated microwave filter tuning by extracting human experience in terms of linguistic rules using fuzzy controllers," in *Proc. IEEE MTT-S Int. Microw. Symp. Digest*, 11–16 June 2006, pp. 1439–1442.

[91] A. E. Atia and A. E. Williams, "Narrow-bandpass waveguide filters," *IEEE Trans. Microw. Theory Tech.*, vol. 20, no. 4, pp. 258–265, 1972, doi: 10.1109/TMTT.1972.1127732.

[92] R. J. Cameron, C. M. Kudsia, and R. R. Mansour, *Microwave Filters for Communications Systems: Fundamentals, Design, and Applications.* John Wiley & Sons, Inc., 2007.

[93] J.-S. Hong and M. J. Lancaster, *Microstrip Filters for RF/Microwave Applications*, K. Chang, Ed. John Wiley & Sons Inc., 2001, vol. Wiley Series in Microwave and Optical Engineering.

[94] S. Amari, F. Seyfert, and M. Bekheit, "Theory of coupled resonator microwave bandpass filters of arbitrary bandwidth," *IEEE Trans. Microw. Theory Tech.*, vol. 58, no. 8, pp. 2188–2203, 2010, doi: 10.1109/TMTT.2010.2052874.

[95] D. M. Pozar, *Microwave Engineering*, 3rd ed. John Wiley & Sons Inc., 2005.

[96] SONNET Software Inc., "Sonnet 12.56," North Syracuse, NY, 2009.

[97] N. Zahirovic, R. R. Mansour, and M. Yu, "A three-step high-Q variable MEMS capacitor with low actuation voltage," in *Proc. Eu. Microw. Conf.*, 2009, pp. 1136–1139.

[98] H.-T. Hsu, H.-W. Yao, K. Zaki, and A. Atia, "Computer-aided diagnosis and tuning of cascaded coupled resonators filters," *IEEE Trans. Microw. Theory Tech.*, vol. 50, no. 4, pp. 1137 –1145, Apr. 2002, doi: 10.1109/22.993417.

[99] G. Pepe, F.-J. Gortz, and H. Chaloupka, "Computer-aided tuning and diagnosis of microwave filters using sequential parameter extraction," in *Proc. IEEE MTT-S Int. Microw. Symp. Digest*, vol. 3, April 2004, pp. 1373–1376.

[100] M. Meng and K.-L. Wu, "An analytical approach to computer-aided diagnosis and tuning of lossy microwave coupled resonator filters," *IEEE Trans. Microw. Theory Tech.*, vol. 57, no. 12, pp. 3188 –3195, Dec. 2009, doi: 10.1109/TMTT.2009.2033868.

[101] P. Perry and T. Brazil, "Hilbert-transform-derived relative group delay measurement of frequency conversion systems," in *Microwave Symposium Digest, 1996 IEEE MTT-S International*, vol. 3, 17-21 June 1996, pp. 1695–1698vol.3.

[102] G. Matthei, E. Jones, and L. Young, *Microwave Filters, Impedance-Matching Networks, and Coupling Structures*, february ed. Artech House Publishers, 1980.

[103] F. Domingue, S. Fouladi, A. B. Kouki, and R. R. Mansour, "Design methodology and optimization of distributed MEMS matching networks for low-microwave-frequency applications," *IEEE Trans. Microw. Theory Tech.*, vol. 57, no. 12, pp. 3030–3041, Dec. 2009, doi: 10.1109/TMTT.2009.2034218.

[104] S.-J. Park, I. Reines, C. Patel, and G. M. Rebeiz, "High-Q RF-MEMS 4–6 GHz tunable evanescent-mode cavity filter," *IEEE Trans. Microw. Theory Tech.*, vol. 58, no. 2, pp. 381–389, Feb. 2010, doi: 10.1109/TMTT.2009.2038448.

[105] M. Bakri-Kassem and R. R. Mansour, "A high-tuning-range MEMS variable capacitor using carrier beams," *Can. J. of Elect. and Comp. Eng.*, vol. 31, no. 2, pp. 89–95, 2006, doi: 10.1109/CJECE.2006.259190.

[106] X. Rottenberg, I. De Wolf, B. K. J. C. Nauwelaers, W. De Raedt, and H. A. C. Tilmans, "Analytical model of the DC actuation of electrostatic MEMS devices with distributed dielectric charging and nonplanar electrodes," *J. Microelectromech. Syst.*, vol. 16, no. 5, pp. 1243–1253, Oct. 2007, doi: 10.1109/JMEMS.2007.899334.

[107] M. S.-C. Lu and G. K. Fedder, "Position control of parallel-plate microactuators for probe-based data storage," *J. Microelectromech. Syst.*, vol. 13, no. 5, pp. 759–769, Oct. 2004, doi: 10.1109/JMEMS.2004.835761.

[108] D. Piyabongkarn, Y. Sun, R. Rajamani, A. Sezen, and B. J. Nelson, "Travel range extension of a MEMS electrostatic microactuator," *IEEE Trans. Control Syst. Technol.*, vol. 13, no. 1, pp. 138–145, Jan. 2005, doi: 10.1109/TCST.2004.838572(410) 13.

[109] G. K. Fedder, S. Santhanam, M. L. Reed, S. C. Eagle, D. F. Guillou, M. S.-C. Lu, and L. R. Carley, "Laminated high-aspect-ratio microstructures in a conventional CMOS process," in *Proc. Int. Workshop Micro Elect. Mech. Syst.*, 1996, pp. 13–18.

[110] M. G. el Hak, Ed., *MEMS Design and Fabrication.* CRC Press Taylor and Francis Group, 2006.

[111] S. Hafizovic, K.-U. Kirstein, and A. Hierlemann, *Applied Scanning Probe Methods V - Integrated Cantilevers and Atomic Force Microscopes*, ser. Nanoscience and Technology. Springer Berlin Heidelberg, 2007.

[112] J. J. Neumann, D. W. Greve, and I. J. Oppenheim, "Comparison of piezoresistive and capacitive ultrasonic transducers," in *Proc. SPIE*, S.-C. Liu, Ed., vol. 5391, no. 1, 2004, pp. 230–238. [Online]. Available: http://link.aip.org/link/?PSI/5391/230/1

[113] G. M. Rebeiz, *RF MEMS: Theory, Design and Technology.* John Wiley & Sons, Inc., 2003.

[114] N. Zahirovic, R. R. Mansour, and M. Yu, "A MEMS variable capacitor with piezoresistive position sensing fabricated in a standard 0.35μm CMOS process," in *Proc. IEEE MTT-S Int. Microw. Symp. Digest*, 2010, pp. 1154–1157.

[115] ——, "Scalar measurement-based algorithm for automated filter tuning of integrated chebyshev tunable filters," *IEEE Trans. Microw. Theory Tech.*, vol. 58, no. 12, pp. 3749–3759, 2010, doi: 10.1109/TMTT.2010.2085791.

[116] ——, "A mems variable capacitor with piezoresistive position sensing fabricated in a standard 0.35um cmos process," in *Proc. IEEE MTT-S Int. Microwave Symp. Digest (MTT)*, 2010.

[117] S. Fouladi, F. Domingue, N. Zahirovic, and R. R. Mansour, "Distributed mems tunable impedance-matching network based on suspended slow-wave structure fabricated in a standard cmos technology," *IEEE Trans. Microw. Theory Tech.*, vol. 58, no. 4, pp. 1056–1064, 2010, doi: 10.1109/TMTT.2010.2042511.